# MULTISCALE MODELING AND THERMODYNAMIC CONSISTENCY BETWEEN SOFT-PARTICLE REPRESENTATIONS OF MACROMOLECULAR LIQUIDS

by

JAMES JOSEPH McCARTY V

A DISSERTATION

Presented to the Department of Chemistry and Biochemistry
and the Graduate School of the University of Oregon
in partial fulfillment of the requirements
for the degree of
Doctor of Philosophy

December 2013

DISSERTATION APPROVAL PAGE

Student: James Joseph McCarty V

Title: Multiscale Modeling and Thermodynamic Consistency between Soft-Particle Representations of Macromolecular Liquids

This dissertation has been accepted and approved in partial fulfillment of the requirements for the Doctor of Philosophy degree in the Department of Chemistry and Biochemistry by:

| | |
|---|---|
| Dr. Michael Kellman | Chair |
| Dr. Marina G. Guenza | Advisor |
| Dr. Andrew H. Marcus | Core Member |
| Dr. Peter H. von Hippel | Core Member |
| Dr. Richard P. Taylor | Institutional Representative |

and

| | |
|---|---|
| Kimberly Andrews Espy | Vice President for Research & Innovation/ Dean of the Graduate School |

Original approval signatures are on file with the University of Oregon Graduate School.

Degree awarded December 2013

DISSERTATION ABSTRACT

James Joseph McCarty V

Doctor of Philosophy

Department of Chemistry and Biochemistry

December 2013

Title: Multiscale Modeling and Thermodynamic Consistency between Soft-Particle Representations of Macromolecular Liquids

Coarse-graining and multi-scale approaches are rapidly becoming important tools for computer simulations of large complex molecular systems. Such theoretical models are powerful tools because they allow one to probe the essential features of a complex, many-bodied system on length and time scales over which emergent phenomena may occur. Because of the computational advantages and fundamental insight made available through coarse-grained methods, a vast array of various phenomenological potentials to describe coarse-grained interactions have been developed; nonetheless, the ability of these potentials to provide quantitative information about several different properties of the same system is not evident. On a theoretical level, it is not well-understood how small correlations in the long-range structure propagate through the coarse-graining procedure into the effective potential and lead to incorrect thermodynamics. Taking an alternative approach, this dissertation will discuss an analytical coarse-graining method for synthetic polymer chains of specific chemical structure, where a group of atoms on a polymer chain are represented by a variable number of soft interacting effective sites. The approach is based in liquid-state theory, providing a theoretical framework to address questions

of thermodynamic consistency. It will be shown that the proposed method of coarse-graining maintains thermodynamic consistency for a variety of polymer models. In a multiscale modeling scheme simulations of the same system represented by several different levels of detail may be joined to provide a complete description of the system at all length and time scales of interest.

This dissertation includes previously published and unpublished co-authored material.

# CURRICULUM VITAE

NAME OF AUTHOR: James Joseph McCarty V

GRADUATE AND UNDERGRADUATE SCHOOLS ATTENDED:

University of Oregon, Eugene, OR
California Polytechnic State University, San Luis Obispo, CA

DEGREES AWARDED:

Doctor of Philosophy, Chemistry, 2013, University of Oregon
Bachelor of Science, Biochemistry, 2007, California Polytechnic State University

AREAS OF SPECIAL INTEREST:

Theoretical Chemical Physics
Statistical Mechanics
Soft Condensed Matter
Polymer Physics

PROFESSIONAL EXPERIENCE:

Research Assistant, University of Oregon, 2008-2013. Advisor: M. Guenza

Teaching Assistant, University of Oregon, 2007-2008, 2011-2013

NSF GK-12 Program Fellow, University of Oregon, 2012-2013

Science Literacy Program Fellow, University of Oregon, 2012

Participant in the Workshop on Multiscale Theory and Simulation, Center for Multiscale Theory and Simulation, University of Chicago, Chicago, IL, June 2012

Participant in the First Les Houches School in Computational Physics: Soft Matter, Ecole de Physique des Houches, Les Houches, France, June - July 2011

Research Assistant, California Polytechnic State University, 2006-2007. Advisor: L. Lindert

Research Assistant, California Polytechnic State University, 2005-2006. Advisor: J. Goers

PUBLICATIONS:

A. J. Clark, J. McCarty, and M. G. Guenza. Effective Potentials for Representing Polymers in Melts as Chains of Interacting Soft Particles *J. Chem. Phys.*, **139**, 124906, (2013).

J. McCarty, A. J. Clark, I. Y. Lyubimov, and M.G. Guenza. Thermodynamic Consistency between Analytic Integral Equation Theory and Coarse-Grained Molecular Dynamics Simulations of Homopolymer Melts *Macromol.*, **45** 8482 (2012).

A. J. Clark, J. McCarty, I. Y. Lyubimov, and M. G. Guenza. Thermodynamic Consistency in Variable-Level Coarse-Graining of Polymeric Liquids *Phys. Rev. Lett.*, **109** 168301 (2012).

J. McCarty and M. G. Guenza. Multiscale Modeling of Binary Polymer Mixtures: Scale Bridging in the Athermal and Thermal Regime *J. Chem. Phys.*, **133** 094904, (2010).

I. Y. Lyubimov, J. McCarty, A. Clark, and M. G. Guenza. Analytical rescaling of polymer dynamics from mesoscale simulations. *J. Chem. Phys.*, **132**, 224903, (2010).

J. McCarty, I. Y. Lyubimov, and M. G. Guenza. Effective Soft-Core Potentials and Mesoscopic Simulations of Binary Polymer Mixtures *Macromol.*, **43** 3964, (2010).

J. McCarty, I. Y. Lyubimov, and M. G. Guenza. Multiscale Modeling of Coarse-Grained Macromolecular Liquids *J. Phys. Chem. B.*, **113** 11876, (2009).

# ACKNOWLEDGEMENTS

Foremost, I would like to gratefully acknowledge my advisor, Dr. Marina Guenza, for endless support and patience throughout my graduate career and for introducing me to the topics of polymer physics and non-equilibrium statistical mechanics. None of this work would have been possible without her careful guidance, instruction, and useful insights.

In addition, I would like to express my gratitude to members of the Guenza research group, past and present, from whom I have learned many "tricks of the trade." In particular I would like to thank Ivan Lyubimov who introduced me to computational work, Anthony Clark, who developed much of the foundational work which is developed in this thesis, and Jeremy Copperman, who offered much support and useful discussion.

I would like to acknowledge the support and commitment of my thesis committee. In particular, Andrew Marcus provided me with valuable mentorship and assistance in my professional development, and Peter von Hippel has offered many interesting and insightful ideas during committee meetings. I would like to offer my special thanks to Michael Kellman for being willing to step in as committee chair. The willingness of chair, Michael Kellman and external member, Richard Taylor, to accept my many requests throughout this process is greatly appreciated.

I would like to recognize the contributions from Dr. Lisa Lindert and Dr. John Goers at California Polytechnic State University for giving me training and introducing me to scientifically rigorous research, and for their interest in my development as a scientist. I would also like to acknowledge Dr. Rod Schoonover whose undergraduate physical chemistry class introduced me to the subject and

encouraged me to purse physical chemistry in graduate school.

Much of the computational work in this dissertation was accomplished through the XSEDE project funded through NSF and on the ACISS cluster at the University of Oregon. In particular Robert Yelle has been exceedingly helpful in technical assistance using the ACISS computation resources.

I would like to acknowledge partial financial support from the NSF GK-12 program, and from the HMI funded Science Literacy Program both at the University of Oregon, and through teaching assistantships provided through the Department of Chemistry.

I dedicate this work to my parents, Jim and Marilou McCarty, who have always provided me with unconditional support and motivation. No words could adequately express my gratitude for all that they have done for my success.

TABLE OF CONTENTS

Chapter Page

I. INTRODUCTION . . . . . 1

I.1. Basic Concepts of Polymer Physical Chemistry . . . . . 1

I.2. Liquid State Theory of Polymer Melts . . . . . 4

I.3. Perspectives on Coarse-Graining Models . . . . . 8

I.4. Organization of Dissertation . . . . . 12

II. THEORETICAL BACKGROUND: HIGHLY COARSE GRAINED REPRESENTATIONS OF POLYMER MELTS . . . . . 14

II.1. Generalized PRISM Ornstein Zernike Equation . . . . . 14

II.2. Soft Sphere Limit . . . . . 18

II.3. Analytical Approximation of the Effective Potential . . . . . 20

II.4. Conclusion . . . . . 22

III. THERMODYNAMIC CONSISTENCY BETWEEN ANALYTICAL INTEGRAL EQUATION THEORY AND COARSE-GRAINED MOLECULAR DYNAMICS SIMULATIONS OF HOMOPOLYMER MELTS . . . . . 23

III.1. Thermodynamic Consistency in Density Dependent Potentials . . . . . 23

III.2. Theoretical Background: Coarse-Grained Model and Effective Pair Potential . . . . . 27

III.3. Thermodynamics of Soft Interacting Particle Description of a Polymer Melt . . . . . 33

III.4. Equivalence with Monomer Level Description . . . . . 47

Chapter Page

III.5. Comparison of Analytical Expressions with Molecular Dynamics Simulations of Soft Spheres . . . . . 52

III.6. Conclusion . . . . . 56

IV. ACCURATE DETERMINATION OF THE THERMODYNAMIC PROPERTIES OF POLYETHYLENE MELTS FROM HIGHLY COARSE-GRAINED SIMULATIONS: COMPARISON WITH REALISTIC MOLECULAR DYNAMICS SIMULATIONS . . . . . 58

IV.1. Introduction . . . . . 58

IV.2. Molecular Dynamics Simulations . . . . . 60

IV.3. Thermodynamic Properties . . . . . 64

IV.4. Conclusion . . . . . 86

V. OBTAINING THE COARSE-GRAINED POTENTIAL FOR REALISTIC POLYMER MODELS . . . . . 87

V.1. Numerical PRISM Solution for the Direct Correlation Function . . . . . 88

V.2. Calculation of the Coarse-Grained Potential . . . . . 91

VI. MULTISCALE MODELING OF MACROMOLECULAR LIQUIDS AND BLENDS . . . . . 102

VI.1. Introduction . . . . . 103

VI.2. The Multiscale Method . . . . . 105

VI.3. Determining the Crossover Limit . . . . . 115

VI.4. Multiscale Modeling of Polymer Blends . . . . . 117

Chapter Page

VI.5. Thermal Blends . . . . . 121

VI.6. Conclusion . . . . . 123

VII. EFFECTIVE SOFT-CORE POTENTIALS AND MESOSCOPIC SIMULATIONS OF BINARY POLYMER MIXTURES . . . . . 125

VII.1. Introduction . . . . . 125

VII.2. Mesoscopic Pair Correlation Functions for Asymmetric Binary Polymer Blends . . . . . 127

VII.3. The Effective Soft Core Potential . . . . . 132

VII.4. Mesoscopic Simulations of Binary Mixtures . . . . . 137

VII.5. Total Pair Correlation Functions of the Polymer Mixture from Mesoscale Simulations . . . . . 138

VII.6. Scattering Functions and Concentration Fluctuations . . . . . 144

VII.7. Corrections to the Debye Intramolecular Form Factor . . . . . 154

VII.8. Applications to Miscible LCST Blends . . . . . 156

VII.9. Conclusion . . . . . 158

VIII. CONCLUSION . . . . . 161

VIII.1. Perspectives on the Completed Work . . . . . 161

VIII.2. Future Directions . . . . . 164

Chapter Page

APPENDIX: SAMPLE PYTHON FUNCTION TO GENERATE THE COARSE-GRAINED POTENTIAL . . . . . 168

A.1. Soft Sphere . . . . . 168

A.2. Tri-Block Model . . . . . 170

A.3. Block Average Description . . . . . 177

REFERENCES CITED . . . . . 183

LIST OF FIGURES

Figure Page

I.1. Some typical polymer topologies. Figure reproduced from Ref[2] . . . . 3

II.1. Schematic depiction of the intermolecular and intramolecular distribution functions between monomers (mm), fictitious sites (bb), and monomers about fictitious sites (bm). . . . . 16

II.2. Schematic depiction of the soft sphere limit where there are now just the intermolecular distributions between fictitious sites $h^{cc}$ and intramolecular distributions of monomers about the center of mass $\Omega^{cm}$. . . . . 19

III.1. Schematic description of the coarse-graining process. First as an approximate model of the atomistic picture, we represent the actual polymer chain as a Gaussian thread. The parameters from this level of description enter the coarse-graining model, where individual chains are represented as soft colloidal particles, or point particles with a long range, soft effective interaction. . . . . 32

III.2. Top: The equation of state obtained from the MSA approximation, Equation III.37 is shown (open circles) in comparison with the full equation of state using the HNC potential, Equation III.48 (solid line) for the PRISM thread model. The two lines superimpose and are nearly indistinguishable, both scaling linearly with $N$ for large N. Bottom: For comparison is show the contributions to the equation of state from Equations III.41 and III.46, both of which quickly approach their asymptotic value with $N^{-1}$ scaling for the potential of mean force term (dashed line) and with $N^{-1/2}$ scaling for the third term (solid line). . . 44

Figure Page

III.3. The soft potential (Top Left) calculated for the representative case for PE with $N = 100$ and $\rho = 0.78$ g/mL. The dashed lines indicate the distances at which the potential was cut, which occur where the force crosses zero (Top right). The inset highlights the region where the potential is cut. The bottom panels show the pressure (Bottom Left) and potential energy (Bottom right) calculated directly from mesoscale simulations of point particles cut after the first repulsive peak (squares), the first repulsive plus first attractive well (open circles) and after the first repulsive, first attractive, and second repulsive peak (crosses). Comparison is made with our analytical prediction given by Equation III.37 and Equation III.28 (solid line) for different densities. . . . . 55

III.4. Comparison between the pressure calculated directly from mesoscale simulations of point particles (squares) with analytical prediction given by Equation III.37 (line) for different densities of PE with $N = 500$. . . 56

III.5. Comparison between the potential energy calculated directly from the average of the mesoscale simulation (squares) with the analytical prediction given by Equation III.28 (line) for PE with $N = 500$ . . . . 57

IV.1. Coarse-graining at multiple block-levels. The far right is a snapshot of a typical configuration from UA a simulation of polyethylene. Moving from right to left the same chain is represented by 5 blocks, 3 blocks, to a single soft sphere. Below is a snapshot of a typical mesoscale simulations, where each sphere represents a single polyethylene chain. . . . . 61

IV.2. Comparison of the pressure from united atom simulations of PE $N = 44$ (black circles), PE $N = 78$ (squares) and PE $N = 200$ ( black triangle) with coarse-grained simulations of the soft sphere model (stars) and tri-block model (green triangles) and 5-block model (red squares). . . . . 65

IV.3. Comparison of the pressure from united atom simulations of PE $N = 66$ (black circles), PE $N = 100$ (black squares) with coarse-grained simulations at the soft sphere level (stars) and 3-block level for PE100 (green triangles). . . . . 66

IV.4. Pressure vs. degree of polymerization calculated for a hierarchy of soft-block simulations as compared to united atom simulations. All simulations were carried out at constant temperature, T=509K, and density, $\rho = 0.733$ g/mL. United atom model is depicted with black circles, soft sphere model with blue asterisk, tri-block with green triangles, 5-block with red squares, 10-block with maroon diamonds, and 20-block with orange left-oriented triangle. . . . . 70

IV.5. Pressure data from United Atom simulations plotted as function of the effective packing fraction. . . . . 71

IV.6. Estimated free energy change obtained via thermodynamic integration of the pressure, as a function of packing fraction compared to a reference packing fraction of $\eta_1 = 0.27$. All systems collapse to a universal curve within numerical precision, independent of degree of polymerization. The solid and dashed lines represent equation IV.17 evaluated at N=44 and 200 respectively. . . . . 72

IV.7. Excess free energy given by Equation IV.18 as a function of packing fraction. For comparison, the dashed line depicts the excess free energy for a simple liquid of hard spheres. . . . . 73

IV.8. Depiction of the three block model mapped onto a random walk. The coarse-grained coordinates are $R_1$ and $R_2$, which are the bond vectors joining effective CG sites, and the angle, $\theta$, between them. Note that many underlying atomistic configurations are possible for each configuration of the coarse-grained coordinates. . . . . 76

IV.9. Distribution of the bond vector (top) and angle (bottom) from coarse-grained simulations (open circles) compared to united atom simulations (filled circles). The solid line indicates the predicted distribution for a Gaussian chain. . . . . 77

IV.10. Comparison of the intramolecular distribution, $\omega^{bb}(k)$ (top) and intermolecular correlation function, $h^{bb}(r)$, (bottom) between block centers calculated from both 3-block and united atom simulations of PE225. The solid line depicts theoretical predictions from the coarse-grained model. . . . . 78

IV.11. Internal energy calculated from coarse grained simulation of PE200 (top) and PE1000 (bottom) as a function of the number of blocks ($n_b$). The last point is the internal energy from united atom simulations. The contribution from the kinetic energy has be subtracted. The red symbols show theoretical predictions and the solid line is an extrapolation of the theory for large $n_b$. . . . . 81

V.1. Semiflexible chain model used as the molecular model for numerical PRISM equations. This model allows for a realistic estimate of $c_0$, which is input into the coarse-grained model. . . . . 89

V.2. Left: Calculated value of $c_0$ from numerical PRISM using a simple SFC chain model as a function of the monomer site density. Three different chain lengths are shown; $N = 44$ (circles), $N = 100$ (squares) and $N = 200$ (triangles). The line is a fit to a quadratic polynomial to serve as a guide to the eye. Right: Calculated values of $c_0$ from numerical PRISM as a function of polymer chain length at fixed density, $\rho = 0.03153$ sites/$\mathring{A}^3$ (circles). The solid line is a fit to the form $a + b/N$. . . . . 92

V.3. The effective pair potential for PE100 at an intermediate density of $\rho = 0.03656$ sites/$\mathring{A}^3$ The solid line is the potential calculated using numerical PRISM with the SFC chain model. The dashed line is the same potential using the thread model value for $c_0$ for comparison. The inset shows the virial force. . . . . 93

V.4. The monomer radial distribution function for PE with $N = 100$ at a monomer density $\rho = 0.03355$ sites/$\mathring{A}^3$ calculated from United Atom simulations (solid line) and from PRISM calculation using the SFC model with $d_{HS} = 3.9\mathring{A}$ which gives the best agreement between the pressures . . . . . 94

VI.1. The Multiscale modeling procedure to calculate the total monomer distributions at all length-scales of interest. The total correlation function calculated from different simulations are combined in k-space at an intermediate value of k, and subsequently numerically Fourier Transformed to real space. . . . . 106

VI.2. Plot of $h^{mm}(k)$ for different polymer melts (hhPP, PE, and sPP). Solid line depicts $h^{mm}(k)$ calculated using Equation VI.1. Symbols represent data points from full UA MD simulation. . . . . 108

VI.3. Left: Plot of the total correlation function, $h^{mm}(k)$, for polymer melts of (a) sPP and (c) hhPP, obtained by combining mesoscale and UA MD simulations. Mesoscale simulation depicts $h^{mm}(k)$ over the small k range whereas UA simulation provides data over the large k range. The dashed line indicates the point at which the two simulations were combined. The inset depicts the local peak. Right: Plot of the related $h^{mm}(r)$, the total correlation function in real space for (b) sPP and (d) hhPP. The solid line depicts $h^{mm}(r)$ calculated using our multiscaling approach and the open circles represent data points from UA MD simulations. . . . . 109

VI.4. Left: Plot of the total correlation function, $h^{mm}(k)$, for polymer melts of (a) iPP and (c) PIB, obtained by combining mesoscale and UA MD simulations. Mesoscale simulation depicts $h^{mm}(k)$ over the small k range whereas UA simulation provides data over the large k range. The dashed line indicates the point at which the two simulations were combined. The inset depicts the local peak. Right: Plot of the related $h^{mm}(r)$, the total correlation function in real space, for polymer melts of (b) iPP and (d) PIB. The solid line depicts $h^{mm}(r)$ calculated using our multiscaling approach and the open circles represent data points from UA MD simulations. . . . . 110

VI.5. Left: Plot of the total correlation function, $h^{mm}(k)$, for polyethylene of varying chain length, (a) PE44 ($T$ = 400K), (c) PE48 ($T$ = 448K) obtained by our multiscale modeling approach of combining mesoscale and UA MD simulations. The inset depicts the local peak. Right: Plot of $h^{mm}(r)$, the total correlation function for different PE chains. The solid line depicts $h^{mm}(r)$ calculated using our multiscaling approach and the open circles represent data points from UA MD simulations. . . . . 111

VI.6. Left: Plot of the total correlation function, $h^{mm}(k)$, for polyethylene of varying chain length, (a) PE66 ($T$ = 448K), (c) PE96 ($T$ = 448K) obtained by our multiscale modeling approach of combining mesoscale and UA MD simulations. The inset depicts the local peak. Right: Plot of $h^{mm}(r)$, the total correlation function for different PE chains. The solid line depicts $h^{mm}(r)$ calculated using our multiscaling approach and the open circles represent data points from UA MD simulations. . . . . 112

VI.7. Plot of the local peak for the total correlation function, $h^{mm}(k)$, for polymer melts of PE at increasing degree of polymerization, ($N$ = 48, 66, 96) from local UA simulations at T=448 K . . . . . 114

VI.8. Fraction of intramolecular contacts, $f_s(r)$, for melts of polymers with different monomer architectures . . . . . 116

VI.9. (a) Plot of $h^{cc}_{AA}(k)$ for hhPP/sPP obtained from mesoscale simulation (open red circles). Comparison with UA data (filled circles) and theoretical predictions (solid line) shows quantitative agreement. (b) Plot of $h^{mm}_{AA}(k)$ calculated using the inverse mapping procedure, Equation VI.5, (open red circles) compared to data from the full UA MD simulation (solid circle). . . . . 119

VI.10. (Left) Multiscale modeling: The left panels show the total correlation function, $h^{mm}(k)$, for AA (top), BB (middle), and AB (bottom) interactions, for a mixture of 50:50 hhPP/sPP. The data over the range of small k values was obtained by mesoscale simulation, whereas over the large k range it was obtained by UA MD simulation. The inset depicts the local structure. The dashed line indicates the value at which the two simulations were combined. (Right) The correlation function, $h^{mm}(r)$, after Fourier transform (solid red line) is compared with results from the full UA MD simulation (open symbols). . . . . 120

VI.11. (A) The concentration fluctuation structure factor obtained from the multiscale modeling procedure (open circles) for hhPP/PE ($\phi = 0.5$) at $T = 453K$. For comparison the RPA equation evaluated at $\chi = 0.0016$ (solid line) and $\chi = 0.00$ (dashed line) is shown. The inset shows the structure factor from the full UA simulation. (B) The same as part (A), except for PIB/PE ($\phi = 0.5$), for which the RPA equation, evaluated at $\chi = 0.0034$ (solid line) and $\chi = 0.00$ (dashed line), is shown. (C) the same except for the hhPP/PIB blend, and the RPA equation is evaluated at $\chi = 0.00038$ (solid line) and $\chi = 0.00$ (dashed line). . . . 122

VII.1. Comparison of the effective pair interaction potential $v_{\alpha\beta}(r)$ derived from the HNC closure for the hhPP/PE blend, $\phi = 0.5$, with $\chi/\chi_s \in \{0.0, 0.1, 0.3, 0.5, 0.7, 0.9\}$. The upper panels show $v^{cc}(r)$ obtained via the Padé approximation and the lower panels show $v^{cc}(r)$ from the Debye form. The inset highlights the change in the repulsive part of the potential as the reduced temperature is changed. The solid line represents the athermal regime ($\chi/\chi_s = 0.0$). In both the AA and BB curves, the repulsive component decreases as the system approaches the spinodal ($\chi/\chi_s = 1$), whereas the AB curve increases. . . . . 136

VII.2. Comparison of mesoscopic simulations [open symbols] with UA MD simulations [filled symbols] for the $h_{\alpha\beta}(r)$ of polymer mixtures under athermal conditions. Also shown are theoretical predictions [solid curves] based on our analytic expression, Equation VII.9. Presented are data from $AA$ [circles], $AB$ [triangles], and $BB$ [squares] contributions for compositionally symmetric and asymmetric systems. For comparison, numerical predictions obtained from Equation VII.3 using the Debye form are shown [dashed curves]. For clarity the inset highlights the peak region for each separate contribution. . . . . 140

VII.3. Comparison of mesoscopic simulations [symbols] with numerical predictions [curves] for the $h_{\alpha\beta}(r)$ of a 50:50 mixture of hhPP/PE for different values of the ratio, $\chi/\chi_s$. The left panel shows results obtained using the Padé approximation with our truncation scheme. The right panel depicts the results when the Debye form is used. Mesoscale simulations are shown to capture the structural changes that occur as the system approaches the spinodal. The inset highlights the peak region of $h(r)$ . . . . . 141

VII.4. Comparison of mesoscopic simulations [symbols] with numerical predictions [curves] for the $h_{\alpha\beta}(r)$ of hhPP/PE for different values of $\phi$. Left panels show data when $\chi = 0.008$. Right panels show data for $\chi = 0.012$. Shown are the separate contributions for $AA$ [circles], $AB$ [triangles], and $BB$ [squares] interactions. As $\phi$ increases, the fraction of species B in the simulation box decreases, and thus, the statistics become poorer for BB interactions. . . . . 145

VII.5. Same as Figure VII.4 except that left panels show data when $\chi = 0.016$, and right panels show data for $\chi = 0.019$. . . . . 146

VII.6. Top Left: Partial structure factor, $S^{\phi\phi}(k)$, obtained from mesoscopic simulations [symbols] of the coarse-grained mixture of 50:50 hhPP/PE with $\chi/\chi_s \in \{0.0, 0.1, 0.3, 0.5, 0.7\}$. The curves represent theoretical values obtained using the Debye function. Top Right: Partial structure factor, $S^{\rho\rho}(k)$ and Bottom Left: $S^{\rho\phi}(k)$ are also shown for different values of $\chi/\chi_s$. $S^{\rho\rho}(k)$ does not change noticeably with $\chi/\chi_s$ but $S^{\rho\phi}(k)$ has a slight $\chi/\chi_s$ dependence at low k. Bottom Right: Extrapolated $1/S^{\phi\phi}(0)$ values vs. $\chi$ [symbols]. The line represents a linear fit to the data and is extrapolated to the spinodal, $\chi_s$ (dashed line). . . . . 149

VII.7. The concentration fluctuation partial structure factor, $S^{\phi\phi}(k)$, calculated from mesoscale simulations [filled symbols] at different values of $\phi$ for the mixture hhPP/PE. The curves represent theoretical predictions. . . . . 152

VII.8. The extrapolated $k = 0$ limit of $S^{\phi\phi}(k)$ based on our numerical predictions [data points] and from our analytical expression, Equation VII.20, [curves] as a function of $\phi$ for different fixed values of $\chi$, for the mixture hhPP/PE. . . . . 153

VII.9. Top: Inverse concentration fluctuation structure factor, $S^{\phi\phi}(0)$ plotted against the interaction parameter, $\chi$ for different values of $\phi$, for the mixture hhPP/PE. The solid line depicts a linear fit to the data and the dashed line shows the extrapolation to the spinodal. Bottom: Phase diagram for the coarse-grained mixture obtained from the above extrapolation to the spinodal, $\chi_s$. The solid curve depicts the Florry-Huggins analytical expression. . . . . 155

VII.10.Top Left: The effective pair potential between A type chains for an athermal mixture of hhPP/PE with $\phi = 0.5$ when corrections to the Debye formula are included (solid line). The dashed line indicates the potential obtained using the uncorrected Debye formula. Top Right: The AA component of the correlation function calculated from mesoscale simulations using the corrected Debye formula at $\chi = 0.0$ (open circles) and $\chi = 0.7$ (open triangles). The solid line represents theoretical predictions, and the dashed line indicates predictions using the Debye formula. Filled circles represent UA MD simulations. Bottom Left: BB component and Bottom Right: AB component of the correlation function for the same mixture. The pcfs obtained using the Padé approximation are shown to nearly superimpose with the corrected Debye form. (Partially shaded circles). . . . . 157

VII.11.Top Left: AA component of the correlation function for the miscible blend, hhPP/PIB ($\phi = 0.5$) at $T = 2000K$ (circles) and $T = 200K$ (triagles). Theoretical predictions are indicated as solid lines. Top Right: BB component and Bottom Left: AB component of the same mixture. Bottom Right: The concentration fluctuation structure factor for hhPP/PIB obtained from mesoscale simulation (symbols) and from theory (solid line) at various temperatures. . . . . 159

LIST OF TABLES

Table Page

IV.1. Polyolefin Melt Simulation Parameters . . . . . 61

VI.1. Total Number of Sites ($N_{sites}$) and Number of Molecules ($n$) included in a spherical volume of radius $r$, evaluated for $f_s(r) = 0.025$ and 0.05 . . . . . 117

VI.2. Mesoscale Simulation (MS-MD) Particle Number and Box Dimension Compared to UA Box Dimension. All UA simulations are for 1600 chains. . . . . 124

VII.1. Polyolefin blends ($T = 453$ K, $N_A = N_B = 96$) . . . . . 135

VII.2. Mesoscale Simulation Parameters for Blends of hhPP/PE . . . . . 138

VII.3. Mesoscale Simulation Parameters for Athermal Blends . . . . . 139

# CHAPTER I

# INTRODUCTION

## I.1. Basic Concepts of Polymer Physical Chemistry

Polymers represent an interesting class of large-molecular weight molecules which are made up of many repeat units linked together by covalent bonds. Synthetic polymers have numerous applications in material science and engineering, being the main constituent of plastics and composite materials.[1] Additionally, the essential components in bilological systems: DNA, RNA, and proteins are polymeric macromolecules. Since industrial polymers are processed in a molten state, and since biological polymers are typically dissolved in solution, understanding the structure and dynamics of polymer liquids present a unique theoretical challenge with practical interest.

At high concentrations, polymer liquids are viscoelastic fluids characterized by multiple length and timescales of different orders of magnitude. As the degree of polymerization, $N$ is increased, the translational entropy is reduced, but the configurational entropy of each chain is dramatically increased.[2] Local conformations at atomistic length and timescales, including bond vibrations and torsional rotations which lead to isomerization between trans and gauche states, have a typical energy scale of a few $k_BT$. This leads to dynamics on the timescales of picoseconds to nanoseconds. At distances greater than the local chain persistence length, bond orientations become uncorrelated, and the chain is flexible.[3] As

the number monomers becomes large, many chain conformations become possible. These conformations are self-similar over the range of length-scales larger than the persistence length. In fact, polymer chains are an example of a random fractal with a fractal dimension $D = 2$ for ideal random walk chains.[4]

Polymers that contain only one repeating monomer unit are called homopolymers. When two or more different types of monomers are linked together, the polymer chain is referred to as a heteropolymer. Heteropolymers have many unique properties depending on the chemical details of the monomers and the way in which they are arranged on the chain. For example, copolymers can me made by linking two shorter homopolymers together in alternating or random arrangements, or one type of polymer can be grafted onto another to form polymer brushes. Polyelectrolytes are heteropolymers containing charged monomers, and can form micelles, monolayers, or bilayers under certain experimental conditions.

Monomers can be linked together in different ways to created different architectures of chains as shown for example in Figure I.1 Examples include linear chains, rings, star polymers, combs, ladders, or dendrimers. By linking monomers with different chemical properties and interaction strengths in various architectures, a variety of phases and ordered structures are possible.

Most polymeric materials are composites, which are made by blending two distinct polymers together in the molten state. This allows for the custom design of new materials by selecting polymers with a desired mechanical property. It is extremely difficult to predict the mixing behavior of polymer blends since small energy differences between local sites are often amplified by the large number of interacting monomers.

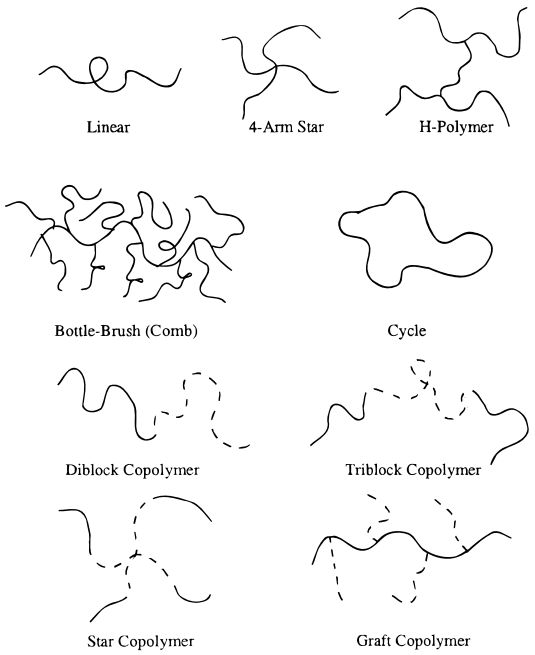


FIGURE I.1. Some typical polymer topologies. Figure reproduced from Ref[2]

The simplest treatment is the Flory-Huggins model which expresses the free energy of mixing as a sum of entropic and enthalpic terms[5]

$$\frac{F}{k_B T} = \frac{\phi_1}{N_1} \ln \phi_1 \frac{\phi_2}{N_2} \ln \phi_2 + \chi \phi_1 \phi_2, \tag{I.1}$$

where $\phi_i$ is the volume fraction of component, $i$, and $N_i$ is the degree of polymerization. The parameter, $\chi$ is the Flory-Huggins parameter which is a nonuniversal reduced temperature, $\chi \sim T^{-1}$. The Flory-Huggins model predicts the critical point with a typical mean-field exponent of 1/2 at

$$\chi_c = \frac{1}{2} \left( \frac{1}{\sqrt{N_1}} + \frac{1}{\sqrt{N_2}} \right)^2 \tag{I.2}$$

This scaling of the critical point, $T_c$ with $N^{-1}$ has been confirmed experimentally[6] and in Monte Carlo simulations by Binder and co-workers.[7] Nonetheless, for real polymer systems the simple Flory-Huggins model does not provide a quantitative description of the phase diagram. Instead, experimental data is customarily fit to Equation I.1 with $\chi$ being a fitting function which may depend on both $N$ and $\phi$ and often includes an entropic component as well. Furthermore, while most mixtures exhibit an upper critical solution temperature (UCST), some systems exhibit a lower critical solution temperature (LCST) for which the mixture is stabile at low temperatures and demixes upon heating. For systems which display an LCST phase behavior, the sign of $\chi$ is negative. One of the goals of polymer theory and simulation work is to predict the phase behavior of multicomponent materials.

## I.2. Liquid State Theory of Polymer Melts

The theoretical framework to describe liquids using integral equation theory was originally pioneered by Kirkwook in the 1930s, and has since been developed extensively throughout the past eighty years[8] Of central importance is the pair correlation function, or radial distribution function, $g(r)$, which describes the fraction of the bulk density found locally about an infinitesimally thin spherical shell of radius, $r$ from a target particle at the origin,

$$g(r) = \frac{1}{\rho} \left\langle \frac{1}{N} \sum_{i}^{n} \sum_{j \neq i}^{n} \delta(\vec{r} - \vec{r}_{ij}) \right\rangle \tag{I.3}$$

where $\vec{r}_{ij} = \vec{r}_i - \vec{r}_j$ and brackets denote an ensemble average. From knowledge of the radial distribution function, along with the assumption of pairwise additivity, all of the thermodynamic properties of the liquid may be calculated,[9] thus the statistical

mechanical treatment of liquids involves obtaining an expression for $g(r)$.

For simple liquids, i.e. liquids without intramolecular structure, the Ornstein-Zernike equation is a convenient starting point to calculate the distribution function.[8]

$$h(r) = c(r) + \int dr' c(r')\rho h(h - r'), \tag{I.4}$$

where h(r) is the correlation function defined as $g(r) - 1$, and is expressed as the convolution of a shorter ranged, direct correlation function $c(r)$ with itself. Equation I.4 serves as the defining relation of the function $c(r)$. In order to solve Equation I.4, one needs an additional relationship, a closure, which relates $c(r)$ to the pair potential, $v(r)$. For simple liquids, one typically adopts the Percus-Yevick approximation,[8]

$$c(r) = g(r)\left(1 - e^{v(r)/k_B T}\right). \tag{I.5}$$

For hard spheres, where $v(r)$ is infinite inside the hard sphere diameter, $d$, and zero outside, the Percus-Yevick equation reduces to

$$\begin{aligned} g(r) &= 0 \qquad r < d \\ c(r) &\approx 0 \qquad r > d \end{aligned} \tag{I.6}$$

Equations I.6 and I.4 together provide a nonlinear integral equation for the pair correlation function of a simple liquid. Another closure relation frequently used for soft potentials is the hypernetted-chain equation (HNC) given by[8]

$$c(r) = -v(r)/k_B T + h(r) - \ln[h(r) + 1] \tag{I.7}$$

The work of Chandler, Anderson, and coworkers generalized integral equation

theory from simple liquids to molecular liquids by developing the Reference Interaction Site Model (RISM).[10–13] In RISM, each molecule consists of several spherically symmetric interaction sites, and the generalized Ornstein-Zernike equation becomes a matrix equation for $g_{\alpha\gamma}(r)$ which is the radial distribution function for sites $\alpha$ and $\gamma$ on different molecules. Importantly, in molecular liquids, the intramolecular distributions have a large effect on determining the intermolecular pair distributions; thus the generalized Ornstein-Zernike equation includes a convolution with the intramolecular distribution, also referred to in the literature as the intramolecular structure factor, or form factor.

Schweizer and Curro have extended RISM theory to describe the equilibrium structure of polymer melts and polymers in solution, by assuming that each interaction site in the polymer chain is identical, i.e. each chain experiences an identical environment, regardless of its unique position in the chain. This simplifies the intractable number of coupled integral equations that would arise from applying RISM to a large molecular weight polymer, by assuming the correlation functions to be independent of the location of the individual sites on the chain, and reduces the problem to a single chain problem. This approach is known as the Polymer Reference Interaction Site Model, or PRISM.[14,15] For a homopolymer fluid of identical monomers, the PRISM Ornstein-Zernike equation becomes, in Fourier space,

$$h(k) = \omega(k)c(k)\omega(k) + \rho\omega(k)c(k)h(k) \tag{I.8}$$

where $\omega(k)$ is the Fourier transform of the intramolecular distribution function, and describes the correlations between sites on the same chain. For chemically realistic models that provide quantitative predictions of the distributions, the PRISM equations are solved numerically. However, a qualitatively informative limiting case,

the polymer thread model, can be evaluated analytically. This approximation is useful when one desires an analytical result for a heavily coarse-grained model as it provides exact expressions which are generally only available for very simple atomic fluids.[8] The analytical thread result will be discussed in detail in Chapter 2 where it is compared with a highly coarse-grained analytical model.

The thread model is defined as an infinitesimally thin Gaussian chain with $N >> 1$, such that the hard sphere diameter, $d \to 0$, the statistical segment lenght, $\sigma \to 0$ and the density, $\rho \to \infty$, in such a manner that the quantity $\rho d^3$ and the aspect ratio $\sigma/d$ are both finite and nonzero. The intramolecular distribution is given by the Pade approximation for a Gaussian chain[16] given in Fourier space as

$$\omega(k) \approx \frac{1}{k^2\sigma^2/12 + 1/N} \tag{I.9}$$

The Percus-Yevick closure given by Equation I.5 implies that $g(r \to 0) = 0$ and $C(r > 0) = 0$. Substitution of Equation I.9 into Equation I.8 with the closure relation gives an analytical solution for the total correlation function as

$$\rho\sigma^3 h(r) = \frac{3}{\pi r}\left[e^{-r/\xi_\rho} - e^{-r/\xi_c}\right] \tag{I.10}$$

where $\xi_c$ is the lengthscale of the "correlation hole", $\xi_c = R_g/\sqrt{2}$, and $\xi_\rho$ is the lengthscale of the density fluctuations given as[14]

$$\xi_\rho^{-1} = \xi_c^{-1} + \frac{1}{3}\pi\rho\sigma^3. \tag{I.11}$$

The lengthscale, $R_g$ is the polymer radius of gyration defined as $R_g = \sqrt{N/6}\sigma$. The PRISM formalism has been generalized to treat polymer blends by Curro and

Schweizer[15] In the case of a homopolymer mixture the PRISM equation becomes a matrix equation

$$\mathbf{H}(k) = \Omega(k)\mathbf{C}(k)\left[\Omega(k) + \mathbf{H}(k)\right] \tag{I.12}$$

for the three independent intermolecular correlation functions, $h_{AA}(r)$, $h_{AB}(r)$, and $h_{BB}(r)$ in real space. Interestingly, one can make a direct comparison with scattering experiments and the Flory-Huggins parameter. Introducing a segmental volume ratio, $R_v = v_A/v_B$, it is straightforward to derive[17]

$$\chi_S = (\rho/2)(\phi_A R_v^{-1/2} + \phi_B R_v^{1/2})^{-1}\left[R_v^{-1}\hat{C}_{AA}(0) + R_v\hat{C}_{BB}(0) - 2\hat{C}_{AB}(0)\right] \tag{I.13}$$

Importantly, Equation I.13 is independent of the closure approximation used, and is a direct result of the Ornstein-Zernike matrix equation. In specifying a closure for polymer blends, Yethiraj and Schweizer[18,19] have formulated "molecular" closures which are essential to obtaining the correct scaling of the critical temperature with $N$.

### I.3. Perspectives on Coarse-Graining Models

In addition to theoretical models, such as integral equation theory, molecular dynamics (MD) simulations have become instrumental in developing and testing theories in polymer physics since simulations can provide direct access and physical insight into the time evolution of complex fluids.[20–22] In MD simulations, one has access to the positions and velocities of each atom and its trajectory in phase space. Correlation functions can be readily calculated from simulation trajectories and compared with experiments. Additionally, any physically observable property can be extracted from the simulation including viscosity, equation of state, diffusion

coefficient, structure, and time correlation functions.

However, explicit atom MD simulations are computationally costly which limits their range of applicability to small length and time-scales. This limitation has stimulated the development of numerous coarse-graining methods, which are highly efficient because they represent the system at a lower resolution, and thus greatly reduce the number of degrees of freedom.[23] As discussed in Section I, polymers are multi-scale in nature: bond lengths are typically of the order of Angstroms with bond vibrations occurring on the order of femtoseconds; a single polymer chain radius of gyration is on the order of nanometers with typical relaxation times on the order of nanoseconds; polymer networks can be of the order of several micrometers with extremely long relaxation times for dense glassy systems.[24] At large time and length scales emergent phenomena such as phase transitions or self-assembly become apparent, and one becomes interested in the effective interactions and driving forces that produce ordered structures in these complex systems. In order to investigate these disparate time and length scales it is necessary to adopt a multiscale approach for which a polymer chain is represented at varying degrees of detail.

An extremely successful approach has been the United Atom (UA) description where each moiety of type $C$, $CH$, $CH_2$, or $CH_3$ is represented as an effective unit.[25–28] The UA description is useful because polyolefines can be fully represented as a collection of these sites. A similar widely-used approach, the Kremer-Grest model, maps a polymer chain onto a series of connected beads linked via harmonic interactions.[29,30] These low-level models are useful in that parameters have been optimized to reproduce experimentally observable quantities, and they provide a modest gain in computational time from all-atom MD simulations. Nonetheless, they are still limited to the order of a few hundred nanoseconds and dense liquids

of chains are extremely difficult to equilibrate due to chain entanglements. Hence a more extreme level of coarse graining is needed to enable simulations to reach the largest time and length scales of interest. Two main challenges become apparent when seeking a coarse-grained model. First, it is not often obvious how to link simulations of more detailed models with more coarse-grained ones, such that the behavior of the system at both levels of detail inform one another and the behavior at both scales can be resolved to obtain a complete description of the system at all scales of interest. The second challenge is how to determine the effective potential energy between interacting sites in the CG model. It is important to note that the goal in devising a coarse-grained model is to reproduce the physically observable properties of the more detailed system. Several models to determine the effective CG potential are widely used in the literature. All of these methods require an all-atom simulation against which the CG potential is numerically optimized.

One of the most widely used coarse-graining method in the literature is the Iterative Boltzmann Inversion (IBI) method[31,32] which makes use of a uniqueness theorem from Henderson[33] which states that for a given radial distribution function, $g(r)$, there is a unique pair potential, $v(r)$ which will reproduce it. The IBI approach attempts to determine the pair potential that will reproduce a target radial distribution function through an iterative optimization scheme. First, an all atom simulation is performed, and a target radial distribution function, $g_T(r)$ is calculated. The coarse-grained potential is then estimated as the direct Boltzmann inversion of the distribution, $v_{cg}(r) = -k_B T \ln g_T(r)$. This potential is used in a coarse-grained simulation, and the radial distribution function $g_{cg}$ is calculated. The pair potential

is then updated according to

$$v_{\text{new}}(r) = v_{\text{old}}(r) - k_B T \ln\left(\frac{g_T(r)}{g_{cg}(r)}\right) \tag{I.14}$$

The process is repeated until $v_{cg}(r)$ converges, i.e. the coarse-grained simulation reproduces the target radial distribution function.

An alternative approach is the force matching approach developed by Izvekov and Voth.[23,34–36] One again begins with an all-atom reference simulations and numerically optimizes the coarse-grained model against it. However, the force-matching scheme optimizes the average force on each coarse-grained interaction site against the expected sum of the forces from the all-atom representation

$$\langle F_I \rangle = -\frac{\partial v_{cg}(r)}{\partial r_I} \tag{I.15}$$

where the fictitious site is labeled by the index, $I$, and the brackets denote an ensemble average in the all-atom simulation. One then minimizes the least-squared sum of the difference between the forces in the two representations with respect to the free parameters in $v_{cg}(r)$.

The "holy grail" of coarse-graining would be to determine the effective potential from the knowledge of the atomistic structure and interactions alone, without the need for an all-atom simulation. This would alleviate the need to perform computationally costly all-atom simulations against which to parameterize the coarse-grained model. The goal of the Guenza group has been to develop a systematic coarse-graining strategy from liquid state integral equation theory that does not rely on any numerical optimization scheme. The approach originates from a mapping suggested by Krackoviack et al.[37] which formally relates the center of

mass distributions of a polymer melt with the distributions of monomers. Yatsenko et al.[38,39] used this formalism to derive an analytical theory for the structural correlations of Gaussian chains. The model has been extended to soft dumbbell representations of diblock copolymer chains.[40] Recently, this formalism has been extended by Clark et. al.[41] to a multi-block representation, where the polymer chain is described by an arbitrary number of fictitious sites. These distributions are used to derive a coarse-grained potential between fictitious sites which is then implemented in MD simulations of the coarse-grained system without the need to perform computationally costly all-atom simulations.

### I.4. Organization of Dissertation

This dissertation discusses the coarse-graining and multiscale modeling procedure for dense polymer systems developed in the Guenza group. Chapter II will briefly summarize the theory to derive the effective potential and will serve to provide relevant context to the subsequent chapters. This chapter is based from material co-authored with A. Clark and M. G. Guenza. Chapters III and IV are devoted to demonstrating the thermodynamic consistency of the model. Both chapters will address fundamental issues of coarse-graining and how various thermodynamic quantities are affected in the coarse-graining procedure. Chapter III will focus on an analytical derivation of the equation of state for the coarse-grained model and will present a comparison to the analytical Gaussian thread limit of PRISM theory. This chapter is co-authored with A. Clark and M. G. Guenza. Chapter IV presents numerical results which show quantitative agreement with a united atom model of polyethylene chains. Chapter V discusses the procedure to derive the potential for chemically realistic polymer models. Both Chapter IV and V are co-authored with A.

Clark, J. Copperman, and M. G. Guenza. Chapter VI presents a multiscale modeling method to combine information from the two levels of detail, which provides a clear way to link information from different simulations. Chapter VII will then discuss coarse-grained simulations of polymer blends. Chapters VI and VII are both co-authored with I. Y. Lyubimov and M. G. Guenza. A brief conclusion discusses the relevance of the completed work and anticipates future developments of the coarse-grained model.

# CHAPTER II

# THEORETICAL BACKGROUND: HIGHLY COARSE GRAINED REPRESENTATIONS OF POLYMER MELTS

The material presented in this section briefly summarizes previous work in deriving an analytical coarse-graining procedure based on liquid state theory for polymer melts. Each coarse-grained particle is located at the center of mass of a polymer subchain. Much of this section is adapted and summarized from "Effective potentials for representing polymers in melts as chains of interacting soft particles," co-authored with Anthony Clark and Marina Guenza which is publised in the Journal of Chemical Physics in 2013[41] This chapter provides relevant background and foundational material for subsequent chapters.

## II.1. Generalized PRISM Ornstein Zernike Equation

For a chain of $N$ monomers, with radius of gyration, $R_g = \sqrt{N/6}\sigma$, and monomer density $\rho_m$, we divide the chain into $n_b$ number of coarse-grained (CG) sites with $N_b = N/nb$ number of underlying monomers per CG site. The coarse-graining procedure begins by solving a generalized PRISM Ornstein Zernike equation of Equation I.8, and introducing fictitious interaction sites at the center of mass of a group of real monomer sites. Fictitious interaction sites are assumed to have no

site-site direct correlation. The resulting matrix equations in Fourier space are

$$h^{mm}(k) = \omega^{mm}(k)c(k)\left[\omega^{mm}(k) + n_b\rho_{ch}h^{mm}(k)\right] \quad \text{(II.1)}$$

$$h^{bm}(k) = \omega^{bm}(k)c(k)\left[\omega^{mm}(k) + n_b\rho_{ch}h^{mm}(k)\right] \quad \text{(II.2)}$$

$$h^{mb}(k) = \omega^{mm}(k)c(k)\left[\omega^{mb}(k) + n_b\rho_{ch}h^{mb}(k)\right] \quad \text{(II.3)}$$

$$h^{bb}(k) = \omega^{bm}(k)c(k)\left[\omega^{mb}(k) + n_b\rho_{ch}h^{mb}(k)\right], \quad \text{(II.4)}$$

where $\rho_c = \rho_m/N$ is the density of chains. Throughout this dissertation we assume a chain-averaged description, such that fictitious sites along the chain are identical and end effects can be neglected. Correlations between monomers are denoted by a superscript $m$ and correlations between CG sites are denoted with a superscript, $b$. An illustration of the coarse-graining procedure is shown in Figure II.1. Intermolecular distributions between block centers are denoted $h^{bb}(k)$ and between monomers as $h^{mm}(k)$. The normalized intramolecular distributions are denoted with $\Omega^{mm}(k) = \omega^{mm}(k)/N$ being the distributions of monomers on a single chain, $\Omega^{bm}(k) = \omega^{bm}(k)/N$ the distribution of monomers about a block center, and $\Omega^{bb}(k) = \omega^{bb}(k)/N$ the intramolecular distribution of block centers.

The monomer direct correlation function is taken to have negligible k-dependence in the range of interest, hence $C(k) = C(k = 0) = c_0$. From the Ornstein Zernike relations in Equation II.4, after some algebra one obtains an expression for the block-block intermolecular correlation function[42]

$$\hat{h}^{bb}(k) = -\frac{N_b n_b^2 \Gamma_b}{\rho_m} \frac{(\hat{\Omega}^{bm}(k))^2}{1 + n_b\Gamma_b\hat{\Omega}^{mm}(k)}, \quad \text{(II.5)}$$

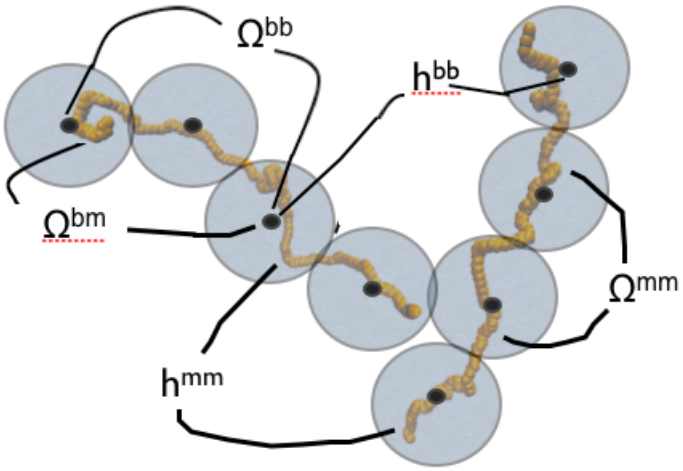


FIGURE II.1. Schematic depiction of the intermolecular and intramolecular distribution functions between monomers (mm), fictitious sites (bb), and monomers about fictitious sites (bm).

where $N_b$ is the number of monomers per block and $n_b$ is the number of blocks, and the parameter $\Gamma_b = -N_b\rho_m c_0$. Equation II.5 is general and does not assume anything about the underlying monomer distributions. As a next step, we assume the intramolecular distributions obey Gaussian statistics, which is valid in melts at distances much larger than the persistence length, for which the central limit theorem applies (roughly $N_b > 30$). Clark and Guenza have derived expressions for the intramolecular distributions.[42] The block-monomer intramolecular distribution function from this previous work is given as

$$\begin{aligned} \hat{\omega}^{bm}_{\alpha\beta}(k) &= \hat{\omega}^{bm}_{\gamma}(k) \\ &= \begin{cases} \left(\frac{N_b\sqrt{\pi}}{R_{gb}k}\right)\left(erf\left[\frac{1}{2}kR_{gb}\right]\right)e^{-(R^2_{gb}k^2/12)} & \text{if} \quad \gamma = 0 \\ \frac{N_b}{k^2R_g^2}e^{-1/6[Q_\gamma k^2]}(1-e^{-R^2_{gb}k^2}) & \text{if} \quad \gamma \neq 0 \end{cases} \end{aligned} \tag{II.6}$$

with $\gamma = |\alpha - \beta|$ as the separation index between sites, and $Q_\gamma = 2R_{gb}^2 + 3R_{gb}^2/N_b + R_{gb}^2/N_b^2 + 6R_{gb}^2|\beta - \alpha - 1| \approx 2R_{gb}^2 + 6(\beta - \alpha - 1)R_{gb}^2$, with $R_{gb}$ being the block radius of gyration, $R_{gb} = R_g/\sqrt{n_b}$. Taking the block average over all sites $\alpha$ and $\beta$ gives

$$\hat{\Omega}^{bm}(k) = \frac{1}{n_b}\left[\frac{\sqrt{\pi}}{k} Erf\left(\frac{k}{2}\right) e^{-\frac{k^2}{12}} - 2\left(\frac{e^{-n_b k^2} - n_b e^{-k^2} + n_b - 1}{k^2 n_b (e^{-k^2} - 1)}\right) e^{-k^2/3}\right] , \quad \text{(II.7)}$$

where the wave vector, $k$, is expressed in units of $R_{gb}^{-1}$. The monomer intramolecular distribution is given as the normalized Debye equation[16]

$$\hat{\Omega}^{mm}(k) = \frac{2}{n_b^2 k^4}(k^2 n_b - 1 + e^{-n_b k^2}), \quad \text{(II.8)}$$

and the intramolecular distribution between block centers is obtained by taking the average over all sites of the result from our previous work[42]

$$\hat{\Omega}^{bb}(k) = \frac{1}{n_b} + 2\left[\frac{e^{-n_b k^2} - n_b e^{-k^2} + (n_b - 1)}{n_b^2 (e^{-k^2} - 1)^2}\right] e^{-2k^2/3} , \quad \text{(II.9)}$$

with $\rho_b$ is the number density of blocks, $\rho_b = \rho_m/N_b$. Substitution of Equation II.7 and Equation II.8 into Equation II.5 gives an expression for the intermolecular block distribution that depends only on the structural and thermodynamic parameters of the model which are $N_b$, $n_b$, $T$, $\rho_m$, and again $k$ in units of $R_{gb}^{-1}$, as well as the monomer direct correlation parameter $c_0$.

To obtain the direct correlation function between coarse-grained sites, $c^{bb}(k)$, we substitute Equation II.9 and Equation II.5 into the PRISM Ornstein-Zernike equation for the coarse grained liquid,

$$\hat{h}^{bb}(k) = n_b \hat{\Omega}^{bb}(k)\hat{c}^{bb}(k)\left[n_b \hat{\Omega}^{bb}(k) + \rho_b \hat{h}^{bb}(k)\right] , \quad \text{(II.10)}$$

and solve for the direct correlation function to obtain

$$\hat{c}^{bb}(k) = \frac{c_0 N_b^2 (\hat{Y}^{bm}(k))^2}{1 + \Gamma_b \hat{Z}^{bm}(k)} \ , \tag{II.11}$$

with the notation

$$\hat{Y}^{bm}(k) = \hat{\Omega}^{bm}(k)/\hat{\Omega}^{bb}(k) \ , \tag{II.12}$$

and

$$\hat{Z}^{bm}(k) = n_b \left[ \hat{\Omega}^{mm}(k) - (\hat{\Omega}^{bm}(k))^2 / \hat{\Omega}^{bb}(k) \right] \ . \tag{II.13}$$

with $k$ in units of $R_{gb}^{-1}$.

## II.2. Soft Sphere Limit

Much of the work of this dissertation will consider the particular limiting case where each polymer chain is represented as a single coarse-grained site. This case is termed the soft sphere model and is characterized by $n_b = 1$ and $N_b = N$. This limiting case is informative in that basic features and properties of the coarse-graining method can be investigated without unnecessary complications. Furthermore, the model maps the complex polymer fluid onto a simple single component fluid, meaning that we apply the extensive theoretical framework of simple liquids to this model. Figure II.2 illustrates the soft sphere limit where the fictitious site is now the center of mass of the whole chain. For this reason we use the superscript "cc" to indicate correlations between center of mass sites.

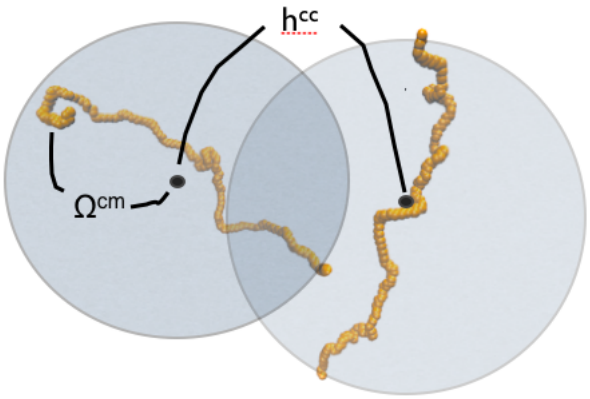


FIGURE II.2. Schematic depiction of the soft sphere limit where there are now just the intermolecular distributions between fictitious sites $h^{cc}$ and intramolecular distributions of monomers about the center of mass $\Omega^{cm}$.

The total and direct correlations in the soft sphere model are

$$\hat{h}^{cc}(k) = -\frac{N\Gamma}{\rho_m}\frac{(\hat{\Omega}^{cm}(k))^2}{1+\Gamma\hat{\Omega}^{mm}(k)} \ , \tag{II.14}$$

with $\Gamma = -N\rho_m c_0$, and $c_0$ is the $k = 0$ value of the monomer-level PRISM direct correlation function. Again, $k$ is expressed in reduced units of $R_g^{-1}$. The intramolecular monomer-monomer distribution function is given by the Debye equation[16]

$$\hat{\Omega}^{mm}(k) = \frac{2}{k^4}\left(k^2 - 1 + e^{-k^2}\right) \ , \tag{II.15}$$

while the cm monomer distribution function is defined as[43]

$$\hat{\Omega}^{cm}(k) = \frac{\sqrt{\pi}}{k}\mathrm{erf}(\frac{k}{2})e^{-\frac{k^2}{12}} \ . \tag{II.16}$$

The direct correlation function, using the definitions Eqs.II.12 and II.13 extended to a soft-sphere coarse-grained representation, reduces to

$$\hat{c}^{cc}(k) = \frac{c_0 N^2 (\hat{Y}^{cm}(k))^2}{1 + \Gamma \hat{Z}^{cm}(k)} \ , \tag{II.17}$$

with $\hat{Y}^{cm}(k) = \hat{\Omega}^{cm}(k)$ and $\hat{Z}^{cm}(k) = \hat{\Omega}^{mm}(k) - \left(\hat{\Omega}^{cm}(k)\right)^2$.

## II.3. Analytical Approximation of the Effective Potential

Once the distribution functions are calculated, the effective potential is determined by adopting a closure for the coarse-grained fluid. Since the coarse-grained potentials remain finite even at small separation distances and never become much larger than a few $k_B T$, we adopt the HNC closure is known to give a good approximation to the relationship between the direct correlation and the pair potential for soft systems.[8] This defines the potential as

$$V^{bb}(r) = -k_b T \left[ c^{bb}(r) - h^{bb}(r) + ln(1 + h^{bb}(r)) \right] \ . \tag{II.18}$$

In order to obtain an analytical approximation of the potential, we assume that $|h^{bb}(r)| << 1$, which is true at large separations ($r >> 1$ in units of $R_{gb}$) and at any separation for representations with large $N_b$ and high densities. Under these conditions, Equation II.18 simplifies to

$$V^{bb}(r) \approx -k_b T c^{bb}(r) \ . \tag{II.19}$$

This formula is referred to as the mean spherical approximation (MSA) or random phase approximation in the literature.[44] In our formalism it is arrived at as a mean-field approximation since it assumes that the liquid is isotropic at large distances, $g(r) = 1$.

In the limit of large separation distances, $k$ is small, and the quantity, $\hat{Z}^{bm}(k) = \hat{\Omega}^{mm}(k) - (\hat{\Omega}^{bm}(k))^2/\hat{\Omega}^{bb}(k)$ that appears in the denominator of Equation II.11 can be expanded about $k = 0$. Factoring out the overall factor of $\Gamma_b$, re-scaling wave vector units to fix the width of the peak, $k \rightarrow k\Gamma_b^{1/4}$, and expanding in powers of $1/\Gamma_b^{1/4}$ around $1/\Gamma_b^{1/4} \rightarrow 0$ gives

$$\hat{c}^{bb}(k) \approx \frac{-N_b\Gamma_b}{\rho_m}\left[\frac{45}{45+\Gamma_b k^4} + \frac{5k^2}{28}\frac{13\Gamma_b k^4 - 3780}{(\Gamma_b k^4+45)^2}\right] \ ... \tag{II.20}$$

Taking the inverse transform integral and substitution into Equation II.19 leads to an analytical approximation for the potential which is valid at large r (in units of $R_{gb}$),

$$V^{bb}(r)\approx\frac{k_BTN_b\Gamma_b}{2\pi^2\rho_m R_{gb}^3 r}\int_0^\infty\left(k\sin(kr)\left[\frac{45}{45+\Gamma_b k^4}+\frac{5k^2}{28}\frac{13\Gamma_b k^4-3780}{(\Gamma_b k^4+45)^2}\right]\right)dk$$

$$=k_BT\Big[\left(\frac{45\sqrt{2}N_b\Gamma_b^{1/4}}{8\pi\sqrt{3}\sqrt[4]{5}\rho_m R_{gb}^3}\right)\frac{\sin(Q'r)}{Q'r}e^{-Q'r} - \left(\frac{\sqrt{5}N_b}{672\pi\rho_m\Gamma_b^{1/4}R_{gb}^3}\right)\Big[(13Q^3(Q'r-4))cos(Q'r)$$

$$+\left(\frac{945+13Q^4}{\Gamma_b^{1/4}}\right)r\sin(Q'r)+\frac{945r}{\Gamma_b^{1/4}}cos(Q'r)\Big]\frac{e^{-Q'r}}{Q'r}\Big] \ , \tag{II.21}$$

where $Q' = 5^{1/4}\sqrt{3/2}\Gamma_b^{-1/4}$ and $Q \equiv Q'\Gamma_b^{1/4}$ . Equation II.21 is the main result of this chapter and its importance cannot be understated. It presents an analytical potential that maps a polymer onto a collection of arbitrary numbers of coarse-grained sites,

$n_b$, under the assumption that the underlying monomers obey Gaussian statistics. All of the parameters entering into the model are known from the underlying atomistic description, thus it is clear how to relate this potential to the underlying monomer picture. It is straightforward to obtain the soft sphere limit of this potential, by taking $n_b = 1$ and $N_b = N$, such that $\Gamma_b = \Gamma = -\rho_m N c_0$.

## II.4. Conclusion

This chapter has presented an analytical solution for the effective potential acting between block centers in a coarse-grained representation of a polymer melt. Given only a single block per chain, the multi-block potential reduces to a soft sphere model. The remainder of the dissertation will focus on properties of the coarse-grained potential which can be used in coarse-grained simulations of complex macromolecular fluids. In particular the next chapter will discuss the thermodynamics of the soft sphere limit in detail.

# CHAPTER III

# THERMODYNAMIC CONSISTENCY BETWEEN ANALYTICAL INTEGRAL EQUATION THEORY AND COARSE-GRAINED MOLECULAR DYNAMICS SIMULATIONS OF HOMOPOLYMER MELTS

Having summarized the derivation of the analytical coarse-grained potential in Chapter II, Chapter III presents a derivation of the thermodynamic properties of the soft sphere coarse-grained model, including the equation of state, for the soft sphere description of the polymeric liquid. In order to obtain an analytically tractable solution, the thermodynamic properties for the coarse-grained description are derived for a Gaussian thread polymer as the underlying monomeric description. This material is adapted from a paper co-authored with A. Clark, I. Y. Lyubimov, and M. G. Guenza[45]

## III.1. Thermodynamic Consistency in Density Dependent Potentials

While coarse-graining invariably aims at reducing the complexity of the underlying atomistic system, it is nonetheless important that a mesoscopic description correctly reproduces thermodynamic properties of the real system. Many coarse-graining methods have been developed in recent years[46–51] with a vast majority of them being numerical, meaning that the effective pair potential is numerically optimized to reproduce some particular property calculated from a more detailed-level simulation. As discussed in Chapter I, a widely used procedure is the Iterative Boltzmann Inversion (IBI) technique,[31] where an initial guess of the effective potential, $v_0(r)$, usually taken as the potential of mean force $[v_0(r) = -k_B T \ln g(r)]$ is used in a trial simulation, yielding a new radial distribution function, $g_0(r)$,

which is different from the target $g(r)$. This provides a correction term to the pair potential by Boltzmann inversion of the difference in the radial distribution functions, $k_B T \ln[g_0(r)/g(r)]$. This procedure is then iterated until the effective pair potential reproduces the correct target radial distribution function (RDF) as measured in an atomistic simulation. Examples of other structure-based approaches include the inverse Monte Carlo method,[52] the multiscale coarse-graining (MS-CG) approach, which is based on a force-matching procedure,[35,36] and the structure-based method of Kremer and co-workers.[50,53] Another approach of Nielsen, *et al.* optimizes coarse-grained potentials to match experimental bulk density and surface tension values,[54] while a coarse-grained model for DNA has been proposed for which the force field parameters are obtained through an iterative procedure to match experimental melting temperatures.[55,56]

The abundance of these coarse-graining procedures in the literature have revealed two deep-seated problems inherent to any numerical optimization scheme. Following the argument outlined by Louis,[57] the first is a problem of *transferability*, namely, that an effective pair potential optimized at one set of thermodynamic conditions will not generally be transferable to another set of conditions. This is a consequence of coarse-graining, as the effective potential is a free energy of the system, and thus is state-dependent. In principle, the pair potential optimized at one density, temperature, and composition is not the same as that optimized at any other density, temperature, and composition, and one would need to optimize a new effective potential for each thermodynamic state of the system, which defeats the overall purpose of coarse-graining since the potential must be optimized to match an atomistic-level simulation. Typically, as the explicit state-dependence is unknown, a numerically optimized pair potential will have a limited range of applicability to

a subset of states close to the one at which the potential was derived.[58,59] This feature limits the applicability of coarse-grained potentials for studying systems at conditions far from those of conventional simulations, such as systems approaching the glass transition.

The second problem for numerical coarse-graining methods is a problem of *representability*. It has been theoretically shown by Henderson that any isotropic potential which reproduces the correct pair structure of a fluid is unique up to a constant.[33] Consequently, for any given structure, there is one unique effective pair potential which will reproduce the correct radial distribution function, and in principle any thermodynamic property of interest, since knowledge of the structure (along with the proper closures for integral equations), completely specifies the thermodynamic state of the system.[9] However, even at the correct state conditions, numerical potentials optimized to reproduce one quantity (for example, the correct RDF), will not necessarily reproduce any other, such as the correct pressure or internal energy. Consequently, one obtains a different effective potential depending on the property against which the coarse-grained system was optimized. For example, Johnson *et al.* found that coarse-grained potentials for water, optimized to reproduce the correct radial distribution function, do not reproduce the correct average internal energy or virial pressure.[60]

There are at least two reasons why numerical coarse-grained potentials fail to resolve thermodynamic properties even though they may produce the apparent correct structure. The first problem is due to an imperfect representation of the target RDF, which will introduce errors into the effective potential due to the optimization scheme. This problem is particularly difficult to avoid in numerical optimization methods, since the procedure depends on an atomistic simulation, which

always introduces some error into the calculation. This is important as it has been observed that visibly different potentials may produce structures with near identical radial distribution functions to within line thickness.[61] On the other hand, many thermodynamic properties depend sensitively on the form of the interaction potential. Thus, although small errors introduced into the numerical optimization procedure do not appear to be important in determining the correct radial distribution function, they become important in the calculation of other thermodynamics properties.[62] As a result, it is often necessary to post-optimize the system to obtain the correct thermodynamics after structural optimization is complete.[51]

A second reason for the representability problem, stems from the fact that during coarse-graining, many microscopic degrees of freedom are averaged out, resulting in a simplified energy landscape and different entropy. Because it is not possible to know how a specific numerical coarse-grained potential depends on its state parameters, it is not clear how to make corrections when one expects the two levels of description to be different, for example in terms of the entropy of the system.[63]

Having an analytical solution for the coarse-grained potential allows us to calculate thermodynamic quantities analytically and address the issues of thermodynamic consistency without the need for any numerical simulations which may introduce errors. Importantly, the state-dependence of the effective potential is explicitly known, and thus the transferability problem is solved outright. Secondly, having an analytical solution avoids the need to optimize the effective potential against a more detailed description, hence avoiding the inclusion of numerical errors arisinging from the atomistic simulation. Finally, having an analytical formula essentially solves the representability problem, since any thermodynamic quantity can be calculated analytically. The resulting expression can then be compared to a

more detailed model and the correction terms can be directly identified if the two levels of description differ. For, example, we have recently developed such a procedure to reconstruct the "real" friction and entropy from a coarse-grained simulation to reproduce the correct center of mass displacement as measured in experiments and atomistic simulations.[64]

## III.2. Theoretical Background: Coarse-Grained Model and Effective Pair Potential

We consider a homopolymer fluid of $n$ chains and molecular number density, $\rho_{ch}$, where each chain consists of $N$ sites, or monomeric units. This description is consistent with an united atom simulation model, where each site is taken to be a $CH_x$ group with $x = 1$, 2, or 3, or with a theoretical representation of the polymeric chain as a bead-spring model or as a thread model (see below). The overall size of the macromolecule is defined by the chain radius of gyration, $R_g$, which also defines the segmental size, $\sigma = \sqrt{6/N}R_g$. This level of description we term the monomer level of description throughout this work.

At the monomer level of description, pair correlation functions are related through the Polymer Reference Inter Site Model (PRISM) site-averaged Ornstein-Zernike equation,[15]

$$\hat{h}^{mm}(k) = \hat{\omega}^{mm}(k)\hat{c}^{mm}(k)[\hat{\omega}^{mm}(k) + \rho\hat{h}^{mm}(k)], \tag{III.1}$$

where the superscript denotes monomer-monomer (mm) interactions. Here $h^{mm}(k)$ is the Fourier transform of the total correlation function, $h^{mm}(r) = g^{mm}(r) - 1$, $c^{mm}(k)$ is the direct correlation function, $\omega^{mm}(k)$ is the intrachain structure factor, and $\rho$ is

the monomer site density, given as $\rho = N\rho_{ch}$. A convenient model of the monomer structure for our purposes here, is the PRISM thread model, which treats each polymer chain as an infinite thread of vanishing thickness, such that the monomer hard core diameter, $d \to 0$, and the segment number density $\rho \to \infty$, while the quantity $\rho d^3$ remains finite. Under these simplifying conditions, the direct correlation function becomes a Dirac-delta function in real space such that, $\hat{c}^{mm}(k) = c_0$, and $c^{mm}(\mathbf{r}) = c_0\delta(\mathbf{r})$. The solution of Equation III.1, subject to the constraints that $g^{mm}(r \to 0) = 0$, yields the monomer pair distribution function,

$$g^{mm}_{thread}(r) = 1 + \frac{3}{\pi\rho\sigma^2 r}\left[e^{-r/\xi_\rho} - e^{-r/\xi_c}\right]. \tag{III.2}$$

where $\xi_\rho$ is the length scale of density fluctuations defined as $\xi_\rho^{-1} = \xi_c^{-1} + 2\pi\rho_{ch}R_g^2$, and $\xi_c = R_g/\sqrt{2}$ is the length scale of the correlation hole.[3] The direct correlation strength parameter, $c_0$, in the thread model is given by,[65]

$$c_{0,thread} = -\frac{\pi\sigma^3}{3\sqrt{3N}} - \frac{\pi^2\rho\sigma^6}{108}. \tag{III.3}$$

The thread model, which is the model adopted in field theories, has been shown to capture correctly several key features of the large-scale liquid structure, and to do so consistently both at the monomer and at the coarse-grained levels of soft-sphere and multi-blobs. The thread model is adopted here for analytical convenience, as it allows for the direct comparison of the formal expressions derived at the monomer and CG levels. Although simple, the model nonetheless represents many key features of the behavior of real chains in the scaling limit of $N \to \infty$.

We now turn to our *coarse-grained description* of the polymer melt. This description we term a mesoscale description since it represents a fluid with resolution

somewhere in between a fully atomistic model and a continuum model. By assuming Gaussian chain distributions for the intramolecular form factors, which is a reasonable approximation for polymer melts, Yatsenko, *et al.*[38] derived an analytical expression for the total distribution function between center of mass sites, $h^{cc}(k)$. For chains of $N \geq 30$, the resulting pair distribution function in real space between polymer center of masses can be approximated as[66]

$$g^{cc}_{thread}(r) \approx 1 - \frac{39}{16}\sqrt{\frac{3}{\pi}}\frac{\xi_\rho}{R_g}\left(1+\sqrt{2}\frac{\xi_\rho}{R_g}\right)\left[1-\frac{9r^2}{26R_g^2}\right]e^{-3r^2/4R_g^2}. \tag{III.4}$$

Equation III.4 has been shown to quantitatively describe the structure of the polymer melt on length scales of the order of $R_g$ and larger, as compared with both atomistic and coarse grained simulations.[38,66]

Evaluation of thermodynamic properties requires knowledge of the bare intermolecular pair potential between coarse-grained units. In the soft sphere model, the polymers are described as a simple liquid of soft colloids, and the direct correlation function in reciprocal space, $c^{cc}(k)$, reads

$$\hat{c}^{cc}(k) = \frac{\hat{h}^{cc}(k)}{\hat{S}^{cc}(k)}, \tag{III.5}$$

where $\hat{S}^{cc}(k) = 1 + \rho_{ch}\hat{h}^{cc}(k)$ is the center of mass static structure factor.[38] The effective pair potential may be obtained with substitution of Equation III.4 and Equation III.5 into the HNC closure, Equation I.7. In our previous papers the potential was solved numerically, and used as an input into classical molecular dynamic simulations of soft interacting spheres. Those mesoscale simulations (MS) produced center-of-mass pair distribution functions in agreement not only with the center of mass pair distribution analytical expressions, but also with the $g^{cc}(r)$

calculated directly from united atom simulations of the same polymer system, further validating the proposed procedure.[47,66] Because they reproduce the polymer structure at intermediate to large length-scales those simulations we term mesoscale simulations.

Although Equation I.7 can be solved numerically from $g^{cc}(r)$, an explicit analytical form of the potential is desirable as it facilitates the evaluation of thermodynamic quantities of interest. For this we use the analytical approximation for the direct correlation function in the limit of high degree of polymerization and high monomer density which was presented in Chapter II. The total correlation function can be written as

$$\hat{h}^{cc}(k) = \frac{c_0[\hat{\omega}^{cm}(k)]^2}{1 - \rho c_0 \hat{\omega}^{mm}(k)} \ . \tag{III.6}$$

Substitution of Equation III.6 into the expression for the inverse static structure factor, given for soft colloids as $[S^{cc}(k)]^{-1} = 1/[1 + \rho_{ch} h^{cc}(k)]$, leads to an analytical expression for $[S^{cc}(k)]^{-1}$, which can be rewritten in the form

$$[\hat{S}^{cc}(k)]^{-1} = \Gamma \left[ \frac{1/\Gamma + \hat{\Omega}^{mm}(k)}{1 + \Gamma \hat{\Omega}^{mm}(k) - \Gamma [\hat{\Omega}^{cm}(k)]^2} \right], \tag{III.7}$$

where the parameter $\Gamma \equiv -N c_0 \rho$ and the $\hat{\Omega}(k)s$ are the intramolecular form factors normalized by $N$, $(\hat{\Omega}(k) = \hat{\omega}(k)/N)$.

We represent the intramolecular distribution functions as following a Gaussian form, which is an approximation correct for $N > 30$ in a melt, and by expanding the difference, $\hat{\omega}^{mm}(k)/N - [\hat{\omega}^{cm}(k)/N]^2$, in a Taylor series about $k = 0$. To leading

order, the effective potential for soft spheres in real space is

$$v^{cc}_{(0)}(r) \approx k_B T \frac{45}{(5^{1/4})8\pi}\sqrt{\frac{2}{3}}\frac{\Gamma^{1/4}}{\rho_{ch}R_g^3}\frac{\sin(Qr)}{Qr}e^{-Qr}, \tag{III.8}$$

where the numerical factor $Q = 5^{1/4}\sqrt{3/2}/(\Gamma^{1/4}R_g)$. For shorter chains, a second order correction term has to be included

$$v^{cc}_{(1)}(r) = -k_B T \frac{\sqrt{5}}{672\pi\rho_{ch}R_g^3\Gamma^{1/4}}[(\frac{945r}{\Gamma^{1/4}R_g}(\cos(Qr)+\sin(Qr)) + 13Q_{rs}^3(Qr-4)\cos(Qr) + \frac{13Q_{rs}^4 r}{\Gamma^{1/4}R_g}\sin(Qr)]\frac{e^{-Qr}}{Qr}, \tag{III.9}$$

with $Q_{rs}$ being the numerical factor $Q_{rs} = (5^{1/4}\sqrt{3/2})$. These expression define the total direct correlation function and the potential for a liquid of soft spheres of size $R_g$. It should be stressed that this result is general and does not amount to making the thread limit approximation, but just in assuming $\hat{c}(k)$ to be independent of $k$ for small $k$, where a coarse-grained description is valid. Also, the expression differs slightly from that presented in Chapter II since we have left $r$ in unscaled arbitrary units.

The overall schematic of the coarse-graining procedure is represented by Figure III.1 First, the appropriate monomer-level description is specified, which in the present case is the PRISM thread model. Then, the coarse-grained potential can be calculated. The parameters which enter the potential are the monomer density, $\rho$, the number of monomers per chain, $N$, the temperature, $T$, the effective segment length, $\sigma$, and the direct correlation parameter, $c_0$. We now consider the thermodynamics of the soft-sphere model.

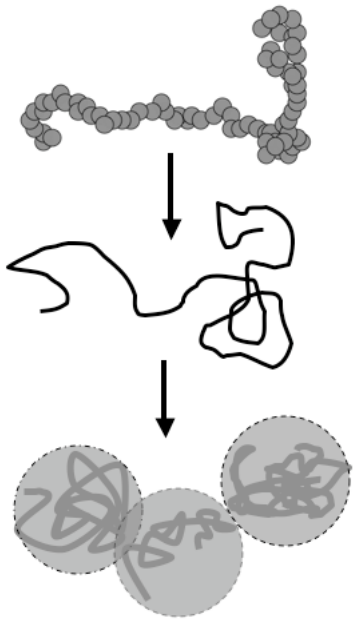

FIGURE III.1. Schematic description of the coarse-graining process. First as an approximate model of the atomistic picture, we represent the actual polymer chain as a Gaussian thread. The parameters from this level of description enter the coarse-graining model, where individual chains are represented as soft colloidal particles, or point particles with a long range, soft effective interaction.

## III.3. Thermodynamics of Soft Interacting Particle Description of a Polymer Melt

The Hamiltonian of a system of $n$ soft particles labeled with index $i \in \{1, n\}$ is simply the sum of the kinetic and potential energy

$$H = \frac{1}{2m} \sum_{i=1}^{n} (p_{xi}^2 + p_{yi}^2 + p_{zi}^2) + \Phi(\mathbf{r}_1, ..., \mathbf{r}_n) \tag{III.10}$$

where $\Phi(\mathbf{r}_1, ..., \mathbf{r}_n)$ is the intermolecular interaction potential. We assume constant temperature, $T$, and constant volume, $V$, conditions, consistent with the canonical ensemble in which the atomistic simulations were performed. The partition function for $n$ particles in a volume $V$ is given as

$$Q = \frac{1}{n! h^{3n}} \int ... \int e^{-\beta H} d\mathbf{p}_1 ... d\mathbf{p}_n d\mathbf{r}_1 ... d\mathbf{r}_n, \tag{III.11}$$

where $h$ is Planck's constant and $\beta = 1/k_B T$. Factoring the molecular partition function into an ideal translational term and a perturbation arising from the intermolecular potential formally gives,

$$Q = \frac{1}{n!} (q_{trans} q_{inter})^n \tag{III.12}$$

with $q_{trans}$ being the classical translational partition function of one atom of a monatomic ideal gas given as

$$\begin{aligned} q_{trans} &= \tfrac{1}{h^3} \int ... \int \exp\left\{ -\tfrac{(p_x^2+p_y^2+p_z^2)}{2k_BTm} \right\} dp_x dp_y dp_z dx dy dz \\ &= V/\Lambda^3, \end{aligned} \tag{III.13}$$

where $\Lambda$ is the thermal deBroglie wavelength. The partition function may be rewritten as

$$Q = \frac{Z_n}{n!\Lambda^{3n}} \tag{III.14}$$

with $Z_n$ the configurational integral given as

$$Z_n = \int ... \int e^{-\Phi(\mathbf{r}_1,...,\mathbf{r}_n)/k_BT} d\mathbf{r}_1 ... d\mathbf{r}_n \tag{III.15}$$

such that

$$q_{inter}^n = \frac{Z_n}{V^n}. \tag{III.16}$$

$q_{inter}$ is the contribution to the single particle partition function that is due to the potential. In the soft sphere representation, the potential is pairwise decomposable,

$$\Phi(\mathbf{r}_1, ..., \mathbf{r}_n) = \sum_{1 \le i \le j}^{n} v^{cc}(r_{ij}), \tag{III.17}$$

and the contribution from the interaction potential, $q_{inter}$, can be written in terms of the mean potential field as

$$\begin{aligned} q_{inter} &= \exp\left(-\bar{\phi}/2k_BT\right) \\ &= \exp\left( -\frac{2\pi\rho_{ch}}{k_BT} \int_0^\infty v^{cc}(r) g^{cc}(r) r^2 dr \right). \end{aligned} \tag{III.18}$$

By combining Equations III.14, III.16, and III.18 with the pair distribution functions and effective potentials of our coarse-grained model we will now derive some thermodynamic functions of interest.

In the canonical ensemble the Helmholtz free energy, $F$, is a natural starting point, given as $F = -k_B T \ln Q$. From Equation III.14 the free energy of a soft sphere can be expressed in terms of the pair potential as

$$F^{\text{soft}} = -nk_B T \ln\left(\frac{Ve}{\Lambda^3 n}\right) + n2\pi\rho_{ch}\int_0^\infty v^{cc}(r)g^{cc}(r)r^2 dr \tag{III.19}$$

where the first term is simply the Helmholtz free energy of an ideal gas, $F_0$, and the second term is a perturbation due to the interaction between point particles through the effective pair potential. For convenience we assume that since the radial distribution function, $g^{cc}(r)$, approaches unity at a much smaller distance than the spatial range of the potential, the integrand is dominated by the contribution arising from the direct correlation function, and $g^{cc}(r)$ is well approximated by the homogenous limit of $g(r) \cong 1$. This assumption is justified by the soft, long-ranged nature of the pair potential. Noting that the integral of the first order correction term vanishes,

$$\int_0^\infty v^{cc}_{(1)}(r)r^2 dr = 0, \tag{III.20}$$

Equation III.19 simplifies to

$$F^{\text{soft}} = F_0 + \frac{n\rho_{ch}}{2}\int_0^\infty v^{cc}_{(0)}(r)4\pi r^2 dr \tag{III.21}$$

which yields the final result,

$$\frac{F - F_0}{nk_BT} = -\frac{Nc_0\rho}{2}. \tag{III.22}$$

It should be noted that the parameters entering the final expression above come entirely from the monomer-level description, (i.e. there are no fit parameters in our procedure). These parameters are simply the chain length, $N$, the monomer site density, $\rho$, and importantly the low wave-vector limit for the monomer direct correlation function $c_0$, which contains important physical information since it is related to the compressibility of the system. This can be seen from the Ornstein-Zernike equation, Equation III.1, using the fact that $\hat{\omega}(0) = N$.

$$\rho k_BT\kappa_T = \frac{N}{1 - \rho N c_0}. \tag{III.23}$$

In principle, Equation III.22 is general and could be applied to any system once the relevant parameters are chosen. In other words, the exact formulation of $c_0$ will depend on the monomer-level model which is used, and will be system specific, i.e. it will depend on the chemical architecture of the chain of interest.

Here, we wish to make the connection to the analytical form of the integral equation theory, and thus we use the PRISM thread result for $c_0$ given by Equation III.3, to obtain the analytical formula

$$\frac{(F - F_0)_{thread}}{nk_BT} = \frac{\pi\rho\sqrt{N}\sigma^3}{6\sqrt{3}} + \frac{\pi^2\rho^2 N\sigma^6}{216}. \tag{III.24}$$

Formally, the total energy of the system of soft spheres is given by

$$\bar{E} = \frac{\int ... \int E e^{-\beta E} d\mathbf{r}_1 ... d\mathbf{r}_n}{Q}, \tag{III.25}$$

which under the assumption of a pairwise potential reduces to the well-know expression for the energy of a classical fluid,

$$E^{soft} = \frac{3}{2} n k_B T + n 2\pi \rho_{ch} \int_0^\infty v^{cc}(r) g^{cc}(r) r^2 dr. \tag{III.26}$$

The integral in Equation III.26 is evaluated under the same approximations used in evaluating Equation III.19, giving the final result,

$$E^{soft} = \frac{3}{2} n k_B T - n k_B T \frac{N c_0 \rho}{2}, \tag{III.27}$$

where $c_0 < 0$. Again, inserting the PRISM thread expression for $c_0$ gives the analytical result,

$$\frac{E^{soft}_{thread}}{n k_B T} = \frac{3}{2} + \frac{\pi \rho \sqrt{N} \sigma^3}{6\sqrt{3}} + \frac{\pi^2 \rho^2 N \sigma^6}{216}. \tag{III.28}$$

The first term in Equation III.28 is simply the kinetic energy of the $n$ classical point particles, whereas the remaining terms are the ensemble average of the potential energy arising from the interaction potential.

The entropy can be calculated from the identity $E = F + TS$. Interestingly, the contribution to the entropy from the interaction potential cancels out, leaving only

the entropy of an ideal gas of point particles,

$$S^{soft} = \frac{3}{2} n k_B + n k_B \ln\left(\frac{Ve}{\Lambda^3 n}\right). \tag{III.29}$$

Equation III.29 may also be obtained directly from the relation $S = k_B T \left(\frac{\partial \ln Q}{\partial T}\right)_{n,V} + k_B \ln Q$ using Equations III.12-III.18. The entropy of the underlying real system has additional contributions arising from chain configurations that are not accounted for in the soft sphere model. This is a consequence of coarse graining and will be discussed further below.

Lastly, the pressure is evaluated using the relation, $P = k_B T \left(\frac{\partial \ln Q}{\partial V}\right)_{n,T}$, which from Equation III.14 is simply

$$P = k_B T \left(\frac{\partial \ln Z_n}{\partial V}\right)_{n,T}. \tag{III.30}$$

Equation III.30 is solved using the standard procedure where the volume limits of the integral in Equation III.15 are removed by a change of variables. Equation III.15 is then substituted into Equation III.30, differentiated with respect to the volume, and upon returning to the original position vectors gives,

$$\frac{P}{k_B T} = \frac{n}{V} - \frac{1}{k_B T Z_n} \int ... \int e^{-\Phi/k_B T} \frac{\partial \Phi}{\partial V} d\mathbf{r}_1 ... \mathbf{r}_n \tag{III.31}$$

which is equivalent to

$$P = \rho_{ch} k_B T - \left\langle \frac{\partial \Phi}{\partial V} \right\rangle \tag{III.32}$$

where $\rho_{ch} = n/V$ is the chain density and

$$\left\langle \frac{\partial \Phi}{\partial V} \right\rangle = \frac{\int ... \int \left(\frac{\partial \Phi}{\partial V}\right) e^{-\Phi/k_B T} d\mathbf{r}_1 ... \mathbf{r}_n}{Z_n}. \tag{III.33}$$

For density-dependent potentials, the volume derivative is often taken to act on the pair potential itself, giving rise to an extra term in the virial equation of state that was pointed out by Ascarelli and Harrison.[67] However, in the case we are considering here, the potential is calculated at a fixed given density, and thus is not a variable of the system.[68]

Equation III.32 recovers the known virial expression for the pressure of a fluid, under the assumption of pairwise additivity,

$$\frac{P}{\rho_{ch} k_B T} = 1 - \frac{2\pi\rho_{ch}}{3k_B T} \int_0^\infty \frac{dv^{cc}(r)}{dr} g^{cc}(r) r^3 dr. \tag{III.34}$$

Again using the approximation $\beta v^{cc}(r) = -c^{cc}(r)$ and $g^{cc}(r) \approx 1$ Equation III.34 can be solved from Equations III.8 and III.9. Noting that the integral of the first order correction term again vanishes,

$$\int_0^\infty \frac{dv^{cc}_{(1)}(r)}{dr} r^3 dr = 0, \tag{III.35}$$

we obtain a simple expression for the equation of state for a fluid of soft spheres,

$$\frac{P}{\rho_{ch} k_B T} = 1 - \frac{N c_0 \rho}{2}. \tag{III.36}$$

In modeling polymers as soft interpenetrating spheres, Louis and co-workers, found that the pressure is described by $\beta P = \rho + 1/2\beta\hat{v}(0)\rho^2$, where $\hat{v}(0)$ is the Fourier transform of the effective potential evaluated at $k = 0$.[69] Their result is consistent with Equation III.36, where our formalism has the advantage of being fully analytical.

Invoking the thread limit of Equation III.3 for $c_0$ gives

$$\frac{P_{thread}}{\rho_{ch} k_B T} = 1 + \frac{\pi\rho\sqrt{N}\sigma^3}{6\sqrt{3}} + \frac{\pi^2\rho^2 N\sigma^6}{216}, \tag{III.37}$$

which takes the form of a familiar virial-type expansion of the density, with the second virial coefficient

$$B_2(T) = \frac{\pi\sigma^3}{6\sqrt{3N}}, \tag{III.38}$$

and the third virial coefficient given by

$$B_3(T) = \frac{\pi^2\sigma^6}{216}. \tag{III.39}$$

**III.3.1.** Higher Order Corrections to the Soft Sphere Equation of State

Equation III.37 is derived under the assumption that the center-of-mass pair potential is $\beta v^{cc}(r) \approx -c^{cc}(r)$. This approximation holds for liquids of long polymer chains, where the center-of-mass of the polymers can easily interpenetrate, $h^{cc}(r) \approx 0$. We now investigate the behavior of the two additional terms in the HNC closure given by Equation I.7, which are the potential of mean force between center of mass sites, defined as $\beta w^{cc}(r) = -\ln[g^{cc}(r)]$, and the total correlation function, $h^{cc}(r)$. We begin again with the pressure equation, Equation III.34, which upon introduction of the potential of mean force (pmf) for $v^{cc}(r)$, reduces to

$$\left(\frac{P}{\rho_{ch} k_B T}\right)_{pmf} = 1 + \frac{2}{3}\pi\rho_{ch}\int_0^\infty \frac{dg(r)}{dr} r^3 dr. \tag{III.40}$$

Equation III.40 can be solved analytically using our coarse-grained expression for $g(r)$ from Equation III.4, with the solution,

$$\left(\frac{P_{thread}}{\rho_{ch}k_BT}\right)_{pmf} = 1 + \pi\rho_{ch}R_g^2\xi_\rho(1+\xi_\rho/\xi_c) \tag{III.41}$$

Introducing the definitions of $\xi_\rho$ and $\xi_c$, and after some algebra, one obtains

$$\left(\frac{P_{thread}}{\rho_{ch}k_BT}\right)_{pmf} = \frac{3}{2} - \frac{1}{(\sqrt{2}+2\pi\rho_{ch}R_g^3)^2}. \tag{III.42}$$

Comparison of Equation III.42 with the equation of state calculated above in Equation III.37, shows that the two are markedly different. Most noticeably, Equation III.42 scales as $\rho^{-2}N^{-1}$, and in the limit of infinitely long or infinitely dense chains, approaches a constant value of 1.5, which is negligibly small compared to Equation III.37 which scales as $\rho^2 N$. This supports the validity of the MSA approximation used above for long chains, where $\beta v^{cc}(r) \to -c^{cc}(r)$. In the opposite limit of infinite chain dilution, $\rho_{ch} \to 0$, both Equation III.37 and Equation III.42 approach unity, recovering the equation of state for an ideal gas.

Factoring out a $1/R_g^2$ and reintroducing the definitions of $\xi_c$ and $\xi_\rho$, Equation III.42 can be equivalently written as

$$\left(\frac{P_{thread}}{\rho_{ch}k_BT}\right)_{pmf} = 1 + \frac{1}{R_g^2}\left(\xi_c^2 - \xi_\rho^2\right). \tag{III.43}$$

Equation III.43 can be directly compared with the *monomer level* description in the PRISM thread limit, for which $g^{mm}(r)$ is given by Equation III.2. Upon differentiation of Equation III.2 with respect to $r$, and insertion into Equation III.40,

one obtains

$$\left(\frac{P_{thread}}{\rho_{ch}k_BT}\right)_{pmf}^{chain} = 1 + \frac{6}{N\sigma^2}\left(\xi_c^2 - \xi_\rho^2\right)$$
$$= 1 + \frac{1}{R_g^2}\left(\xi_c^2 - \xi_\rho^2\right) \qquad \text{(III.44)}$$

which is identical with Equation III.43 obtained in the soft-colloidal representation. Thus the equation of state derived from the potential of mean force is equivalent in both representations. This is important because a common approach in deriving realistic coarse-grained potentials is to use an iterative procedure, such as the Iterative Boltzmann Inversion method, where the coarse-grained distribution function is optimized against the monomer distribution by iterative calculation of the *potential of mean force* until convergence is reached.[31,32] Here we have shown how, for dense polymer systems, thermodynamic quantities derived using the potential of mean force in the coarse-grained and monomer representations are formally identical, but also that they are not accurate, as the full pair potential, $v^{cc}(r)$, is needed in the CG simulation.[9]

The third and final contribution in Equation I.7 to the pressure is again calculated from Equation III.34, and becomes

$$\left(\frac{P}{\rho_{ch}k_BT}\right)_3 = 1 + \frac{2}{3}\pi\rho_{ch}\int_0^\infty g(r)\frac{dg(r)}{dr}r^3dr, \qquad \text{(III.45)}$$

which can be solved analytically using Equation III.4, with the solution,

$$\left(\frac{P_{thread}}{\rho_{ch}k_BT}\right)_3 = 1 - \pi\rho_{ch}R_g^2\xi_\rho(1+\xi_\rho/\xi_c) + \frac{3087}{1024}\sqrt{\frac{\pi}{6}}\rho_{ch}R_g\xi_\rho^2\left(1+\frac{\xi_\rho}{\xi_c}\right)^2. \qquad \text{(III.46)}$$

We are now in position to write the total equation of state from the full HNC

potential as

$$\left(\frac{P}{\rho_{ch}k_BT}\right)_{tot} = \left(\frac{P}{\rho_{ch}k_BT}\right)_{MSA} + \left(\frac{P}{\rho_{ch}k_BT}\right)_{pmf} + \left(\frac{P}{\rho_{ch}k_BT}\right)_{3}. \quad \text{(III.47)}$$

Combining Equation III.36, III.41, and III.45 gives,

$$\left(\frac{P_{thread}}{\rho_{ch}k_BT}\right)_{tot} = 1 + \frac{\pi\rho\sqrt{N}\sigma^3}{6\sqrt{3}} + \frac{\pi^2\rho^2N\sigma^6}{216} + \frac{3087}{1024}\sqrt{\frac{\pi}{6}}\rho_{ch}R_g\xi_\rho^2\left(1+\frac{\xi_\rho}{\xi_c}\right)^2. \quad \text{(III.48)}$$

Not surprisingly, the addition of Equation III.41 and Equation III.46 results in a cancellation of the potential of mean force term.

The additional term in Equation III.48 resulting from the inclusion of the full HNC potential, scales as $\rho^{-1}N^{-1/2}$. Thus, for large $N$ the MSA approximation for which $\beta v^{cc}(r) \approx -c^{cc}(r)$ is increasingly valid and $P^{tot} \approx P^{MSA}$ as given by Equation III.37.

Figure III.2 shows the contributions to the total equation of state from each of the terms in Equation III.47 for a representative case where the monomer density is $\rho = 0.0334$ sites/$\mathring{A}^3$ and effective segment length of $\sigma = 4.06\mathring{A}$. It shows that the equation of state is dominated by the contribution from the MSA approximation term, and the additional contributions rapidly approach their asymptotic value.

### **III.3.2.** The Compressibility Route

An alternative approach to calculate the thermodynamic properties of fluids is to use the compressibility route, which is derived in the grand canonical ensemble, where particle number fluctuations may be readily obtained, and is found to depend solely on density fluctuations. More specifically, the reduced equation of state obtained

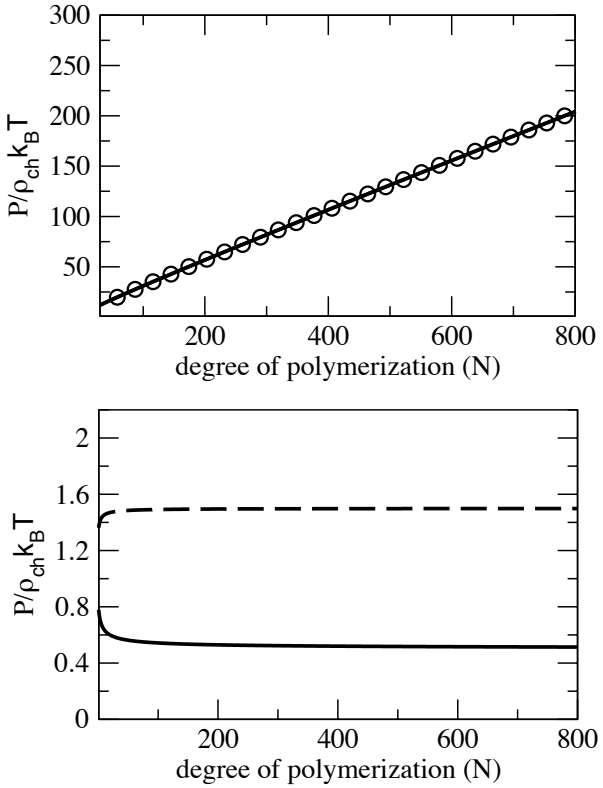


FIGURE III.2. Top: The equation of state obtained from the MSA approximation, Equation III.37 is shown (open circles) in comparison with the full equation of state using the HNC potential, Equation III.48 (solid line) for the PRISM thread model. The two lines superimpose and are nearly indistinguishable, both scaling linearly with $N$ for large N. Bottom: For comparison is show the contributions to the equation of state from Equations III.41 and III.46, both of which quickly approach their asymptotic value with $N^{-1}$ scaling for the potential of mean force term (dashed line) and with $N^{-1/2}$ scaling for the third term (solid line).

from the compressibility route is determined by thermodynamic integration of the isothermal compressibility, $\kappa_T$, which is related to $\hat{S}^{cc}(k \to 0)$, and reads[8]

$$\frac{P}{k_B T} = \int_0^{\rho_{ch}} d\rho [\hat{S}^{cc}(0,\rho)]^{-1}]. \tag{III.49}$$

Using the form of the reciprocal structure factor given above by Equation III.7, recalling that $\Gamma = -Nc_0\rho$, the integral in Equation III.49 can be solved to obtain the compressibility equation of state. A general expression for the density dependence of $c_0$ is not available. As a first estimate, we could ignore any explicitly density dependence of $c_0$ (i.e. $c_0(\rho) = c_0$), giving

$$\left(\frac{P}{\rho_{ch} k_B T}\right)_c = -\frac{N c_0 \rho}{2}, \tag{III.50}$$

which is identical with Equation III.36, showing that the compressibility route and the virial route in this case are equivalent. Also, as shown below, this is equivalent with the monomer-level prediction.

Alternatively, one could introduce a density dependence to $c_0$, for example with the thread limit (Equation III.3), and obtain a slightly different expression. Insertion of Equation III.3 into $[\hat{S}^{cc}(0)]^{-1} = -Nc_0\rho$, and subsequent integration yields,

$$\left(\frac{P_{thread}}{\rho_{ch} k_B T}\right)_c = \frac{\pi\rho\sqrt{N}\sigma^3}{6\sqrt{3}} + \frac{2}{3}\frac{\pi^2\rho^2 N\sigma^6}{216}. \tag{III.51}$$

Comparison of Equation III.51 with Equation III.37 shows that, although not exactly identical, the difference between the two routes in this case is only in the numerical prefactor of the third virial coefficient and not in the overall scaling, which is consistent with the use of the PY closure used to derive the thread limit.

As a test for self-consistency in our theoretical expressions, we can compare the above expression, which was derived from Equation III.7, with that obtained using the analytical expression of the total correlation function, $h^{cc}(k)$, derived from Yatsenko, *et al.*,[38] which can be obtained from integration of Equation III.4, and is given as

$$\hat{h}^{cc}_{thread}(k=0) = -\left[1 - \left(\frac{\xi_\rho}{\xi_c}\right)^2\right]/\rho_{ch}. \tag{III.52}$$

Equation III.52 provides an expression for the isothermal compressibility, $\kappa_T$, related to the structure factor as $\rho_{ch}\kappa_T/\beta = \hat{S}(0) = 1 + \rho_{ch}\hat{h}(0) = (\xi_\rho/\xi_c)^2$. Evaluation of Equation III.49 using our definition for $\hat{h}^{cc}(0)$, one finds

$$\begin{aligned}\left(\frac{P_{thread}}{\rho_{ch}k_BT}\right)_c &= 1 + \sqrt{2}\pi\rho_{ch}R_g^3 + \frac{2}{3}\pi^2\rho_{ch}^2R_g^6 \\ &= 1 + \frac{\pi\rho\sqrt{N}\sigma^3}{6\sqrt{3}} + \frac{2}{3}\frac{\pi^2\rho^2N\sigma^6}{216},\end{aligned} \tag{III.53}$$

where the second expression is obtained using the definition of the effective segment length, $R_g = \sqrt{N/6}\sigma$, and recovers exactly the form of Equation III.51, indicating that the approximate forms for $c^{cc}(r)$ and $[S^{cc}(k)]^{-1}$ are consistent in recovering the compressibility of the coarse-grained system.

Using our coarse-graining procedure for polymer melts, we have now obtained simple, analytical expressions for the reduced equation of state from both the virial route and the compressibility route under different assumptions. Comparison of the reduced equation of state from these different methods show reasonable agreement indicating the consistency of our renormalization procedure and that our analytical form of the direct correlation function and effective pair potential are well determined. We now turn to a more detailed discussion about the equivalence of our expressions with the monomer level description.

## III.4. Equivalence with Monomer Level Description

At this point, we turn to a monomer-level chain description in order to see which of the relationships derived above hold and what information may be lost in coarse-graining. Notationally, the position vector, $\mathbf{r}_i^\alpha$ refers to the position of site $\alpha$ on chain $i$, whereas $\mathbf{r}_{ij}^{\alpha,\gamma}$ is the distance between site $\alpha$ on chain $i$ and site $\gamma$ on chain $j$. Extending the above approach to chain molecules requires the inclusion of intramolecular energy terms such that Equation III.12 becomes

$$Q = \frac{1}{(nN)!}(q_{trans}q_{inter}q_{intra})^{nN} \tag{III.54}$$

where $q_{trans}$ is the translational partition function, $q_{inter}$ is the intermolecular contribution to the partition function and $q_{intra}$ is the intramolecular contribution which will depend on the specific model being used, but will generally include vibrational, angular, torsional, and non-bonded terms. Integration over the $3nN$ independent Cartesian momenta gives,

$$Q = \frac{Z_{nN}}{(nN)!\Lambda^{3nN}} \tag{III.55}$$

where $Z_{nN}$ is the configurational integral given as

$$Z_{nN} = \int ... \int e^{-(\Phi_{inter}+\Phi_{intra})/k_BT} d\mathbf{r}_1^1 ... d\mathbf{r}_n^N, \tag{III.56}$$

where we have separated the potential energy into intermolecular and intramolecular terms.

The energy of the liquid of chains is,

$$E^{chain} = \frac{3}{2} nNk_BT + \langle \Phi_{inter} \rangle + \langle \Phi_{intra} \rangle \,, \tag{III.57}$$

where $\langle \Phi_{inter} \rangle$ is the average intermolecular contribution to the energy and $\langle \Phi_{intra} \rangle$ is the average intramolecular contribution. The first term is given by

$$\langle \Phi_{inter} \rangle = \frac{\int ... \int \Phi_{inter} e^{-(\Phi_{inter}+\Phi_{intra})/k_BT} d\mathbf{r}_1^1 ... d\mathbf{r}_n^N}{Z_{nN}}. \tag{III.58}$$

The true monomer-level description may not be pair-wise additive and higher order correlations will enter between monomers. However, for the sake of simplicity, we assume pair-wise additivity, and thus

$$\Phi_{inter} = \sum_{i>j=1}^{n} \sum_{\alpha,\gamma=1}^{N} v_{\alpha\gamma}(r_{ij}^{(\alpha\gamma)}), \tag{III.59}$$

where $v_{\alpha\gamma}(r_{ij}^{(\alpha\gamma)})$ is the intermolecular pair potential between site $\alpha$ on molecule $i$ and site $\gamma$ on molecule $j$.

The intramolecular contribution is given as

$$\langle \Phi_{intra} \rangle = \frac{\int ... \int \Phi_{intra} e^{-(\Phi_{inter}+\Phi_{intra})/k_BT} d\mathbf{r}_1^1 ... d\mathbf{r}_n^N}{Z_{nN}}. \tag{III.60}$$

The intramolecular potential will depend on the specific monomer chain model, and could include excluded volume, bond, angular, and torsional contributions. In this work, we focus only on the athermal thread limit, which is a highly idealized description for a polymer, for which $\Phi_{intra}$ will only have an excluded volume contribution equivalent to the intermolecular potential. An extension to

more realistic bead-spring models for polymer chains is straightforward and will be presented in a forthcoming paper.

The intramolecular excluded volume potential is written as a sum of pairwise additive terms,

$$\Phi_{intra} = \sum_{i=1}^{n} \sum_{\alpha,\gamma=1}^{N} v_{\alpha,\gamma}(r_{ii}^{(\alpha\gamma)}) \tag{III.61}$$

so that the total energy can be written as

$$E = \frac{3}{2} nNk_BT + \frac{nN\rho}{2} \int_0^\infty 4\pi g(r) v(r) r^2 dr \tag{III.62}$$

where $g(r)$ is the total radial distribution function of monomers.

In the athermal PRISM thread limit, the potential is taken to be a purely repulsive hard core interaction, and the Percus-Yevick (PY) closure is adopted

$$c(r) = (1 - e^{v(r)/k_BT}) g(r) \tag{III.63}$$

which can be approximated by expanding the exponential to first order, such that

$$-k_BTc(r) \approx v(r)g(r). \tag{III.64}$$

Substitution into Equation III.62 immediately gives

$$\frac{E}{nk_BT} = \frac{3}{2}N - \frac{N\rho c_0}{2}, \tag{III.65}$$

which is identical with the result obtained from the course-grained potential except that the kinetic energy is increased by a factor of $N$.

The pressure equation for chain molecules has been rigorously discussed by

Honnell, Hall, and Dickman.[70] Contributions from the intramolecular potential will depend on the particulars of the monomer-level description used. In the thread model, the only intramolecular contribution is the hard core excluded volume interaction, and the pressure is given by

$$\left(\frac{P}{\rho_{ch}k_BT}\right)_{chain} = 1 - \frac{2\pi\rho_{ch}}{3k_BT}\sum_{\alpha,\gamma=1}^{N}\int_0^\infty g_{\alpha\gamma}(r)\frac{dv_{\alpha\gamma}(r)}{dr}r^3dr + R_3, \tag{III.66}$$

where $R_3$ can be written in terms of a three-body distribution function, shown by Schweizer and Curro to be equivalent to[71]

$$R_3 = -\frac{1}{3k_BT}\frac{\rho_{ch}}{N-1}\sum_{\alpha,\gamma,\lambda=1}^{N}\int d\mathbf{r}\int d\mathbf{r}'\hat{\mathbf{r}}\cdot\mathbf{r}'\frac{dv^{mm}(r)}{dr}g^{(3)}_{\alpha\lambda,\gamma}(\mathbf{r},\mathbf{r}'), \tag{III.67}$$

where $g^{(3)}_{\alpha\lambda,\gamma}(\mathbf{r},\mathbf{r}')$ is the joint probability distribution function for site $\alpha$ on chain $i$ and site $\gamma$ on chain $j$ to be separated by distance $\mathbf{r}$ *and* for site $\alpha$ on chain $i$ and site $\lambda$ on the *same* chain $i$ to be separated by distance $\mathbf{r}'$. Schweizer and Curro have shown that the quantity $R_3$ scales as $\rho^{-1}N^{-1/2}$ and is therefore negligible for infinitely long or infinitely dense chains. Here we focus on the first term in Equation III.66. From Equation III.64, along with the thread limit definition of $c(r)$, the derivative of the potential becomes

$$\frac{dv_{\alpha\gamma}(r)}{dr} = -\frac{3v_{\alpha\gamma}(r)}{r} \tag{III.68}$$

Insertion of Equation III.68 into Equation III.66 gives

$$\left(\frac{P}{\rho_{ch}k_BT}\right)_{chain} = 1 + \frac{\rho_{ch}}{2k_BT}\sum_{\alpha,\gamma=1}^{N}\int_0^\infty 4\pi g_{\alpha\gamma}(r)v_{\alpha\gamma}(r)r^2dr. \tag{III.69}$$

Insertion of Equation III.64 along with the PRISM thread $c(r)$ in the site averaged

limit gives the desired result

$$\left(\frac{P}{\rho_{ch}k_BT}\right)_{chain} = 1 - \frac{\rho N c_0}{2}, \tag{III.70}$$

which is precisely equivalent with the result in the course-grained description. This is important as it demonstrates that thermodynamic information is not lost during the coarse-graining procedure, as the bulk properties of a fluid should not depend on the frame of reference used.

### III.4.1. The Compressibility Route

The equivalence between the two levels of description is readily seen in the compressibility route. This is because the formalism inherent in our coarse-graining method is based on determining the center of mass total correlation function, $h^{cc}(r)$, by utilizing the Ornstein-Zernike relationship. In the $k = 0$ limit, both of the intramolecular form factors reduce to $\hat{\omega}(0) = N$, and it is immediately seen that $\hat{h}^{cc}(0) = \hat{h}^{mm}(0)$.

In the monomer frame of reference, the exact recovery of Equation III.53 is arrived at by using the PRISM thread limit for $h^{mm}(k)$,

$$h^{mm}_{thread}(k) = 4\pi\xi'_\rho \left[\frac{\xi^2_\rho}{1 + k^2\xi^2_\rho} - \frac{\xi^2_c}{1 + k^2\xi^2_c}\right], \tag{III.71}$$

with the quantity, $\xi'_\rho = 1/(2\pi\rho_{ch}R^2_g)$. Taking the $k = 0$ limit of Equation III.71, one recovers Equation III.52 in the monomer frame of reference. At the monomer level, $\hat{S}^{mm}(0) = \hat{\omega}(0) + \rho h^{mm}(0) = N(\xi_\rho/\xi_c)^2$, and the integration is carried out over the

monomer density of sites,

$$\left(\frac{P}{k_BT}\right)_{chain} = \int_0^\rho d\rho[\hat{S}^{mm}(0,\rho)]^{-1}]$$
$$= \rho_{ch} + \sqrt{2}\pi\rho_{ch}^2 R_g^3 + \frac{2}{3}\pi^2\rho_{ch}^3 R_g^6, \tag{III.72}$$

which is equivalent to Equation III.53 upon division by $\rho_{ch}$.

The free energy can be readily computed via the standard thermodynamic integration of the pressure,[72]

$$\frac{F}{nk_BT} = \int_0^\rho \frac{d\rho'}{\rho'}\frac{NP}{\rho' k_BT} \tag{III.73}$$

Substitution of Equation III.72 into Equation III.73 and subsequent integration gives

$$\frac{(F-F_0)_{thread}}{nk_BT} = \frac{\pi\rho\sqrt{N}\sigma^3}{6\sqrt{3}} + \frac{1}{3}\frac{\pi^2\rho^2 N\sigma^6}{216} \tag{III.74}$$

where we have used $\sigma = \sqrt{6/N}R_g$. Both Equation III.72 and Equation III.74 have been derived elsewhere by Chatterjee and Schweizer for a homopolymer fluid.[73] Comparison of Equation III.74 with our result for the course grained model given by Equation III.24 show that the two are nearly equivalent with a slightly different prefactor in the final term which comes from the difference between the compressibility and virial route expressions.

## III.5. Comparison of Analytical Expressions with Molecular Dynamics Simulations of Soft Spheres

Our coarse-graining procedure enables one to perform molecular dynamics simulations of large ensembles of polymers, each represented by a single center of mass

site interacting with other sites through an effective potential. These simulations are designated as mesoscale (MS) simulations as they provide information about intermediate time and length scales. Having derived various analytical formulas for thermodynamic properties of interest, our goal in this section is to demonstrate the consistancy between these theoretical expressions and mesoscale simulations.

Any coarse-graining scheme is only as accurate as the more detailed molecular model from which it is derived. Since we have shown that our expressions recover the known PRISM result when the PRISM thread expression for $c_0$ is used, this can be seen as a self-consistency check between thermodynamic quantities calculated directly from MS simulation and from theory.

The procedure to obtain the pair potential is as follows: First, Equation II.14 is used to obtain $h^{cc}(k)$. For the monomer intramolecular distribution we use the Debye formula

$$\omega^{mm}(k) = \frac{2N(e^{-k^2R_g^2} + k^2R_g^2 - 1)}{k^4R_g^4}, \tag{III.75}$$

whereas for the distribution of monomers about the center of mass we employ the Gaussian form,

$$\omega^{cm}(k) = Ne^{-k^2R_g^2/6}. \tag{III.76}$$

For $h^{mm}(k)$ we use the Ornstein-Zernike equation, given by Equation III.1, with $c^{mm}(k)$ approximated as $c_0$ given by the thread limit result of Equation III.3 . From $h^{cc}(k)$, we obtain $c^{cc}(k)$ from Equation III.5. Numerical Fourier Transform of both $h^{cc}(k)$ and $c^{cc}(k)$ yields the desired potential, $v^{cc}(r)$ through the HNC closure given by Equation I.7.

The only parameters entering the model are $\sigma$, $\rho$, $T$, and $N$. To test our expressions we perform mesoscale simulations for two different sets of chain lengths

with differing monomer densities. The first set with $N = 100$, $T = 450K$, and an effective segment length of $\sigma = 4.08\mathring{A}$. The second set with $N = 500$, $T = 450K$, and $\sigma = 4.415\mathring{A}$

Mesoscale simulations of point particles interacting through the soft effective potential have beendescribed elsewhere.[64,74] Briefly, the simulations are performed using the LAMMPS code[75] in parallel using the SDSC Trestles cluster available through XSEDE. Simulations were run in the $NVT$ ensemble, using a Nose-Hoover thermostat with periodic boundary conditions. The pressure in the mesoscale simulation is calculated using the standard virial relation

$$P = \frac{nk_BT}{V} + \frac{\sum_i^n r_i \cdot f_i}{3V}. \tag{III.77}$$

The average total, kinetic, and potential energy was also calculated from the simulation.

The number of particles included in a simulation is chosen to maintain the density of chains in the atomistic description; hence $\rho_{ch} = \rho/N$. Since the volume must increase with the range of the potential, it is convenient to cut the potential at some distance, $r_{cut}$, after which the particles do not interact. However, cutting the potential introduces effects on the calculated thermodynamic quantities. The soft potential has the general form of a damped oscillating function. For the $N = 100$ set of simulations we chose to cut the potential where the derivative passes through zero to avoid any discontinuities in the force. The top panel of Figure III.3 shows the potential for a representative density ($\rho = 0.78$ g/mL). The potential was cut where the derivative (shown on the right) passes through zero, which were for this density at $r_{cut} = 104\mathring{A}$, $194\mathring{A}$, and $270\mathring{A}$. The bottom panels of Figure III.3 show the calculated thermodynamic quantities as compared to our analytical expressions for

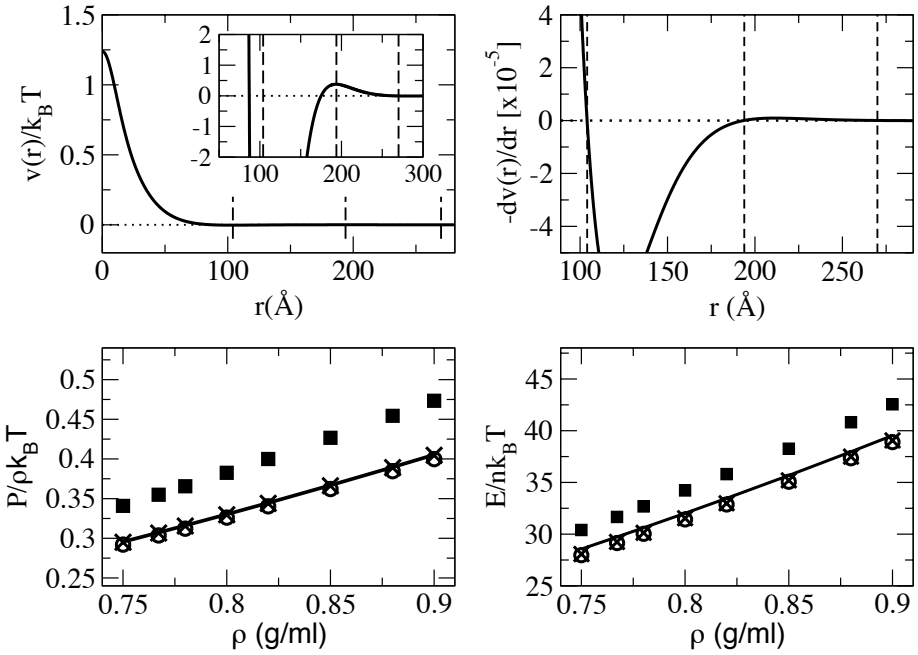


FIGURE III.3. The soft potential (Top Left) calculated for the representative case for PE with $N = 100$ and $\rho = 0.78$ g/mL. The dashed lines indicate the distances at which the potential was cut, which occur where the force crosses zero (Top right). The inset highlights the region where the potential is cut. The bottom panels show the pressure (Bottom Left) and potential energy (Bottom right) calculated directly from mesoscale simulations of point particles cut after the first repulsive peak (squares), the first repulsive plus first attractive well (open circles) and after the first repulsive, first attractive, and second repulsive peak (crosses). Comparison is made with our analytical prediction given by Equation III.37 and Equation III.28 (solid line) for different densities.

the thread model. Cutting the potential after just the first repulsive part leads to an overestimate of the pressure and energy, whereas including the small attractive tail nearly completely corrects for this. The agreement is quantitative when the second repulsive barrier is included.

Figures III.4 and III.5 show a comparison between the pressure and potential energies (respectively) as predicted from our analytical formula and those calculated

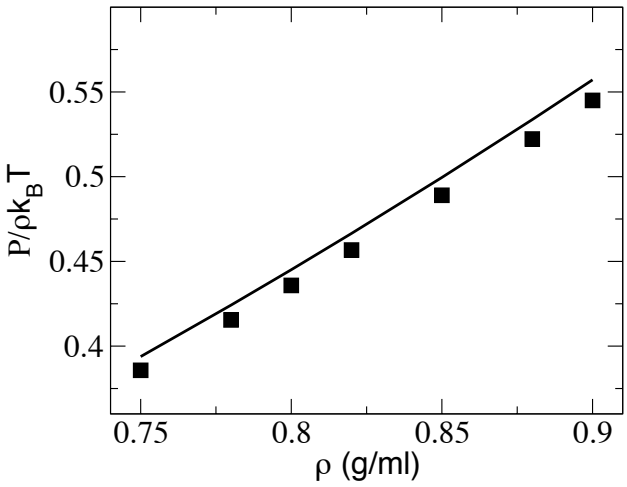


FIGURE III.4. Comparison between the pressure calculated directly from mesoscale simulations of point particles (squares) with analytical prediction given by Equation III.37 (line) for different densities of PE with $N = 500$.

directly from the simulation. For the set of simulations with $N = 500$ we show only the results where the potential was cut after the first repulsive plus first attractive well in the force. Results show quantitative agreement between theory at the monomer and CG levels of description, as well as consistency with data from mesoscale simulations, indicating that the thermodynamics for our soft sphere model are well understood.

## III.6. Conclusion

This chapter has presented a detailed study of the structural and thermodynamic properties of our coarse-grained soft-sphere model, and has made direct comparison to mesoscale simulations that use the derived effective potential as an input. As an illustrative example, we considered the PRISM thread model as the underlying

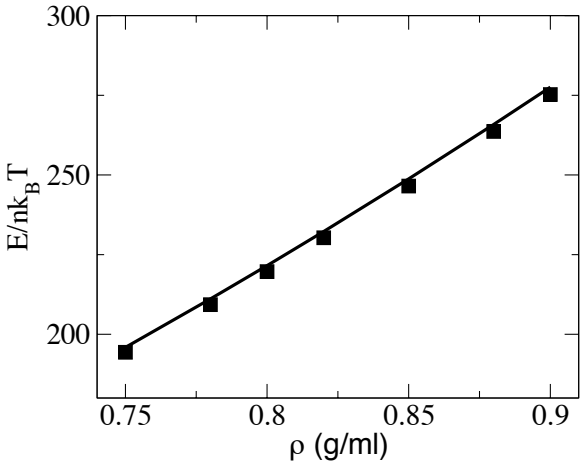


FIGURE III.5. Comparison between the potential energy calculated directly from the average of the mesoscale simulation (squares) with the analytical prediction given by Equation III.28 (line) for PE with $N = 500$

atomistic description which provides an analytical solution. Atomistic and CG descriptions, as well as mesoscale simulations are shown to be fully consistent, demonstrating that the described CG procedure formally maintains both structural and thermodynamic properties of the system under study during coarse-graining. In the next Chapter, we consider a more realistic underlying model of a polymer chain instead of the thread model. In this case, the PRISM Ornstein Zernike equation must be solved numerically for the monomer direct correlation function.

# CHAPTER IV

# ACCURATE DETERMINATION OF THE THERMODYNAMIC PROPERTIES OF POLYETHYLENE MELTS FROM HIGHLY COARSE-GRAINED SIMULATIONS: COMPARISON WITH REALISTIC MOLECULAR DYNAMICS SIMULATIONS

Chapters IV and Chapters V deal with a numerical implementation of the coarse-graining procedure at multiple block levels. This is important because most realistic polymers cannot be described quantitatively with the Gaussian thread model. Instead, the numerical PRISM equations are solved to obtain the monomer direct correlation parameter, $c_0$, which is then used as a parameter in the coarse grained model. Chapter IV discusses the thermodynamics of coarse-graining at the multi-block level, and presents a detailed comparison of the equation of state, free energy, structural correlation functions, and potential energies between different levels of representation for polyethylene melts. Comparison is also made with united atom (UA) simulations of the same chains. These simulations are difficult to equilibrate and were performed on the SDSC Trestles supercomputer available through the XSEDE project funded by NSF.

A manuscript of this chapter is being prepared for publication with co-authors A. Clark, J. Copperman, and M. Guenza. All three co-authors have contributed useful discussions and help in getting the manuscript ready for publication.

## IV.1. Introduction

A major limitation in coarse-graining, which has delayed the widespread use of such models in engineering and material science is the lack of thermodynamic

consistency between various representations. For many numerical coarse-graining schemes, there is no guarantee that the resulting behavior of the coarse system will be consistent with what would have been observed by using a more detailed, more-expensive, model.[57,60,61] Much of the difficulty in developing consistent coarse-graining approaches stems from the fact that it is not always clear how various many-body effects are incorporated into simple two-body interactions, and how errors in the numerical optimization of a pair potential are propagated to thermodynamic properties.

In a multiscale procedure, one seeks to link simulations at different levels of description into on "unified" description of the liquid at all length scales. This requires understanding in a well-defined and clear way how to represent a molecule into coarser and coarser units successively, and then to reintroduce the finer structure of the liquid "a posteriori" in a reverse mapping procedure.

This chapter focuses on a numerical implementation of our coarse-graining procedure, which is based on statistical mechanical principles (i.e. the Ornstein-Zernike equation and liquid state theory). Chapter III demonstrated in detail that the thermodynamics are consistent with polymer integral equation theory, where the PRISM thread model was used to parameterize the atomistic model. In this chapter we wish to implement the procedure to demonstrate the versatility of the approach to model realistic polymer chains. In this case, we consider linear chains of polyethylene melts at various chain lengths and various densities where we represent the chains at different level of chemical detail. The coarse-graining procedure is general and applicable to a wide number of interesting systems.

## IV.2. Molecular Dynamics Simulations

Throughout this chapter we consider a melt of linear polyethylene on two levels of molecular detail. The more detailed level of description considered will be the united atom (UA) model, where each $CH_x$ group is represented as a single interaction site.[25] This model has been used extensively to represent hydrocarbons of different chemical specificity.[26–28] Our CG model is a more extreme representation where we represent the same system as a collection of soft spheres, where each sphere represents a large segment of the polymer chain. We call simulations performed at these various multi-block levels of description Mesoscale (MS) simulations, since they represent the system at a level of description in between an all-atom and a continuum level. As a limiting case, we represent the whole chain with a single, soft interaction site, the soft-sphere model. For this level of coarse-grainging, the relevant information is on length-scales larger than a single polymer chain. Having a description that systematically represents the chain at several levels of detail, enables us to connect information in a multi-scale procedure. A series of snapshots are shown in Figure IV.1, where a single polymer chain is represented first by several spheres, then by a single soft sphere, allowing for the simulation of many more polymers than would otherwise be possible to simulate. The soft particles interact via the coarse-grained potential described below.

UA simulations use the TRAPPE forcefield parameters[26] specified in Table 1. Non-bonded interactions between sites separated by more than 4 sites away are

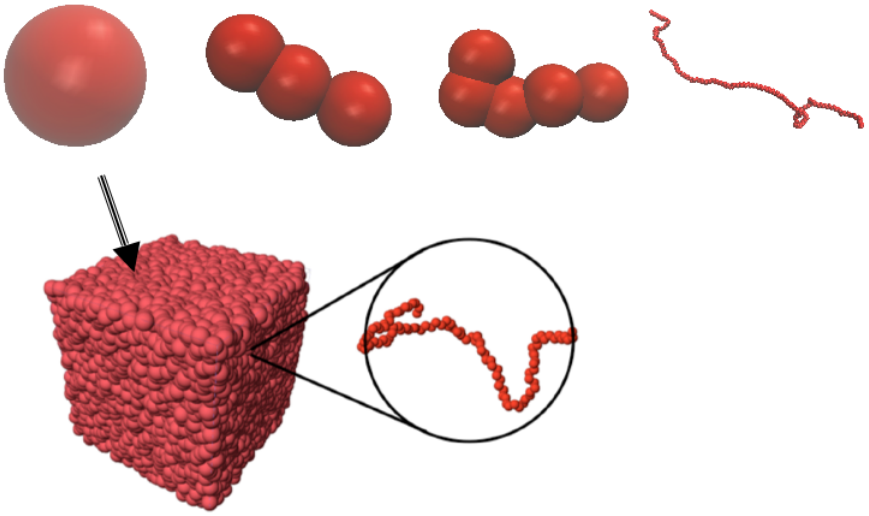

FIGURE IV.1. Coarse-graining at multiple block-levels. The far right is a snapshot of a typical configuration from UA a simulation of polyethylene. Moving from right to left the same chain is represented by 5 blocks, 3 blocks, to a single soft sphere. Below is a snapshot of a typical mesoscale simulations, where each sphere represents a single polyethylene chain.

TABLE IV.1. Polyolefin Melt Simulation Parameters

| | | | |
|---|---|---|---|
| Lennard-Jones | $\epsilon$ (kcal/mol) | $\sigma$ ($\mathring{A}$) | |
| | 0.0912 | 3.95 | |
| Bond parameters | $l_0$ ($\mathring{A}$) | $k_{bond}$ (kcal/mol $\mathring{A}^2$) | |
| | 1.54 | 900 | |
| Angle parameters | $\theta_0$ (degrees) | $k_{angle}$ (kcal/mol rad$^2$) | |
| | 114.0 | 123.75 | |
| Dihedral parameters | $k_1$ (kcal/mol) | $k_2$ (kcal/mol) | $k_3$ (kcal/mol) |
| | 1.4110 | -0.27084 | 3.143 |

governed by the Lennard-Jones potential,

$$v_{nb}(r) = 4\epsilon \left[ \left(\frac{r}{\sigma}\right)^{12} - \left(\frac{r}{\sigma}\right)^{6} \right]. \tag{IV.1}$$

Adjacent intramolecular sites interact through a harmonic potential

$$v_{bond}(r) = \frac{k}{2}(l - l_0)^2 \tag{IV.2}$$

where $l$ is the bond length. Angle interactions between triplets of intramolecular sites are governed by a harmonic potential of the form

$$v_{angle}(\theta) = \frac{k}{2}(\theta - \theta_0)^2. \tag{IV.3}$$

Finally, dihedral interactions between quadruplets of atoms is governed by the OPLS dihedral potential[76]

$$v_{dih}(\phi) = \frac{1}{2}k_1[1 + \cos(\phi)] + \frac{1}{2}k_2[1 - \cos(2\phi)] + \frac{1}{2}k_3[1 + \cos(3\phi)] \tag{IV.4}$$

Simulations are performed using the LAMMPS molecular dynamics code.[75] Chains were randomly generated, and overlapping chains in the initial configuration were slowly pushed apart by a soft repulsive potential for 1ns of simulation time. Then, the full non-bonded potential was switched on with a small timestep, and the system was run for an additional 1ns while ramping up the timestep to 1.25 fs. Subsequently, chains were allowed to equilibrate for 10ns before a final production run of 11ns was used to collect trajectories and calculated static properties. Simulations were run in parallel using the SDSC Trestles clusters available through XSEDE. All simulations were run in the NVT ensemble using Nose Hoover thermostat. We ran

two sets of simulations: the first set at $T = 400K$ with a variety of densities and chain lengths. The second set was at $T = 509K$ at a fixed density of $\rho = 0.03153$ sites/$\mathring{A}^3$ and a variety of chain lengths.

Mesoscale simulations of point particles allow for the simulation of many more particles than the atomistic simulations. The increased particle number makes these simulations suitable to study bulk, large-scale properties such as shearing or phase transitions. The soft particles interact via the coarse-grained potential described in previous chapters. An initial configuration of particles were generated on a cubic lattice, and classical molecular dynamics simulations were again performed using the LAMMPS MD code. Due to the soft nature of the pair potential, mesoscale simulations rapidly equilibrate which is a further advantage to UA simulations of the same system. Simulations were run in the NVT ensemble to reproduce the conditions of the United Atom simulations. For the multi-block model, a coarse-grained bond potential, $v_{\text{bond}}(r)$, and angle potential, $v_{\text{angle}}(\theta)$, were implemented by direct Boltzmann inversion of the probability distributions predicted for Gaussian chains,

$$\begin{aligned} v_{\text{bond}}(r) &= -k_B T \ln\left[P(r)/r^2\right] \\ v_{\text{angle}}(\theta) &= -k_B T \ln\left[P(\theta)/sin(\theta)\right] \end{aligned} \tag{IV.5}$$

The explicit form of these potentials in presented in Chapter V. It is shown in this chapter that these potentials reproduce the predicted angular and bond distributions calculated from united atom simulations.

## IV.3. Thermodynamic Properties

### IV.3.1. Equation of State

In this section we present results of the equation of state calculated by performing numerous mesoscale and UA simulations. The key result of this work is that all MS simulations are thermodynamically consistent in that the pressure and compressibility is consistent across multiple levels of description. In other words, the multi-scale scheme is self-consistent across multiple block levels of description and once the parameters are correctly chosen reproduce the correct equation of state as those predicted from UA simulations. A discussion of how these parameters enter the model and how they are determined is presented in Chapter V

We perform numerous simulations of both soft-sphere and UA models under the same set of conditions. The pressure is calculated from each simulation using the standard viral expression

$$P = \frac{nk_BT}{V} + \frac{\sum_i^n r_i \cdot f_i}{3V}. \tag{IV.6}$$

Figures IV.2 and IV.3 show the pressure from polyethylene simulations performed at $T = 400K$ for a variety of chain lengths and densities. In all cases the coarse-grained simulations reproduce quantitatively the equation of state without any post-optimization scheme or fitting procedure. We also consider a set of simulations of increasing chain length performed at a constant monomer density of $\rho = 0.733g/ml$ and temperature, $T = 509K$. As united atom simulations of long chains are difficult to equilibrate, a reasonable starting configuration for these simulations were provided

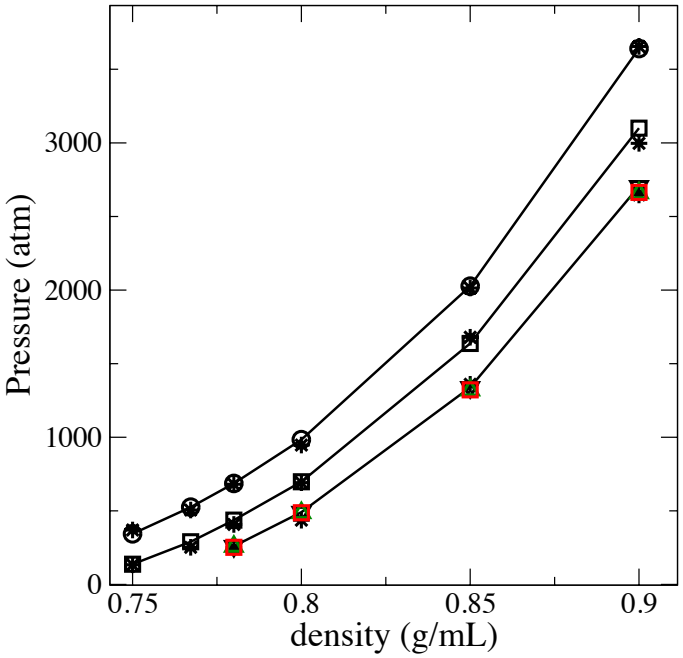


FIGURE IV.2. Comparison of the pressure from united atom simulations of PE $N = 44$ (black circles), PE $N = 78$ (squares) and PE $N = 200$ ( black triangle) with coarse-grained simulations of the soft sphere model (stars) and tri-block model (green triangles) and 5-block model (red squares).

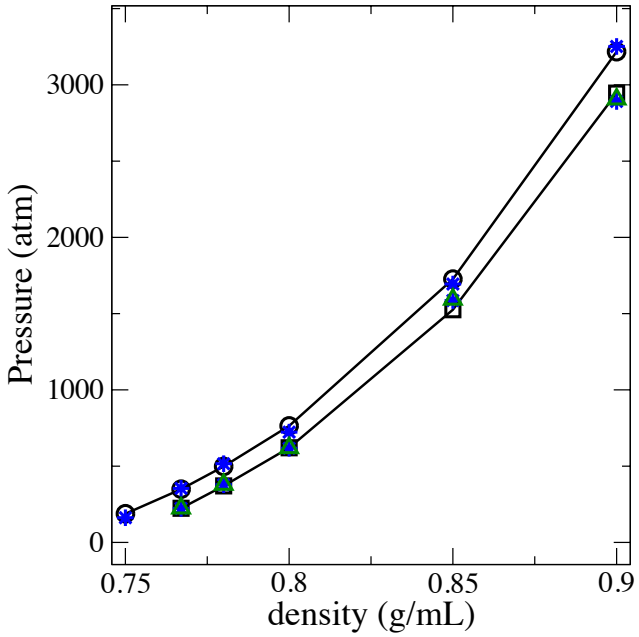


FIGURE IV.3. Comparison of the pressure from united atom simulations of PE $N = 66$ (black circles), PE $N = 100$ (black squares) with coarse-grained simulations at the soft sphere level (stars) and 3-block level for PE100 (green triangles).

to us by Mavrantzas and coworkers.[77,78] Comparison of theses simulations with various levels of coarse-graining are presented in Figure IV.4.

Having an analytical approximation of the effective potential, we have shown in Chapter III that the equation of state is

$$\frac{P}{\rho_{ch} k_B T} = 1 - \frac{N c_0 \rho}{2}, \tag{IV.7}$$

where $\rho$ is the site number density, $N$ is the number of monomers per chain, $\rho_{ch}$ is the density of chains, and $c_0$ is the direct correlation function at zero wave vector, $\hat{c}(k = 0)$, defined from liquid state theory and discussed further below. This equation of state holds for any level of blob description.[62] All of the non-ideal contributions to the pressure that arise from highly system-specific interactions are contained in this single parameter, $c_0$. As a result, the general expression of equation IV.7 is independent of the model used, but evaluation of other thermodynamic properties from the pressure requires knowledge of the state dependence of $c_0$ for the given system of interest. Previously, we used the PRISM thread model as an informative limiting case, which predicts a linear dependence of $c_0$ on the monomer density, giving the equation of state as,

$$\frac{P_{thread}}{\rho_{ch} k_B T} = 1 + \frac{\pi \rho \sqrt{N} \sigma^3}{6\sqrt{6}} + \frac{\pi^2 \rho^2 N \sigma^6}{216}. \tag{IV.8}$$

However, from numerical calculations presented below, it is evident that the density dependence of $c_0$ is not linear for higher densities, and the analytical result grossly underestimates the pressure for high density systems where excluded volume effects not included in the thread model dominate the pressure. In this work, we seek a convenient expression for $c_0$ that will allow for the calculation of other

thermodynamic properties, which can then be tested by comparison to simulation results. When introduced into Equation IV.7, this will provide an expression for the equation of state for the polymer chain.

In simple liquids, the compressibility factor ($P/\rho k_B T$) is often plotted against the packing fraction, $\eta = \pi d^3 \rho/6$, where $d$ is the hard sphere diameter. Although real polyethylene chains are not simple hard sphere fluids, a similar analysis can be made by defining an effective packing fraction $\eta_e = \pi d_e^3 \rho/6$ where $d_e$ is an "effective" hard sphere diameter and $\rho$ is the monomer density. The effective hard sphere diameter will be smaller than the real hard sphere diameter because of the overlaps between intramolecular sites, which decreases the amount of space occupied by the molecules [ie. I can fit more monomers in an equivalent volume than hard spheres]. We assume that for polymer chains, the direct correlation function can then be written as a power series in the effective packing fraction,

$$c_0 = -\frac{4\pi}{3} d^3 \left(1 + \alpha\eta_e + \beta\eta_e^2 + \gamma\eta_e^3 + ...\right). \tag{IV.9}$$

Substitution into Equation IV.7 gives

$$\frac{P}{\rho_{ch} k_B T} = 1 + 4N\eta_e \left(1 + \alpha\eta_e + \beta\eta_e^2 + \gamma\eta_e^3 + ...\right). \tag{IV.10}$$

Following the intuition that for a simple hard sphere fluid, the series can be written as a linear combination of only the first and second derivatives of a geometric seres, we factor out a polynomial, $f(\eta)$, such that the remaining terms are given by the binomial coefficients of the form,

$$\frac{P}{\rho_{ch} k_B T} = 1 + 4N\eta_e f(\eta_e) \sum_{n=0}^{\infty} \frac{(n+2)!}{n!2!} \eta_e^n, \tag{IV.11}$$

which can be summed to give,

$$\frac{P}{\rho_{ch} k_B T} = 1 + \frac{4N\eta_e f(\eta_e)}{(1-\eta_e)^3}. \tag{IV.12}$$

Next, we assume $f(\eta_e)$ to be a quadratic polynomial in terms of $\eta$, such that $[f(\eta_e) = 1 + c1\eta_e + c2\eta_e^2]$, giving the final result for the equation of state for the polymer,

$$\frac{P}{\rho_{ch} k_B T} = \frac{1 + (4N-3)\eta_e + (4Nc_1 + 3)\eta_e^2 + (4Nc_2 - 1)\eta_e^3}{(1-\eta_e)^3} \tag{IV.13}$$

and the direct correlation function,

$$c_0 = -\frac{4\pi d^3}{3} \frac{1 + c_1\eta_e + c_2\eta_e^2}{(1-\eta_e)^3}. \tag{IV.14}$$

Equation IV.13 has the form of a Carnahan Starling-type expression, but with numerical pre-factors in front which reflect the chain connectivity and the fact that the real potential is not a hard sphere potential. For large N, the equation of state can be approximated as,

$$\frac{P}{\rho k_B T} \approx \frac{4\left(\eta + c_1\eta^2 + c_2\eta^3\right)}{(1-\eta)^3}. \tag{IV.15}$$

Assuming that $c1$ and $c2$ are independent of $N$, a plot of the pressure against the effective packing fraction should yield a universal pressure curve for all polyethylene chains. This plot is shown in Figure IV.5 where we show the pressure calculated from united atom simulations against the effective packing fraction. The points nearly fall onto a universal curve of the form of Equation IV.15. A fit of all the data yields the empirical values of $c1 = -11.9045$ and $c2 = 31.1144$, which are independent of both temperature and degree of polymerization. Using Equation IV.14 we can estimate

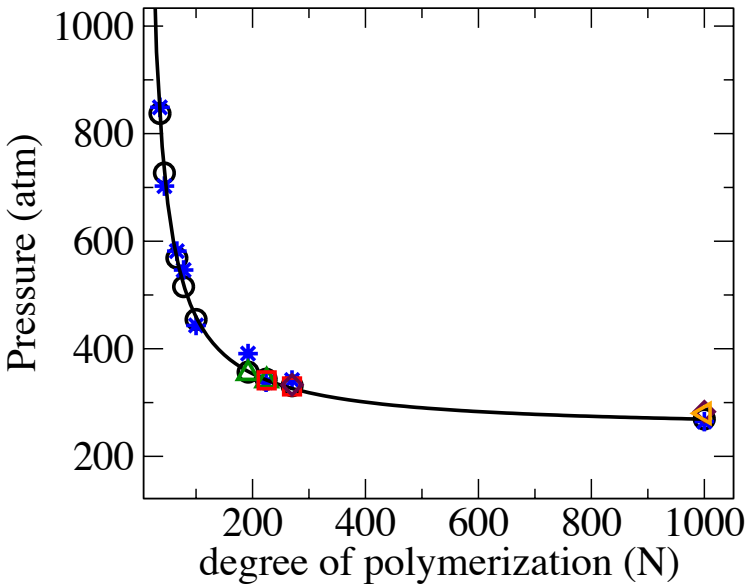


FIGURE IV.4. Pressure vs. degree of polymerization calculated for a hierarchy of soft-block simulations as compared to united atom simulations. All simulations were carried out at constant temperature, T=509K, and density, $\rho = 0.733$ g/mL. United atom model is depicted with black circles, soft sphere model with blue asterisk, tri-block with green triangles, 5-block with red squares, 10-block with maroon diamonds, and 20-block with orange left-oriented triangle.

$c_0$ for any chain length at any temperature for polyethylene.

### IV.3.2. Free Energy Estimation

Having a form of the equation of state allows for an expression of the Helmholtz free energy to be obtained by integration

$$\frac{\Delta F}{nk_BT} = \int_{\eta_1}^{\eta_2} \left( \frac{P}{\rho_{ch} k_B T} \right) \frac{d\eta'}{\eta'}. \tag{IV.16}$$

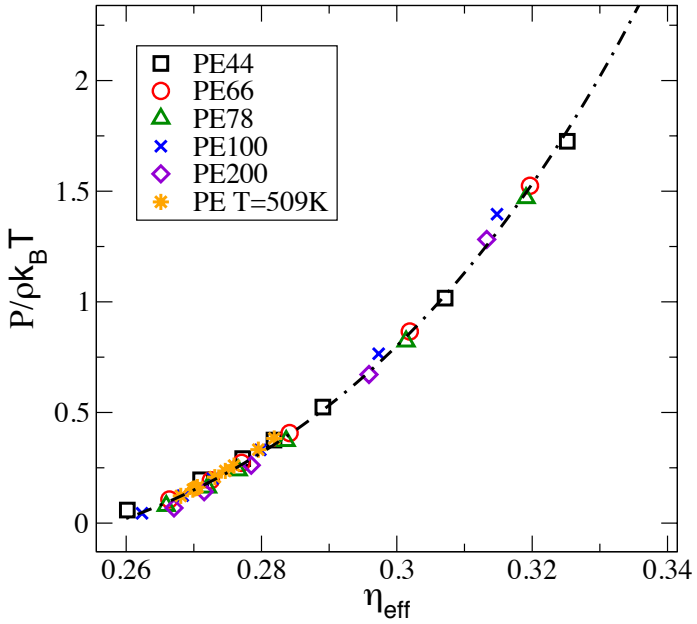


FIGURE IV.5. Pressure data from United Atom simulations plotted as function of the effective packing fraction.

Substitution of Equation IV.13 into Equation IV.17 gives an expression for the free energy change associated with a change in packing fraction from $\eta_1 \rightarrow \eta_2$

$$\frac{\Delta F}{Nnk_BT} = \frac{2(1-c_1-3c_2)(\eta_1^2-\eta_2^2)+4(1-c_2)(\eta_2-\eta_1)-4(c_1+2c_2)(\eta_1\eta_2^2-\eta_1^2\eta_2)}{(1-\eta_1)^2(1-\eta_2)^2} + \ln\left[\left(\frac{1-\eta_1}{1-\eta_2}\right)^{4c_2}\left(\frac{\eta_2}{\eta_1}\right)^{1/N}\right] \tag{IV.17}$$

Taking the limit as $\eta_1 \rightarrow 0$ gives a closed expression for the excess free energy associated with the liquid as distinct from an ideal gas

$$\frac{\Delta F^{ex}}{Nnk_BT} = \frac{-2(1-c_1-3c_2)\eta_2^2+4(1-c_2)\eta_2}{(1-\eta_2)^2} - 4c_2\ln[(1-\eta_2)] \tag{IV.18}$$

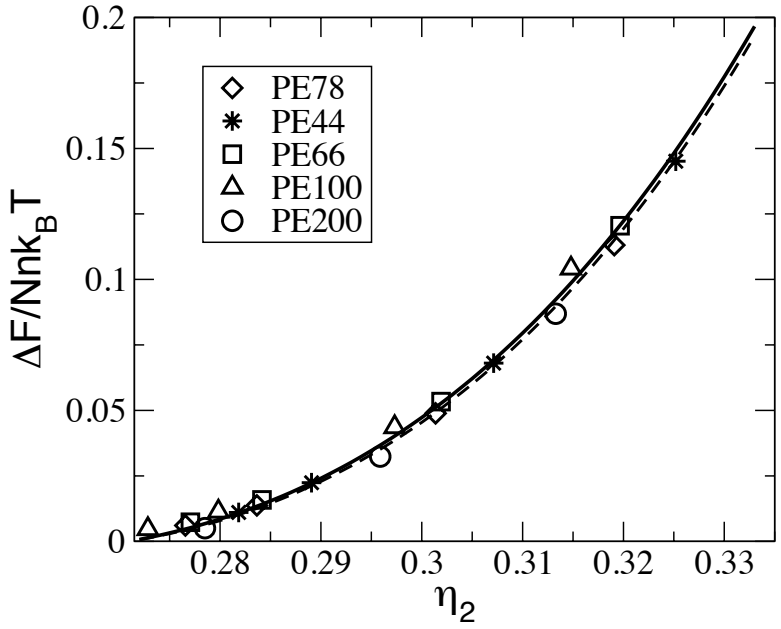


FIGURE IV.6. Estimated free energy change obtained via thermodynamic integration of the pressure, as a function of packing fraction compared to a reference packing fraction of $\eta_1 = 0.27$. All systems collapse to a universal curve within numerical precision, independent of degree of polymerization. The solid and dashed lines represent equation IV.17 evaluated at N=44 and 200 respectively.

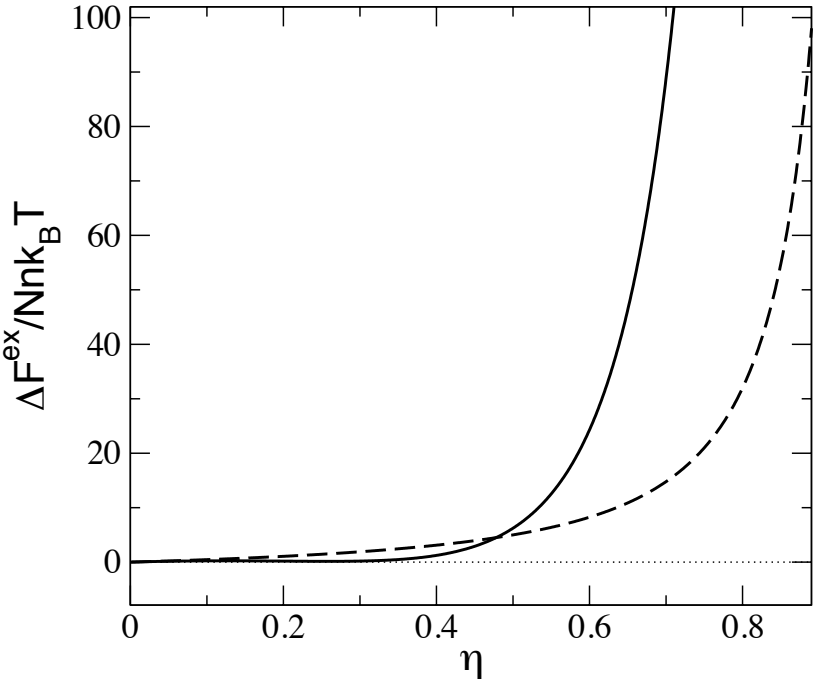


FIGURE IV.7. Excess free energy given by Equation IV.18 as a function of packing fraction. For comparison, the dashed line depicts the excess free energy for a simple liquid of hard spheres.

In the hight density limit, in which we are interested, every particle interacts with a large number of surrounding molecules. Since the potential is long ranged and bounded without short range excluded volume interactions, the free energy in the canonical ensemble is calculated from the mean field approximation,[79,80]

$$F_{exe} = \frac{n\rho_{ch}}{2} \int v^{bb}(r) g^{bb}(r) d\mathbf{r} \tag{IV.19}$$

$$\begin{aligned} \frac{F_{exe}}{n_{ch} k_B T} &= -\frac{\rho c^{bb}(k=0)}{2N_b} \\ &= -\frac{\rho n_b N_b c_0}{2} \end{aligned} \tag{IV.20}$$

which is independent of the level of coarse-graining as $n_b N_b = N$, the number of monomers per chain. Equation IV.20 and Equation IV.18 are different because of the density dependence of the potential and $c_0$. Equation IV.18 is derived by integration over the density, thus the density dependence of $c_0$ had to be accounted for. Equation IV.19 was calculated in the canonical ensemble where the density is constant, and thus the potential is not changing. The main point here is that the excess free energy does not depend on the level of coarse-graining, and is a constant, which is consistent with Figure IV.6 and with the fact that the computed pressure is independent of the level of coarse graining.

### IV.3.3. Structure

The particles in the CG model correspond to fictitious center of mass sites of the underlying real chain, either at the single soft sphere level, or at the mutiblock level. In other words, many atoms in the underlying detailed description are "mapped" onto a single site in the CG representation. Thus, the structure of the CG model reproduces the structure of the detailed model only on the level of the mapping. Thus, we say the structures are equivalent if the distribution functions are equivalent at that level of description and larger. Many atomistic configurations could have the same center of mass configuration, and a CG procedure is unable to distinguish between these "finer" levels of detail. This leads to a reduction in the dimensionality of the configuration space which is also associated with a smoothing of the probability distributions which have a consequence for the entropy of the system, which will be discussed below. Here we are interested in comparing the configuration distributions between coarse-grained and united atom simulations in the configuration space of the coarse-grained model. Figure IV.8 shows a depiction of a random-walk chain mapped onto a tri-block chain with three interaction sites located at the center of mass of a group of monomers. The bond vector linking coarse-grained sites is given as $\mathbf{R}$ and the angle, $\theta$, defines the angle between two bond vectors, $\mathbf{R}_1$ and $\mathbf{R}_2$. As a representative case, we map a polyethylene chain with $N = 225$ monomers onto a 3-block model, each block with 75 underlying monomers. Figure IV.9 shows the distribution of the bond vector and angle vector from both coarse-grained and united atom simulations.

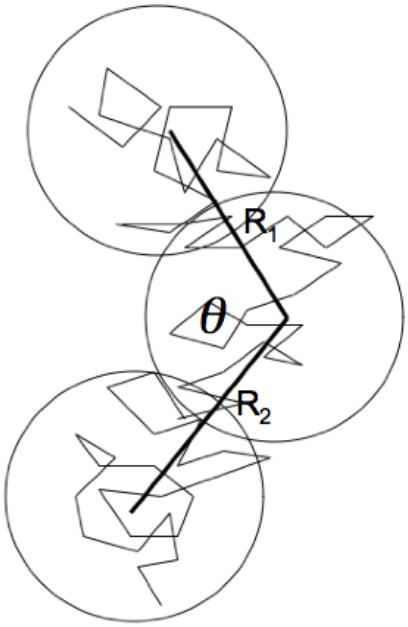


FIGURE IV.8. Depiction of the three block model mapped onto a random walk. The coarse-grained coordinates are $R_1$ and $R_2$, which are the bond vectors joining effective CG sites, and the angle, $\theta$, between them. Note that many underlying atomistic configurations are possible for each configuration of the coarse-grained coordinates.

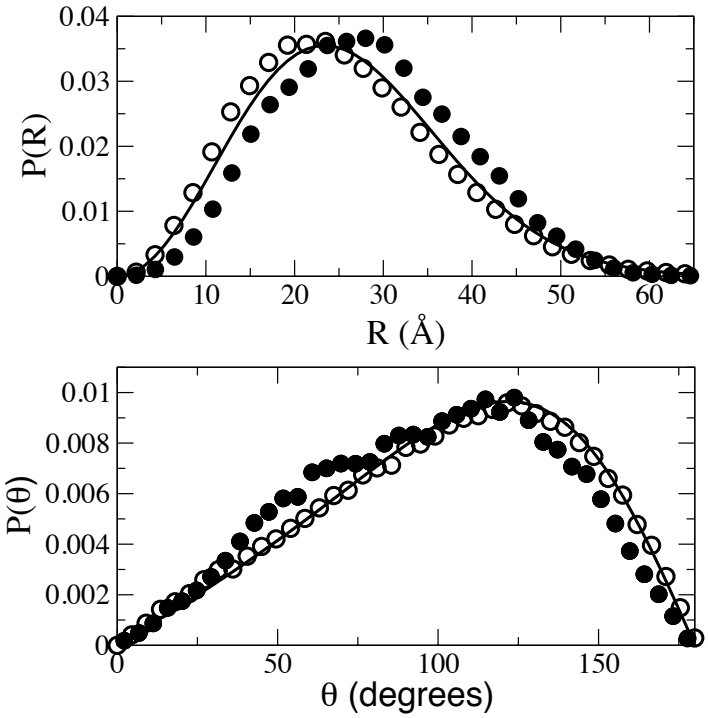


FIGURE IV.9. Distribution of the bond vector (top) and angle (bottom) from coarse-grained simulations (open circles) compared to united atom simulations (filled circles). The solid line indicates the predicted distribution for a Gaussian chain.

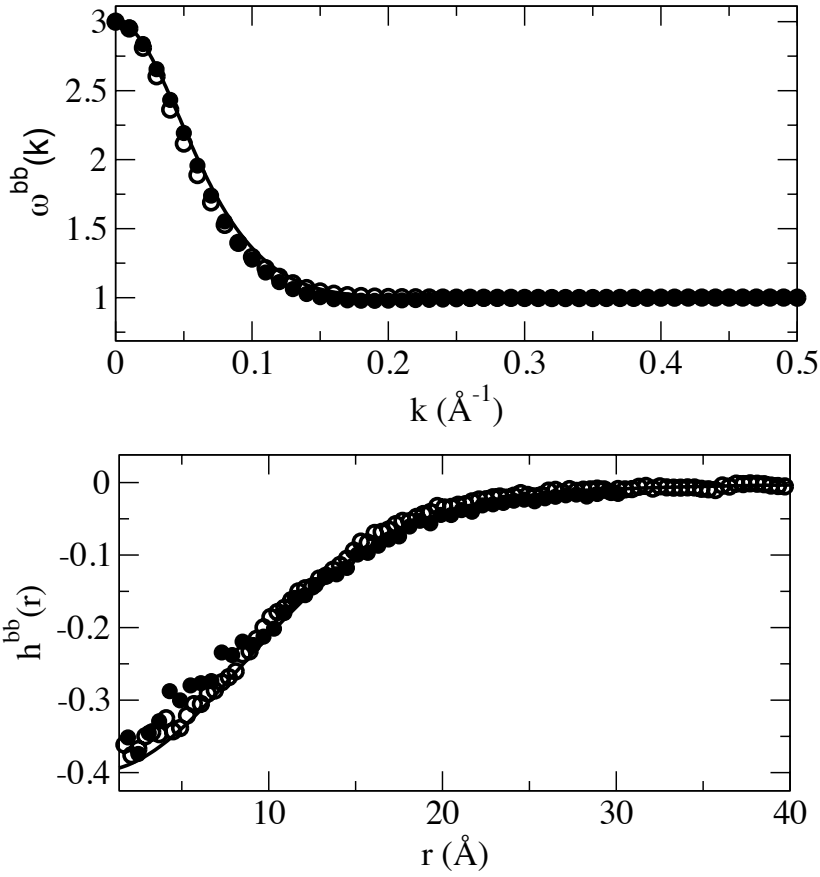


FIGURE IV.10. Comparison of the intramolecular distribution, $\omega^{bb}(k)$ (top) and intermolecular correlation function, $h^{bb}(r)$, (bottom) between block centers calculated from both 3-block and united atom simulations of PE225. The solid line depicts theoretical predictions from the coarse-grained model.

Figure IV.10 shows the intermolecular correlation function, $h^{bb}(r)$, between block centers from both the coarse-grained and united atom simulations. Typically the ratio between this distribution computed in both the coarse-grained and united atom simulation would be used in an iterative numerical scheme to optimize the pair potential. Our approach does not require any optimization since the two distributions are equivalent. This is because the coarse-grained potential reproduces the underlying free energy surface along the coarse-grained degrees of freedom and thus reproduces the correct probability distributions of coarse-grained coordinates. Figure IV.10 also presents the intramolecular distribution in Fourier space between the two levels of description.

### IV.3.4. Compressibility

It is straightforward to show that the compressibility is also preserved in coarse-graining. The isothermal compressibility is calculated from liquid state theory as

$$\hat{S}(k=0) = \rho k_B T \kappa_T \tag{IV.21}$$

Taking this definition in the two levels of description

$$\begin{aligned}
\rho_m k_B T \kappa_T^{mm} - \rho_b k_B T \kappa_T^{bb} &= \hat{S}^{mm}(0) - \hat{S}^{bb}(0) \\
&= [\hat{\omega}^{mm}(0) + \rho_m \hat{h}^{mm}(0)] - [\hat{\omega}^{bb}(0) + \rho_b \hat{h}^{bb}](0) \\
&= [N + \rho_m \hat{h}^{mm}(0)] - \frac{1}{N_b}[N + \rho_m \hat{h}^{bb}(0)]
\end{aligned}$$

hence

$$\begin{aligned} \rho_b k_B T \kappa_T^{bb} &= \frac{\rho_m k_B T \kappa_T^{mm}}{N_b} \\ \kappa_T^{bb} &= \kappa_T^{mm} \end{aligned} \tag{IV.22}$$

for any level of block description.

### IV.3.5. Total Energy Corrections

The pressure, compressibility, structural distributions (at length-scales larger than $R_g$), and free energy of the system are equivalent between UA simulations and our coarse-grained level of representation across all levels of block description. This indicates that the coarse-graining scheme is sound since all directly observable, bulk phenomena are captured; however, we now consider two related, but non-directly observable phenomena: the system potential energy and entropy. We first examine the potential energy of the two representations because this quantity is readily calculated from the molecular dynamics simulation. In the coarse-grained soft sphere representation, the average potential energy has only the contribution from the intermolecular pair potential, which we have previously shown to be given by

$$\begin{aligned} \frac{E^{soft}}{nk_BT} &= \frac{2\pi\rho}{Nk_BT}\int_0^\infty v^{cc}(r)g^{cc}(r)r^2dr \\ &\approx \frac{-Nc_0\rho}{2} \end{aligned} \tag{IV.23}$$

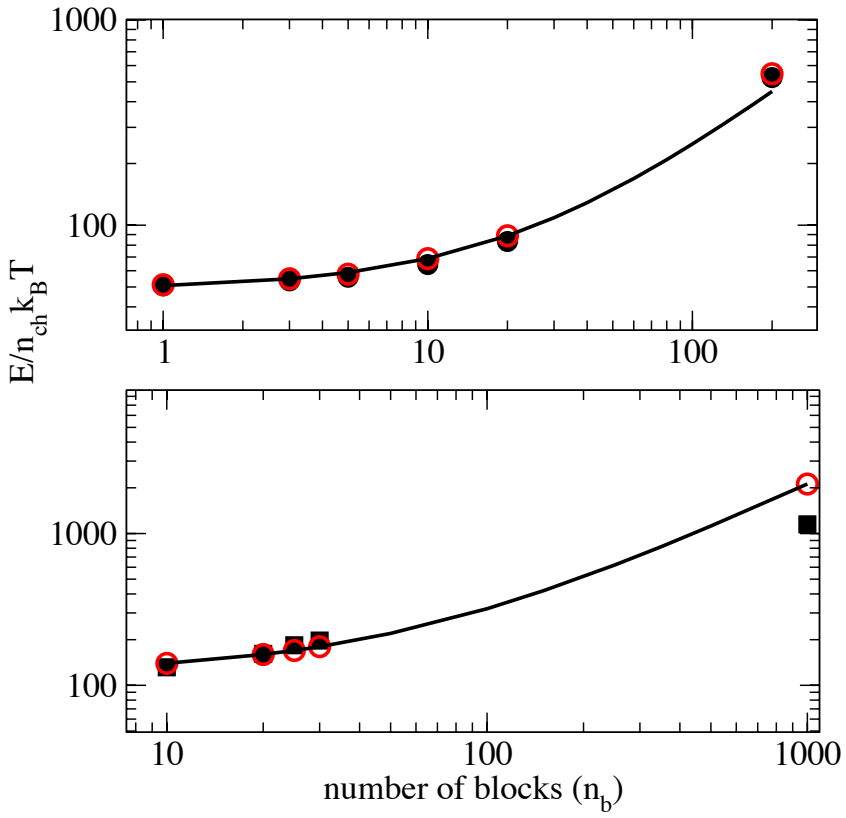


FIGURE IV.11. Internal energy calculated from coarse grained simulation of PE200 (top) and PE1000 (bottom) as a function of the number of blocks ($n_b$). The last point is the internal energy from united atom simulations. The contribution from the kinetic energy has be subtracted. The red symbols show theoretical predictions and the solid line is an extrapolation of the theory for large $n_b$.

Substitution of Equation IV.14 into Equation IV.23 gives

$$\frac{E^{soft}}{Nnk_BT} = \frac{4(\eta + c1\eta^2 + c2\eta^3)}{(1-\eta)^3} \tag{IV.24}$$

which as mentioned earlier is a free energy in the coarse-grained coordinates.

The integral in Equation IV.23 is not equivalent to the monomer-level potential energy, which is a sum of intermolecular pair interactions, $U_{inter}$ and intramolecular

interactions, $U_{intra}$, which can be decomposed further into separate contributions: bond stretching, angle bending, torsional rotation, and non-bonded (nb) pair interactions acting between monomers on the same chain.

The potential energy in the two simulations is simply calculated as the average energy minus the kinetic energy contribution. Figure IV.11 show the potential energy per molecule for two different systems, PE200 at $\rho = 0.8g/mL$ at $T = 400K$ and PE1000 at $\rho = 0.733g/mL$ and $T = 509K$ as a function of the number of effective sites, $n_b$. For comparison, the last data point is the potential energy from UA simulations, where the number of effective sites is equal to the number of united atoms. In both sets of simulations, the potential energy changes as the number sites is increased.

The energy due to the coarse-grained potential is generalized from the soft sphere limit as

$$\frac{E^{bb}}{nk_BT} = \frac{2\pi\rho_{ch}}{k_BT}\int_0^\infty v^{bb}(r)g^{bb}(r)r^2dr \tag{IV.25}$$

which again gives

$$\begin{aligned}\frac{E^{bb}}{nk_BT} &= -\frac{N\rho\hat{c}^{bb}(k=0)}{2N_b} \\ &= -\frac{\rho n_b N_b c_0}{2}\end{aligned} \tag{IV.26}$$

Equation IV.26 is the internal energy due to the coarse-grained potential which is equivalent to the excess free energy of the system in the mean field limit. However, Figure IV.11 shows an increase in energy with the number of coarse-grained sites. This is due to the addition of intramolecular bonding and angular potentials. The bond distribution is assumed a Gaussian distribution as seen in Figure IV.9 of the

form

$$P(r) = 4\pi \left[\frac{3}{\pi 8 R_{gb}^2}\right]^{3/2} r^2 \exp\left[-\frac{3r^2}{8R_{gb}^2}\right]. \quad \text{(IV.27)}$$

Since the bond energy is a harmonic potential with a Gaussian probability distribution, the average bond energy is simply the equipartition result,

$$\left\langle \frac{E_{bond}}{nk_BT} \right\rangle = \frac{3(n_b - 1)}{2} \quad \text{(IV.28)}$$

For the angular contribution we add an additional $E_{angle} \approx (n_b - 2)/2k_BT$ contribution per chain. The total predicted energy calculated from Equations IV.26 and IV.28 are shown in Figure IV.11 with red symbols. The solid line is an extrapolation of the predicted curve for increasing number of blobs. It is clear that the energy in the coarse-grained simulations is approaching that of the united atom simulations in the limit that $n_b \to N$. However, it should be stressed that this is approximate since the assumption in estimating the energy was a mean field assumption $g^{bb}(r) \to 1$, which becomes inceassingly less accurate as the local structure becomes important. As $n_b \to N$, short range excluded volume interactions become important and $g^{mm}(r)$ has local peaks due to packing effects. Nonetheless, from Figure IV.11 it is shown that the mean field approximation does give a quite reasonable estimate of the total energy when extrapolated to the monomer limit.

### IV.3.6. Entropy of Coarse-graining

Shell has developed a formalism for understanding the entropy in coarse-grained potentials, which defines a relative entropy based on the information function that discriminates between coarse-grained configurations sampled in both levels of representation.[?] Rudzinski and Noid have discussed the relative entropy in detail

in the context of numerical coarse-graining schemes such as the multiscale coarse-grained potential (MS-CG) formalism.[82] The relative entropy is minimized for a coarse-grained potential that reproduces the target distribution functions, which means that the coarse-grained potential is the many-body potential of mean force (not the pair-wise potential of mean force). Our coarse-grained formalism uses liquid state theory to derive a relationship between the coarse-grained sites (fictitious sites) and monomer sites. In other words, our coarse-graining procedure is devised to reproduce the correct distributions, thus minimizing the relative entropy without need for any variational approach.

We now consider a related quantity, the mapping entropy, which is not related to any coarse-grained model in particular, but is an intrinsic effect of coarse-graining and a direct consequence of the fact the coarse-graining reduces the dimensionality of the configuration space and smoothes the probability distributions. The mapping entropy is related to the number of atomistic configurations which can be mapped into a single coarse-grained configuration, which can be quite large when the level of coarse-graining is extreme and the underlying chain is flexible. Noid has shown that this mapping entropy is simply the difference in entropy of the atomistic model when viewed from the atomistic configurations and the coarse-grained configurations,[82]

$$S_{map} = S_{\mathbf{r}} - S_{\mathbf{R}} \tag{IV.29}$$

where $S_{\mathbf{r}}$ is the entropy in the atomistic configuration, $\mathbf{r} \in \{\mathbf{r}_1^1 ... \mathbf{r}_N^{n_{ch}}\}$, and $S_{\mathbf{R}}$, is the entropy of the same set of configurations when viewed in the coarse-grained coordinates, $\mathbf{R} \in \{\mathbf{R}_1^1 ... \mathbf{R}_{n_b}^{n_{ch}}\}$. In the context of this work $\mathbf{R}$ is the center of mass of

a group of atoms of equivalent masses, hence,

$$\mathbf{R}_i = \sum_{j\in \text{ atoms in } i} \mathbf{r}_j. \tag{IV.30}$$

The configurational entropy in the united atom model is

$$S_{\mathbf{r}} = -k_B \int d\mathbf{r} p_{UA}(\mathbf{r}) \ln[V^{Nn_{ch}} p_{UA}(\mathbf{r})] \tag{IV.31}$$

and the configurational entropy in the coarse-grained representation is

$$S_{\mathbf{R}} = -k_B \int d\mathbf{R} p_{bb}(\mathbf{R}) \ln[V^{n_{ch}n_b} p_{bb}(\mathbf{R})] \tag{IV.32}$$

where $p_{UA}(\mathbf{r})$ is the configurational probability distribution of the atomistic sites, and $p_{bb}(\mathbf{R})$ is the probability distribution for the center of mass coordinates. Substitution of the Boltzmann weights for the probability distributions gives

$$S_{\mathbf{r}} - S_{\mathbf{R}} = \left\langle \frac{E_{UA}}{T} \right\rangle_{UA} - \left\langle \frac{E_{bb}}{T} \right\rangle_{bb} + \frac{F_{UA}}{T} - \frac{F_{bb}}{T} \tag{IV.33}$$

Since the coarse-grained simulations produce the same distributions as the underlying atomistic ones, the coarse-grained potential is the correct pair potential that reproduces the multidimensional free energy surface along the coarse-grained coordinates. Therefore, the excess free energy is the same between coarse-grained at united atom simulations. The implications of this are that the entropy per site is simply the difference between the average energies in the two simulations and the

free energy difference between ideal noninteracting chains

$$\frac{S_{\mathbf{r}}}{n_{ch}k_B} - \frac{S_{\mathbf{R}}}{n_{ch}k_B} = \left\langle \frac{E_{UA}}{Nn_{ch}k_BT} \right\rangle_{UA} - \left\langle \frac{E_{bb}}{n_b n_{ch}k_BT} \right\rangle_{bb} - \frac{F_{UA}^{(0)} - F_{bb}^{(0)}}{T}. \qquad \text{(IV.34)}$$

The difference in internal energies between the two simulations are due to the additional bond and angular degrees of freedom of the system. Hence, the entropy difference is due to the fact that as $n_b$ becomes larger, there are more configurations that reproduce the same average end-to-end distance.

## IV.4. Conclusion

This chapter focused on the thermodynamic properties of the multiblock model and comparison with united atom simulations of linear polyethylene melts. We have shown that the coarse-grained model reproduces the predicted structural distributions and thermodynamic properties across multiple levels of coarse-graining. Although, all the expressions in Chapter IV could have been parameterized with the Gaussian thread model, they were intentionally left general in terms of the monomer interaction parameter $c_0$, as this parameter is essential to obtaining quantitative comparison with all-atom models. The Guassian thread results provide only a qualitative comparison. Thus, we need a procedure to obtain realistic coarse-grained potentials in terms of the parameter $c_0$, and once this is established, we will know that the structure and thermodynamics are maintained in the two models. The next chapter, Chapter V will discuss how this parameter $c_0$ can be obtained for any type of polymer architecture.

# CHAPTER V

# OBTAINING THE COARSE-GRAINED POTENTIAL FOR REALISTIC POLYMER MODELS

Chapter V discusses the method of numerically computing the coarse-grained potential, which was used in Chapter IV to compare mesoscale simulations with united atom simulations for linear polyethylene melts. This is important because most realistic polymers cannot be described quantitatively with the Gaussian thread model which was used in Chapter III. Instead, the numerical PRISM equations are solved to obtain the monomer direct correlation parameter, $c_0$, which is then used as a parameter in the coarse grained model. This chapter presents a summary of the algorithm to compute $c_0$ and the effective potential for the soft sphere, tri-block, and block averaged description of arbitrary number of blocks. Our codes to systematically compute the effective potential at various levels of detail are in the process of being made available on a website for download. This chapter may also serve as useful documentation on the use of these codes and how to implement the method for multi-scale simulations of dense polymer systems of specific chemical structure which reproduce the correct equation of state across various levels of coarse-graining.

Along with Chapter IV, a manuscript of this work is being prepared for publication with co-authors A. Clark, J. Copperman and M. Guenza. The numerical PRISM codes were initially provided by A. Yethiraj in a somewhat different format and were subsequently modified by me to incorporate the KINSOL nonlinear solver available through the SUNDIALS Suite of programs for solving nonlinear algebraic equations, and to incorporate the R-MMSA molecular closure as discussed in the next section. The code to calculate the effective potential requires as input the

monomer direct correlation parameter and is a modified version from an earlier code written in MATLAB. This chapter discusses the details of the procedure.

The parameters that enter the model directly are the direct correlation parameter, $c_0$, the thermodynamic properties of temperature, $T$, and density, $\rho$, as well as the structural properties of $N$, the number of monomers, and the effective segment size, $\sigma$. These parameters allow the method to be readily applied to a variety of conditions. Appendix A provides a Python function to calculate the effective potential which takes as an input the parameters: $N$, $T$, $\rho$, $R_g$, $n_b$, and $c_0$.

## V.1. Numerical PRISM Solution for the Direct Correlation Function

In Chapter III we used the analytic PRISM thread model as an approximation for $c_0$. While the PRISM thread model represents an idealized limiting case, it is not expected to give quantitative predictions for real chains of finite length and thickness. The extension to realistic chains can be achieved simply by using a more realistic molecular model for the polymer. The monomer total correlation function, $\hat{h}^{mm}(k)$, is given in Fourier space by the PRISM integral equation for a homopolymer fluid,[14]

$$\hat{h}^{mm}(k) = \hat{\omega}^{mm}(k)\hat{c}^{mm}(k)[\hat{\omega}^{mm}(k) + \rho\hat{h}^{mm}(k)], \tag{V.1}$$

where $\rho = N\rho_{ch}$ is the number density of monomer sites, and $\hat{c}^{mm}(k)$ is the monomer direct correlation function. We adopt the semiflexible chain model[83] as depicted in Figure V.1. In its simplest form, the model requires three parameters, the monomer hard sphere diameter, $d_{HS}$, the bond length, $l$, and the bond angle, $\theta$. For polyethylene chains we use the values of $l = 1.54$ and $\theta = 141.7$ to agree with the stiffness $q = - < \cos\theta >= 0.785$, which has been shown to be reasonable for linear

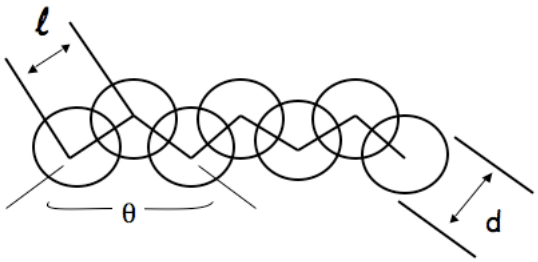


FIGURE V.1. Semiflexible chain model used as the molecular model for numerical PRISM equations. This model allows for a realistic estimate of $c_0$, which is input into the coarse-grained model.

polyethylene models. To estimate the intramolecular distribution, we then use the Koyama distribution which can be calculated using the method from reference.[83]

Having the intramolecular distribution, we solve the PRISM equation, Eqn V.1, with the reference molecular mean spherical approximation (R-MMSA) closure given by,

$$\begin{aligned} \omega(r) * c(r) * \omega(r) \quad &= \omega(r) * c^{(0)}(r) * \omega(r) - \omega(r) * \beta v(r) * \omega(r), \\ & \qquad r > d_{HS}, \end{aligned} \tag{V.2}$$

where the asterisks denote convolution integrals, $c^{(0)}$ is the direct correlation function of a reference purely hard sphere chain, and $v(r)$ is the attractive part of the potential given as a Lennard Jones tail,

$$\begin{aligned} v(r) \quad &= 4\epsilon \left[ \left(\tfrac{\sigma}{r}\right)^{12} - \left(\tfrac{\sigma}{r}\right)^{6} \right], \quad r > \sigma \\ & \qquad v(r) = 0, \quad r < \sigma \end{aligned} \tag{V.3}$$

Inside the hard core, impenetrability is ensured by enforcing the condition

$$h(r) = -1, \quad r < d_{HS}. \tag{V.4}$$

Once the closure is specified by Equations V.2 - V.4, the PRISM equation is solved numerically using the standard Picard iteration with fast Fourier transform or with the KINSOL nonlinear algebraic solver available through the SUNDIALS suite of programs.[84]

Once a solution of is achieved, the value of $c_0$ is determined as

$$c_0 = \frac{\hat{h}(0)}{\rho N \hat{h}(0) + N^2}. \tag{V.5}$$

Figure V.2 shows a plot of $c_0$ for different densities for a chain of $N = 44$, $N = 100$, and $N = 200$. Most noticeably, the dependence of $c_0$ on density is stronger than the linear dependence predicted by the idealized thread model. The right side of Figure V.2 shows the $c_0$ as a function of chain length for $\rho = 0.03153$ sites/$\mathring{A}^3$. The value of $c_0$ approaches an asymptotic value for large $N$ which corresponds to a leveling off of the chain-length dependence of the pressure. This limiting value of $c_0$ can be used to perform coarse-grained simulations of large chains where all-atom simulations are prohibitive.

In performing numerical PRISM calculations we adjust $d_{HS}$ to agree with the predicted equation of state given by equation IV.7, so that the pressure agrees with United Atom simulation data and $c_0$ determined from Equation V.5. We also check that this value of $d_{HS}$ yields a good representation of the monomer structure as given by the radial distribution function, $g(r)$. Figure V.4 shows $g(r)$ calculated from PRISM theory and from United Atom simulations for $N = 100$ and a monomer

density if $\rho = 0.03355$ sites/$\mathring{A}^3$.

It is interesting to compare the effective pair potential obtained from the PRISM calculation using the SFC model with that obtained from the thread model. Figure V.3 shows the effective pair potential for the intermediate density, $\rho = 0.03656$ sites/$\mathring{A}^3$, where the molecular model input into the theory is calculated from PRISM theory for both the SFC model and the thread model. The SFC model results in a stronger and longer-ranged repulsive core; however the attractive well is of comparable magnitude. The inset show the virial force $F(r)r^3/k_BT$ which is used to calculate the pressure equation. The repulsive contribution is much larger for the case of the SFC model. This is due to the finite-sized hard sphere core in the SFC model, which results in a stronger repulsive force. Because the radial distribution function is fairly insensitive to the shape of the potential, the structure is nearly identical between the thread model and the SFC model; however, because the pressure depends on the virial force, it is extremely sensitive to the potential, and thus the SFC model should be used since the value of $c_0$ chosen is such as to match the pressure.

## V.2. Calculation of the Coarse-Grained Potential

Our course grained description represents each polymer chain in a melt as a single soft sphere[38,39,66] or as a collection of $n_b$ soft connected blobs.[40,41] While Chapter II provided a theoretical derivation of this representation, here the numerical procedure is summarized here for completeness. We take the polymer to be comprised

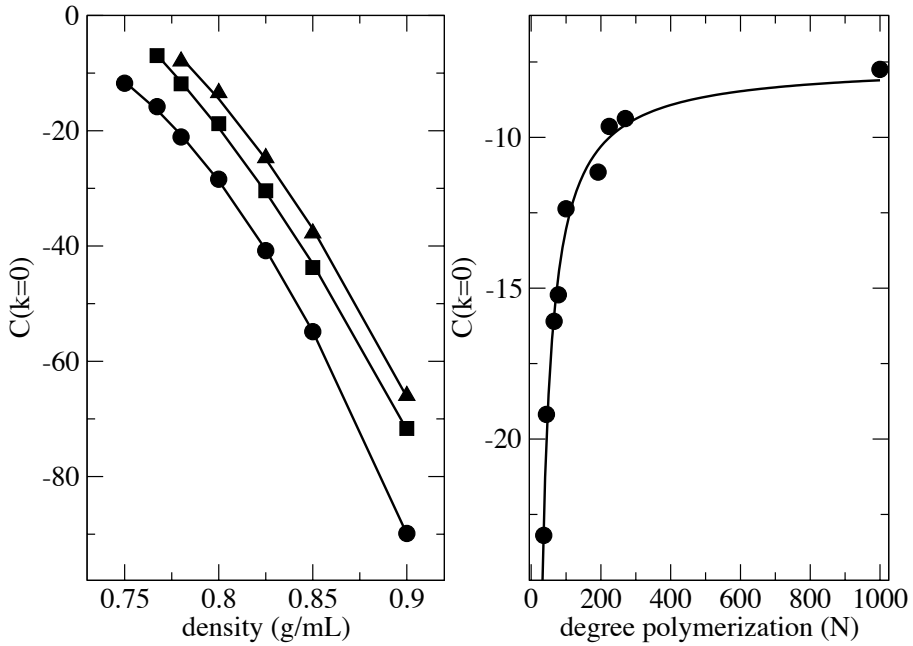


FIGURE V.2. Left: Calculated value of $c_0$ from numerical PRISM using a simple SFC chain model as a function of the monomer site density. Three different chain lengths are shown; $N = 44$ (circles), $N = 100$ (squares) and $N = 200$ (triangles). The line is a fit to a quadratic polynomial to serve as a guide to the eye. Right: Calculated values of $c_0$ from numerical PRISM as a function of polymer chain length at fixed density, $\rho = 0.03153$ sites/$\mathring{A}^3$ (circles). The solid line is a fit to the form $a + b/N$.

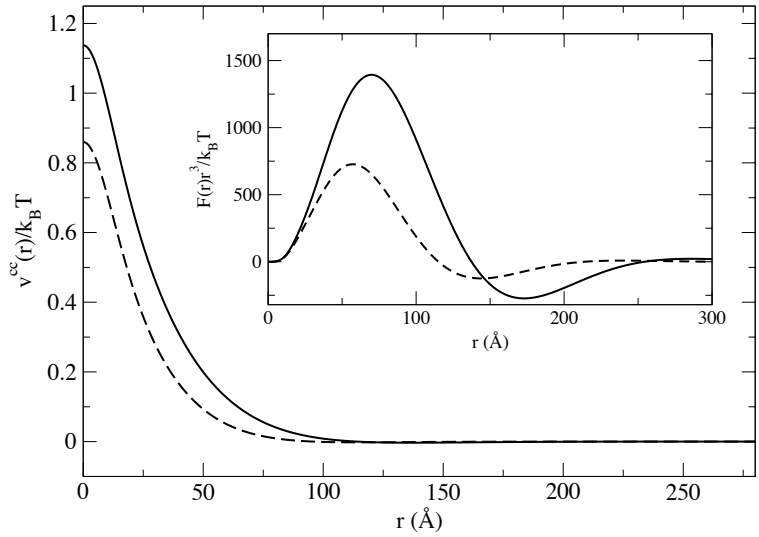


FIGURE V.3. The effective pair potential for PE100 at an intermediate density of $\rho = 0.03656$ sites/$\mathring{A}^3$ The solid line is the potential calculated using numerical PRISM with the SFC chain model. The dashed line is the same potential using the thread model value for $c_0$ for comparison. The inset shows the virial force.

of equivalent sites of $N$ monomers with a chain density $\rho_{ch}$, and an effective segment length $\sigma = \sqrt{6/N}R_g$ with $R_g$ being the polymer radius of gyration and $R_{gb} = Rg/n_b$ the blob radius of gyration. The number of underlying monomers per blob is given as $N_b = N/n_b$. Coarse-grained or fictitious interacting sites are taken to be located at the center of mass of the polymer chain for the soft sphere model or at the centers of mass of several monomers along the same chain for the connected blob model. The relation between center of mass fictitious sites and real monomer sites, originally proposed by Krakoviack, *et al*,[37] is derived by solving a generalized matrix Ornstein Zernike equation, and was extended by Clark, *et al*[41] for the multi-blob model. All codes to calculate the effective potential are readily available upon request.

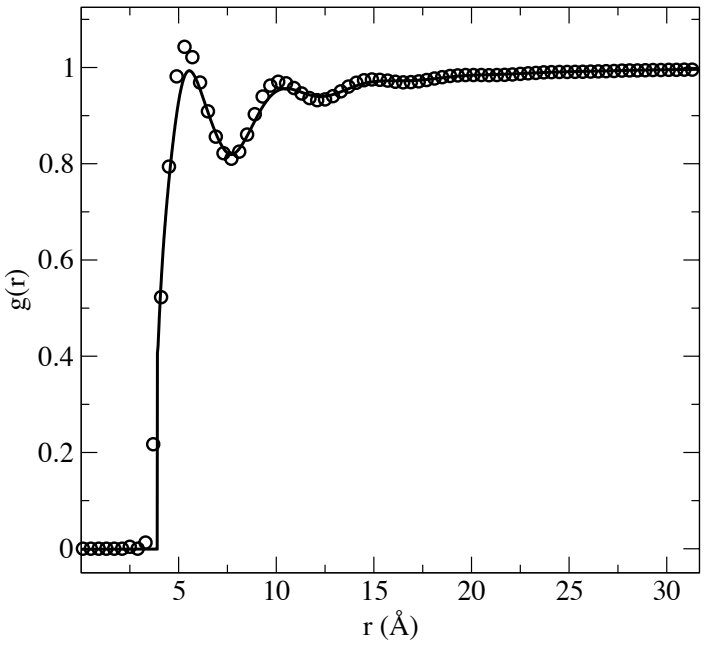


FIGURE V.4. The monomer radial distribution function for PE with $N = 100$ at a monomer density $\rho = 0.03355$ sites/$\mathring{A}^3$ calculated from United Atom simulations (solid line) and from PRISM calculation using the SFC model with $d_{HS} = 3.9\mathring{A}$ which gives the best agreement between the pressures
.

### V.2.1. Soft Spere Potential

For the case where the number of blobs is one, meaning each chain is represented as a single interaction site, one recovers the relation,

$$\hat{h}^{cc}(k) = \left[\frac{\hat{\omega}^{cm}(k)}{\hat{\omega}^{mm}(k)}\right]^2 \hat{h}^{mm}(k), \tag{V.6}$$

where $\hat{h}^{cc}(k)$ is the total correlation function between center of mass, fictitious sites. $\hat{h}^{mm}(k)$ is the total correlation function between monomers, and $\hat{\omega}^{mm}(k)$ and $\hat{\omega}^{cm}(k)$ are the intramolecular distributions between monomers or between monomers about the center of mass respectively.

As an approximation, valid at large r, we take the direct correlation function to be a constant in Fourier space, $\hat{c}^{mm}(k) = \hat{c}^{mm}(0) = c_0$. Substitution of Equation V.1 into Equation V.6 gives,

$$\hat{h}^{cc}(k) = \frac{c_0[\hat{\omega}^{cm}(k)]^2}{1 - \rho c_0 \hat{\omega}^{mm}(k)} \ . \tag{V.7}$$

For the soft sphere model, the direct correlation function between coarse-grained sites, $\hat{c}^{cc}(k)$, is identical to that for a simple fluid,

$$\hat{c}^{cc}(k) = \frac{\hat{h}^{cc}(k)}{1 + \rho_{ch}\hat{h}^{cc}(k)}. \tag{V.8}$$

The effective soft sphere potential is given by the hypernetted chain (HNC) closure,[8]

$$\frac{v^{cc}(r)}{k_B T} = -\ln\left[h^{cc}(r) + 1\right] + h^{cc}(r) - c^{cc}(r). \tag{V.9}$$

The procedure formulated in this manner is easy to implement and the codes to calculate the potential are available upon request. Briefly the algorithm is as follows:

First, the intramolecular distributions are calculated. The monomer intramolecular distribution is given by the Debye formula,

$$\omega^{mm}(k) = \frac{2N(e^{-k^2R_g^2} + k^2R_g^2 - 1)}{k^4R_g^4}, \tag{V.10}$$

whereas the monomer-cm distribution is given by

$$\omega^{cm}(k) = \frac{N\sqrt{\pi}}{kR_g}e^{-k^2R_g^2/12}\mathrm{erf}\left[\frac{kR_g}{2}\right]. \tag{V.11}$$

From Equation V.7, $\hat{h}^{cc}(k)$ is calculated and subsequent numerical Fourier transform of Equations V.7 and V.8 gives the effective potential from Equation V.9.

### V.2.2. Tri-Block Potential

For chains represented by 3 CG sites per chain (tri-block model) the two terminal CG chains are distinct from the central CG site giving rise to three distinct block combinations of block-block tcfs. Using the notation from our previous work[41] the intermolecular tcfs between block centers, $\hat{h}^{bb}_{\alpha\beta}(k)$ with block indices $\alpha$ and $\beta$ and new omega distributions we have the extention of equation V.7

$$\begin{aligned}\hat{h}^{bb}_{11}(k) &= \hat{h}^{bb}_{13}(k) = \hat{h}^{bb}_{31}(k) = \hat{h}^{bb}_{33}(k) \\ &= \frac{c_0[\hat{\omega}^{bm}_0(k) + \hat{\omega}^{bm}_1(k) + \hat{\omega}^{bm}_2(k)]^2}{1 - \rho c_0\hat{\omega}^{mm}(k)}\end{aligned} \tag{V.12}$$

$$\begin{aligned}\hat{h}^{bb}_{12}(k) &= \hat{h}^{bb}_{23}(k) = \hat{h}^{bb}_{21}(k) = \hat{h}^{bb}_{32}(k) \\ &= \frac{c_0[(\hat{\omega}^{bm}_0(k) + \hat{\omega}^{bm}_1(k) + \hat{\omega}^{bm}_2(k))(\hat{\omega}^{bm}_0(k) + 2\hat{\omega}^{bm}_1(k))]^2}{1 - \rho c_0\hat{\omega}^{mm}(k)}\end{aligned} \tag{V.13}$$

and

$$\hat{h}_{22}^{bb}(k) = \frac{c_0[\hat{\omega}_0^{bm}(k) + 2\hat{\omega}_1^{bm}(k)]^2}{1 - \rho c_0 \hat{\omega}^{mm}(k)} \tag{V.14}$$

The direct correlation functions are then expressed in term of the intramolecular distributions by inserting Equations V.12-V.14 into the matrix Ornstein-Zernike equation of the coarse-grained fluid. The resulting direct correlation functions are lengthy but presented here in their full form,

$$\begin{aligned}\hat{c}_{11}^{bb}(k) = -\frac{1}{\hat{D}(k)} \Big( & \hat{h}_{11}^{bb}(k) - 2\hat{h}_{12}^{bb}(k)\hat{\omega}_1^{bb}(k) \\ & + \hat{h}_{22}^{bb}(k)(\hat{\omega}_1^{bb}(k))^2 - \rho_{ch}(\hat{h}_{12}^{bb}(k))^2 + \rho_{ch}\hat{h}_{11}^{bb}(k)\hat{h}_{22}^{bb}(k) \Big)\end{aligned} \tag{V.15}$$

$$\begin{aligned}\hat{c}_{12}^{bb}(k) = -\frac{1}{\hat{D}(k)} \Big( & \hat{h}_{12}^{bb}(k)(1 + 2(\hat{\omega}_1^{bb}(k))^2 + \hat{\omega}_2^{bb}(k)) + 2\rho_{ch}(\hat{h}_{12}^{bb}(k))^2\hat{\omega}_1^{bb}(k) \\ & - \hat{\omega}_1^{bb}(k)(2\hat{h}_{11}^{bb}(k) + \hat{h}_{22}^{bb}(k) + \hat{h}_{22}^{bb}(k)\hat{\omega}_2^{bb}(k) + 2\rho_{ch}\hat{h}_{22}^{bb}(k)\hat{h}_{11}^{bb}(k)) \Big)\end{aligned} \tag{V.16}$$

$$\begin{aligned}\hat{c}_{22}^{bb}(k) = -\frac{1}{\hat{D}(k)} \Big( & 4(\hat{\omega}_1^{bb}(k))^2\hat{h}_{11}^{bb}(k) - 4\hat{\omega}_1^{bb}(k)(1 + \hat{\omega}_2^{bb}(k))\hat{h}_{12}^{bb}(k) \\ & - 2\rho_{ch}(1 + \hat{\omega}_2^{bb}(k))(\hat{h}_{12}^{bb}(k))^2 + \hat{h}_{22}^{bb}(k)(1 + \hat{\omega}_2^{bb}(k))(1 + \hat{\omega}_2^{bb}(k) + 2\rho_{ch}\hat{h}_{11}^{bb}(k)) \Big)\end{aligned} \tag{V.17}$$

with

$$\hat{D}(k) = (2(\hat{\omega}_1^{bb}(k))^2 - \hat{\omega}_2^{bb}(k) - 1)(1 - 2(\hat{\omega}_1^{bb}(k))^2 + \hat{\omega}_2^{bb}(k) - 4\rho_{ch}\hat{\omega}_1^{bb}(k)\hat{h}_{12}^{bb}(k) + \rho_{ch}\hat{\omega}_2^{bb}(k)\hat{h}_{22}^{bb}(k) + \rho_{ch}(2\hat{h}_{11}^{bb}(k) + \hat{h}_{22}^{bb}(k) - 2\rho_{ch}(\hat{h}_{12}^{bb}(k))^2 + 2\rho_{ch}\hat{h}_{11}^{bb}(k)\hat{h}_{22}^{bb}(k))) \tag{V.18}$$

In order to to obtain the tri-block potential, we use the results for the tri-block intramolecular distributions calculated by Clark and Guenza.[42] The monomer-monomer distribution is given by the generalized Debye formula,

$$\hat{\omega}^{mm}(k) = \frac{2N}{n_b^2 k^4 R_{gb}^4}(k^2 R_{gb}^2 n_b - 1 + e^{-n_b k^2 R_{gb}^2}). \tag{V.19}$$

For the block-monomer and block-block distributions, distinct block sites are represented by Greek indices $\alpha$ and $\beta$ and the block separation is given by $\gamma = |\alpha - \beta|$. For the tri-block model $\gamma \in 0, 1, 2$ and the distributions of monomers about blocks on the same site, $\gamma = 0$, is given as

$$\omega_0^{bm}(k) = \frac{N\sqrt{\pi}}{kR_g} e^{-k^2 R_g^2/12} \mathrm{erf}\left[\frac{kR_g}{2}\right], \tag{V.20}$$

whereas the block-monomer distribution of monomers on block, $\alpha$, with block $\beta$ is

$$\omega_{\gamma\neq 0}^{bm}(k) = \frac{N}{k^2 R_{gb}^2} e^{-k^2 R_{gb}^2[2+6(\gamma-1)]/6}(1 - e^{-k^2 R_{gb}^2}). \tag{V.21}$$

Lastly, the block-block distribution is given as

$$\omega_\gamma^{bb}(k) = N e^{-k^2 R_{gb}^2[4+6(\gamma-1)]/6}. \tag{V.22}$$

This completes the tri-block description. Once again equation V.19-V.22 are used to derive expressions for $h^{bb}(k)$ and $c^{bb}(k)$, using Equations V.12-V.14 and Equations V.15-V.17. The potential is again calculated numerically after Fourier transform using the HNC potential, yielding three potentials between block types, $v_{AA}(r)$, $v_{BB}(r)$, and $v_{AB}(r)$.

### V.2.3. Block Averaged Potential

When there are more than five CG sites per chain end effects become negligible and we use a block-averaged description which simplifies the expressions. A detailed analysis of the properties of the block-averaged potential is presented in a recent paper[41] The procedure to derive the analytical potential was described in Chapter II. The numerical procedure begins the same way by calculating the intramolecular distributions in the block averaged limit. For the monomer-monomer distributions we have,

$$\hat{\Omega}^{mm}(k) = \frac{2}{n_b^2 k^4}(k^2 n_b - 1 + e^{-n_b k^2}). \tag{V.23}$$

The block-monomer and the block-block distributions in the chain averaged limit are

$$\hat{\Omega}^{bm}(k) = \frac{1}{n_b}\left[\frac{\sqrt{\pi}}{k} Erf\left(\frac{k}{2}\right) e^{-\frac{k^2}{12}} - 2\left(\frac{e^{-n_b k^2} - n_b e^{-k^2} + n_b - 1}{k^2 n_b (e^{-k^2} - 1)}\right) e^{-k^2/3}\right] , \tag{V.24}$$

and

$$\hat{\Omega}^{bb}(k) = \frac{1}{n_b} + 2\left[\frac{e^{-n_b k^2} - n_b e^{-k^2} + (n_b - 1)}{n_b^2 (e^{-k^2} - 1)^2}\right] e^{-2k^2/3} , \tag{V.25}$$

The next step is to use the result from solving the matrix Ornstein-Zernike equation for $h^{bb}(k)$, which is done numerically using tabulated k-values,

$$\hat{h}^{bb}(k) = n_b \hat{\Omega}^{bb}(k)\hat{c}^{bb}(k)\left[n_b \hat{\Omega}^{bb}(k) + \rho_b \hat{h}^{bb}(k)\right] . \tag{V.26}$$

The direct correlation function is calculated from the Ornstein-Zernike relation as

$$\hat{c}^{bb}(k) = \frac{\hat{h}^{bb}(k)}{n_b\hat{\Omega}^{bb}(k)\left[n_b\hat{\Omega}^{bb}(k) + \rho_b\hat{h}^{bb}(k)\right]} \tag{V.27}$$

. The distributions in real space are calculated from numerical Fourier transform of Equation V.26 and Equation V.27. The interaction potential is calculated by numerically evaluating the HNC potential as above.

### V.2.4. Effective Bond and Angle Potentials

For the multi-block model, bonded sites are given a bond potential derived from the direct Boltzmann inversion of the probability distribution of the effective bond length,

$$v_{\text{bond}}(r) = -k_B T \ln\left[P(r)/r^2\right] \tag{V.28}$$

where

$$P(r) = 4\pi\left[\frac{3}{\pi 8R_{gb}^2}\right]^{3/2} r^2 \exp\left[-\frac{3r^2}{8R_{gb}^2}\right]. \tag{V.29}$$

giving,

$$v_{bond} = \frac{3k_B T r^2}{8R_{gb}^2}. \tag{V.30}$$

The angle potential is similarly computed

$$v_{\text{angle}}(\theta) = -k_B T \ln\left[P(\theta)/sin(\theta)\right] \tag{V.31}$$

where the angular probability distribution for a random walk chain is given by[85]

$$P(\theta) = \frac{(1-a^2)^{3/2}\sin\theta}{\pi(1-a^2\cos^2\theta)^2}\left[\frac{1+2a^2\cos^2\theta\arccos(-a\cos\theta)}{\sqrt{1-a^2\cos^2\theta}} + 3a\cos\theta\right] \tag{V.32}$$

with $a \rightarrow -0.25$ for long chains. All sites separated more than two atoms apart interact via the pair potential derived above. As seen in Chapter IV, this model accurately reproduce the distributions of dense polymer melts.

### V.2.5. Conclusion

This chapter presented a method of calculating the numerical coarse-grained potential for realistic polymer melts. The procedure involves first mapping the real chain onto the semi-flexible chain model and solving the numerical PRISM equation using the molecular R-MMSA closure. This provides a reasonable estimate to the direct correlation parameter, $c_0$. Then the numerical procedure to derive the potential was presented along with the details of computing the effective bond and angle interaction.

# CHAPTER VI

## MULTISCALE MODELING OF MACROMOLECULAR LIQUIDS AND BLENDS

Chapter VI presents an application of the coarse-grained procedure in a novel multi-scale modeling scheme. As stated in Chapter I polymers are complex fluids with many length scales of interest ranging from the local scale to the global. The problem with coarse-graining procedures is that the information on the local length scale is lost. This chapter presents a hybrid scheme where two simulates are run independently, one at the united atom level and one at the soft sphere level and information of the two different length scales are combined to provide the complete monomer-level radial distribution function. This chapter presents results for a variety of homopolymer melts of different chemical structure as well as mixtures. The coarse-graining procedure for mixtures is presented in more detail in Chapter VII. Here we focus simply on the results and the multiscale modeling procedure.

The work in this chapter resulted in two publications, co-authored with I. Lyubimov and M. Guenza, entitled "Multiscale Modeling of Coarse-Grained Macromolecular Liquids"[74] and "Multiscale Modeling of Polymer Mixtures: Scale Bridging in the Athermal and Thermal Regime"[86] Mesoscale simulations were performed using our own MD code on a single PC workstation or on the LONI Queenbee supercomputer through the XSEDE project funded by NSF. United atom simulations of various architectures were generously provided by Jaramillo and co-workers.[27,28]

## VI.1. Introduction

Understanding the structure of complex fluids hinges on our ability of achieving a detailed picture of the system on an extended range of lengthscales. Two fundamental, molecular lengthscales are relevant in the study of any macromolecular liquid, namely the monomer lengthscale, $l$, which is local, and the molecular radius-of-gyration, $R_g = l\sqrt{N/6}$, where $N$ is the molecular degree of polymerization, which roughly represents the overall size of the polymer. Because $R_g$ increases with the number of monomers in the chain, those two lengthscales can be separated by many orders of magnitude in real macromolecular systems of practical application.

Since coarse-graining techniques greatly reduce the complexity and degrees of freedom of the underlying atomistic structure, they are very useful in providing information at large length and timescales and of bulk quantities; however information on the local scale, which is often important in understanding the mechanism of large scale motions, is lost in coarse-graining. As a consequence, techniques have been developed to merge the coarse-grained description with local information. In the so-called "multiscale modeling" procedures a hierarchy of simulations are performed on the system coarse-grained at different characteristic lengthscales, and then the information obtained from those simulations is combined into one overall description, which includes all the lengthscales of interest.

The method presented in this chapter is a multiscale modeling procedure for homopolymer melts and blends. As an example system we consider linear chains of polyethylene (PE), polyisobutylene (PIB), as well as polypropylenes in their head-to-head (hhPP), istotactic (iPP), as well as syndiotactic forms (sPP). Here, the lengthscales of interest are the monomer and the radius-of-gyration, so that two simulations have to be combined, one at the monomer level of description, and one

where polymers are represented at the $R_g$ level, or mesoscale simulation (MS-MD). When dealing with polymer mixtures, a new lengthscale of concentration fluctuations emerges which diverges as the system approaches its phase transition. As this largest lengthscale of interest diverges, one would be tempted to neglect the details of the local scale; however, such a procedure risks losing pertinent information, since the monomeric structure of a blend's components largely determines its glass transition temperature, as well as the shape of its phase diagram. Both local and global scale information need to be accounted for to achieve a complete thermodynamic and dynamic description of the mixture.

The approach taken in this chapter is to perform molecular dynamic simulations of the liquid of polymers described as soft colloidal particles in a MS-MD simulation, and then to combine the structural information with the outcome of a united atom molecular dynamic (UA-MD) simulation for the local description, through our multiscale modeling procedure. An advantage of this multiscale modeling procedure is that it is formally compatible with the first principle formalism used to coarse-grain the polymeric structure as both rely on the Ornstein-Zernike equation along with the introduction of auxiliary sites. Thus the same coarse-graining procedure can be used not only to remove internal degrees of freedom, but also in the opposite way to reintroduce *a posteriori* those those internal degrees of freedom after the MS-MD is completed. It is shown that this approach reproduces pair correlation functions at a high computational efficiency, providing a method of extending simulations to large length scales of interest.

## VI.2. The Multiscale Method

The coarse-grained model has already been described in detail in previous chapters and is not reproduced here. This model is used to describe systems at the large and medium lengthscale where the statistical spatial distribution of monomers follows a Gaussian function. The extension of this description to polymer blends is presented in Chapter VII. For all of the simulations considered in this chapter, we adopted the analytical PRISM thread result for the monomer-level distribution functions as this model provides an adequate description of the polymer structure at the large length scales for which we are interested. The advantage of using the analytical PRISM expression is that it is explicitly parameter dependent, and thus straightforward to apply to different polymer systems defined by different values of structural and thermodynamic parameters. Once the formalism to describe analytically the structure of a liquid of polymers in a coarse-grained representation is solved, the effective potential between coarse-grained units is obtained numerically using the HNC closure and numerical Fourier transform of the distributions.

The overall multiscale modeling scheme is depicted in Figure VI.1. We begin by defining the model parameters that will be used in calculated the numerical coarse-grained potential and running mesoscale simulations of the soft sphere model. We also simultaneously and independently run a more detailed united atom simulation of the same system with fewer numbers of chains, but enough to capture the relvent structural distributions at the local scale. From the mesoscale soft sphere simulation we calculate the distribution of center of mass sites, $h^{cc}(r)$, whereas from the united atom simulation we calculate the intramolecular distributions $\omega^{mm}(k)$ and $\omega^{cm}(k)$ as well as the local intermolecular distribution $h^{mm}(r)$.

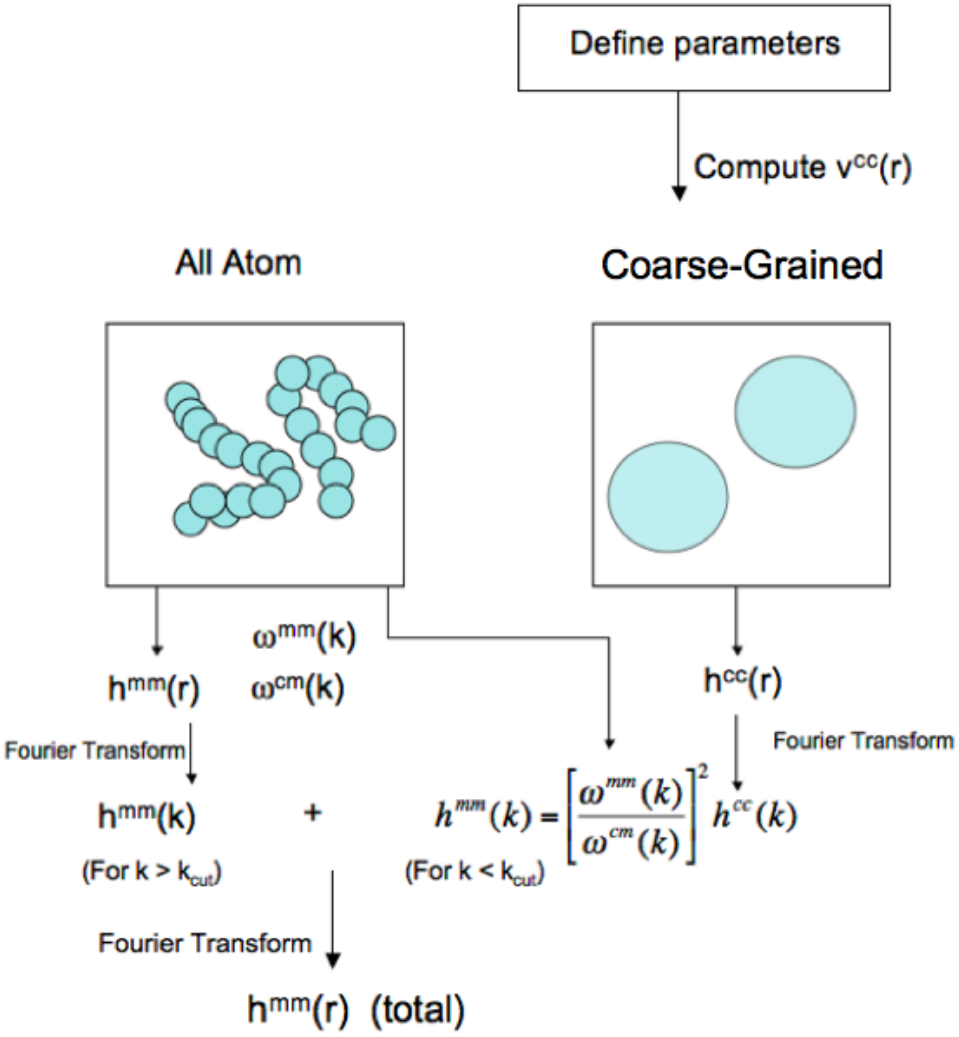


FIGURE VI.1. The Multiscale modeling procedure to calculate the total monomer distributions at all length-scales of interest. The total correlation function calculated from different simulations are combined in k-space at an intermediate value of k, and subsequently numerically Fourier Transformed to real space.

The short UA simulation input to the multiscale modeling procedure only requires a number of polymers of the order of $\sqrt{N}$, which is much smaller than the number of polymers that would need to be simulated in a full UA-MD to obtain the complete global structure. The key step is to obtain the monomer-monomer distribution functions on the global scale, small $k$, from the coarse-grained simulations. To accomplish this we calculate the inverse of Equation V.6 numerically,

$$h^{mm}(k) = \left[\frac{\omega^{mm}(k)}{\omega^{cm}(k)}\right]^2 h^{cc}(k) \ , \tag{VI.1}$$

where mesoscale simulations provide $h^{cc}(k)$ while the short UA MD simulations are used to determine the intramolecular form factors, $\omega^{mm}(k)$ and $\omega^{cm}(k)$.

Figure VI.2 shows $h^{mm}(k)$ (solid line) calculated from the mesoscale simulation using Equation VI.1 for several of the polymer melts where each chain has 96 $CH_x$ units, with $x = 1, 2$, or 3. The calculated $h^{mm}(k)$ (solid line) is compared to the full UA MD simulation (symbols). As expected, the renormalized mesoscale simulation distributions compare well to UA MD simulations for the small k range (large r), and begin to diverge as k increases.

The final step is to combined the numerical results from the mesoscale simulations (solid lines in Figure VI.2) with the united atom simulation at small range. This is done in Fourier space such that the total distribution function is determined after transformation back to real space.

Figures VI.3-VI.6 display the comparison of the total correlation function obtained with our procedure and data from extended UA simulations. The left panel of the Figures show the total correlation function in reciprocal space, $h^{mm}(k)$,

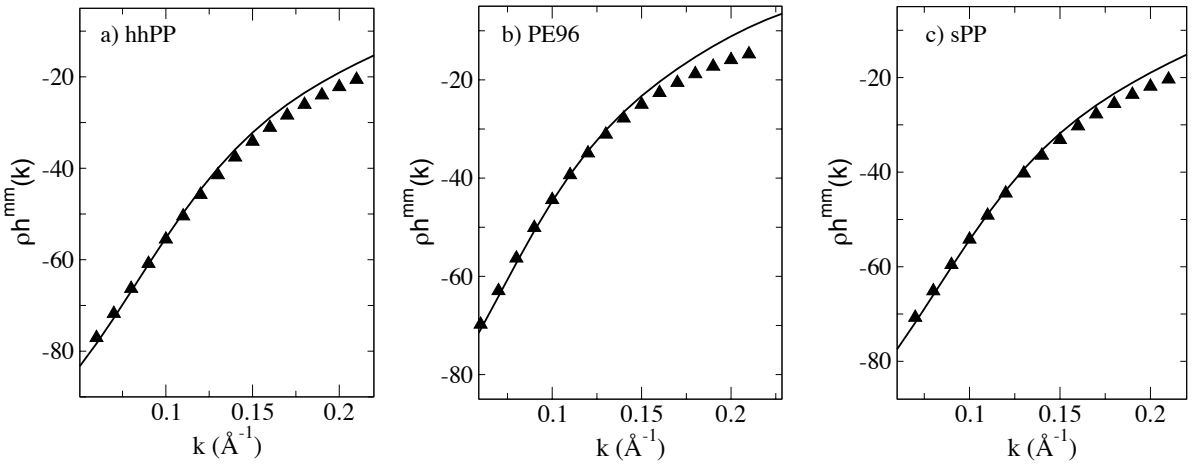


FIGURE VI.2. Plot of $h^{mm}(k)$ for different polymer melts (hhPP, PE, and sPP). Solid line depicts $h^{mm}(k)$ calculated using Equation VI.1. Symbols represent data points from full UA MD simulation.

for various polymer melts, (sPP, hhPP, iPP, and PIB) and for varying chain lengths of polyethylene (PE). $h^{mm}(k)$ is obtained by combining the large scale data (small $k$) from the mesoscale simulations with the small scale data (large $k$) from united atom simulations. The vertical dashed line indicates the distance at which the MS-MD is combined with the UA MD simulation. Note that this occurs at an intermediate distance between the local peak and the global feature, so that neither information about the long range structure, nor the local structure is lost in extrapolating the connection between the two curves for $h^{mm}(k)$.

The right panels of Figures VI.3-VI.5 show the total correlation function, $h^{mm}(r)$, for polymer melts, obtained by taking the Fourier transform of $h^{mm}(k)$. The function, $h^{mm}(r)$, provides a complete description of the liquid structure and thermodynamic properties. In performing the discrete Fourier transform of the multiscale total correlation function, a sampling step of $\Delta k = 0.01\mathring{A}^{-1}$ was used,

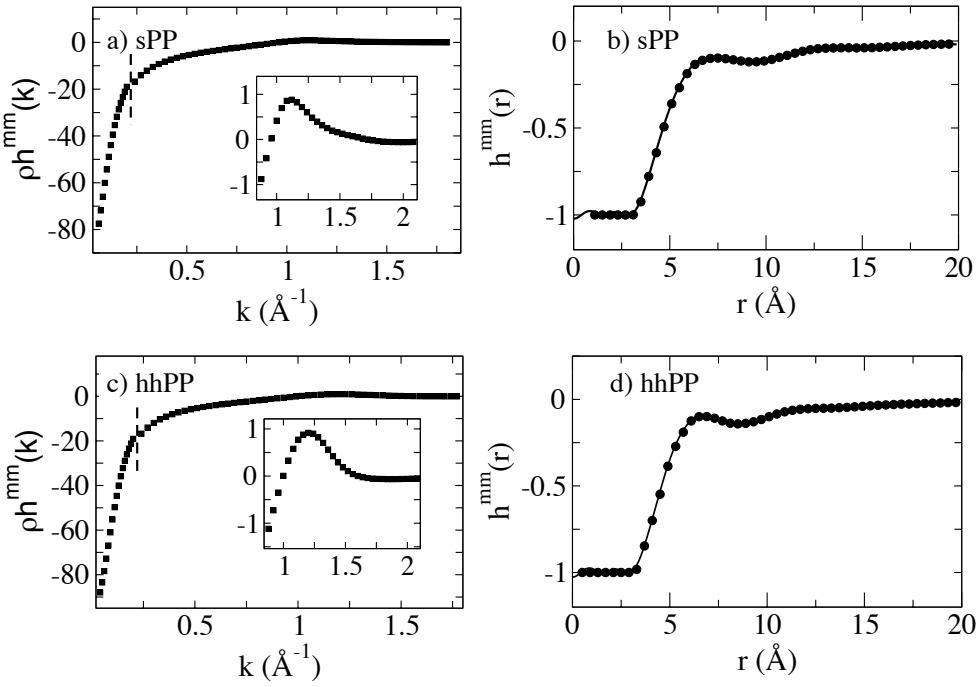


FIGURE VI.3. Left: Plot of the total correlation function, $h^{mm}(k)$, for polymer melts of (a) sPP and (c) hhPP, obtained by combining mesoscale and UA MD simulations. Mesoscale simulation depicts $h^{mm}(k)$ over the small k range whereas UA simulation provides data over the large k range. The dashed line indicates the point at which the two simulations were combined. The inset depicts the local peak. Right: Plot of the related $h^{mm}(r)$, the total correlation function in real space for (b) sPP and (d) hhPP. The solid line depicts $h^{mm}(r)$ calculated using our multiscaling approach and the open circles represent data points from UA MD simulations.

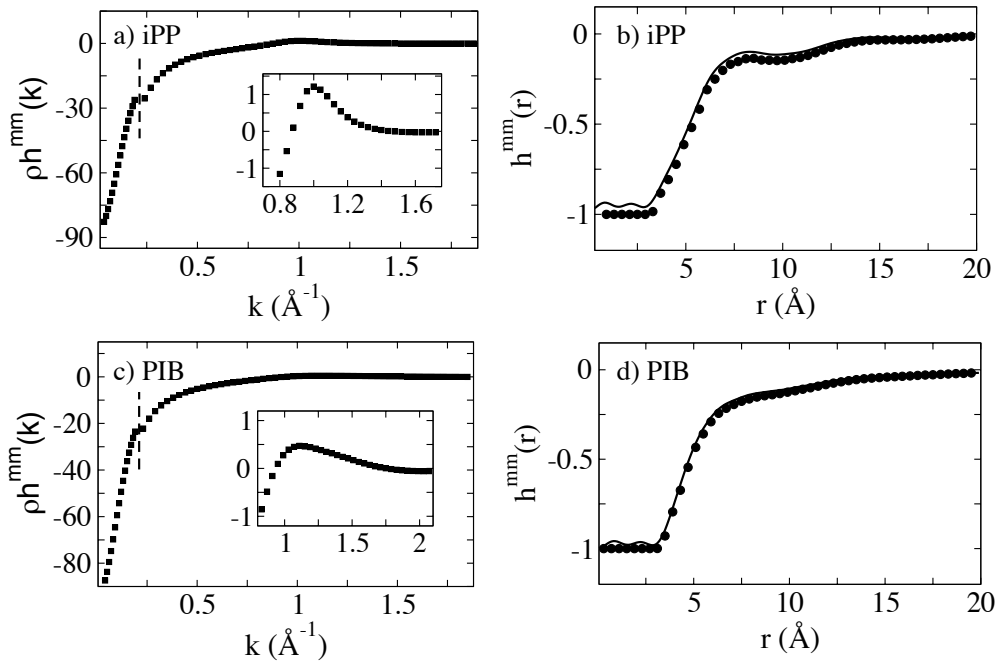


FIGURE VI.4. Left: Plot of the total correlation function, $h^{mm}(k)$, for polymer melts of (a) iPP and (c) PIB, obtained by combining mesoscale and UA MD simulations. Mesoscale simulation depicts $h^{mm}(k)$ over the small k range whereas UA simulation provides data over the large k range. The dashed line indicates the point at which the two simulations were combined. The inset depicts the local peak. Right: Plot of the related $h^{mm}(r)$, the total correlation function in real space, for polymer melts of (b) iPP and (d) PIB. The solid line depicts $h^{mm}(r)$ calculated using our multiscaling approach and the open circles represent data points from UA MD simulations.

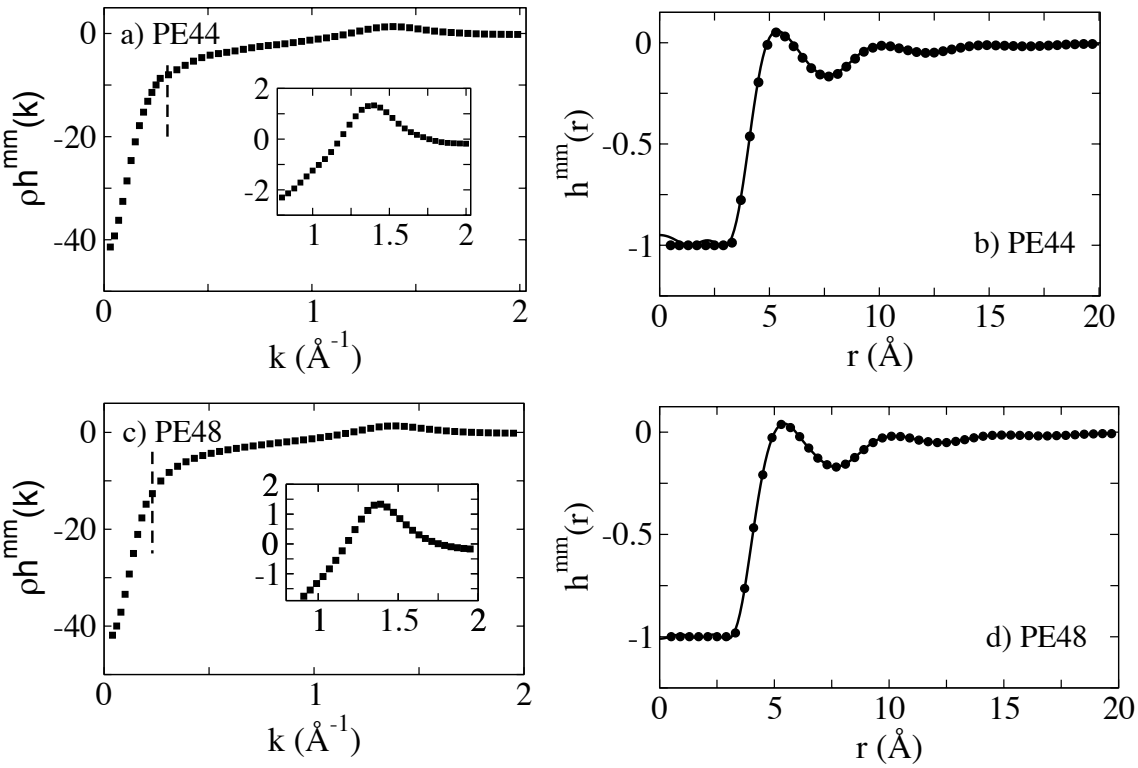


FIGURE VI.5. Left: Plot of the total correlation function, $h^{mm}(k)$, for polyethylene of varying chain length, (a) PE44 ($T = 400$K), (c) PE48 ($T = 448$K) obtained by our multiscale modeling approach of combining mesoscale and UA MD simulations. The inset depicts the local peak. Right: Plot of $h^{mm}(r)$, the total correlation function for different PE chains. The solid line depicts $h^{mm}(r)$ calculated using our multiscaling approach and the open circles represent data points from UA MD simulations.

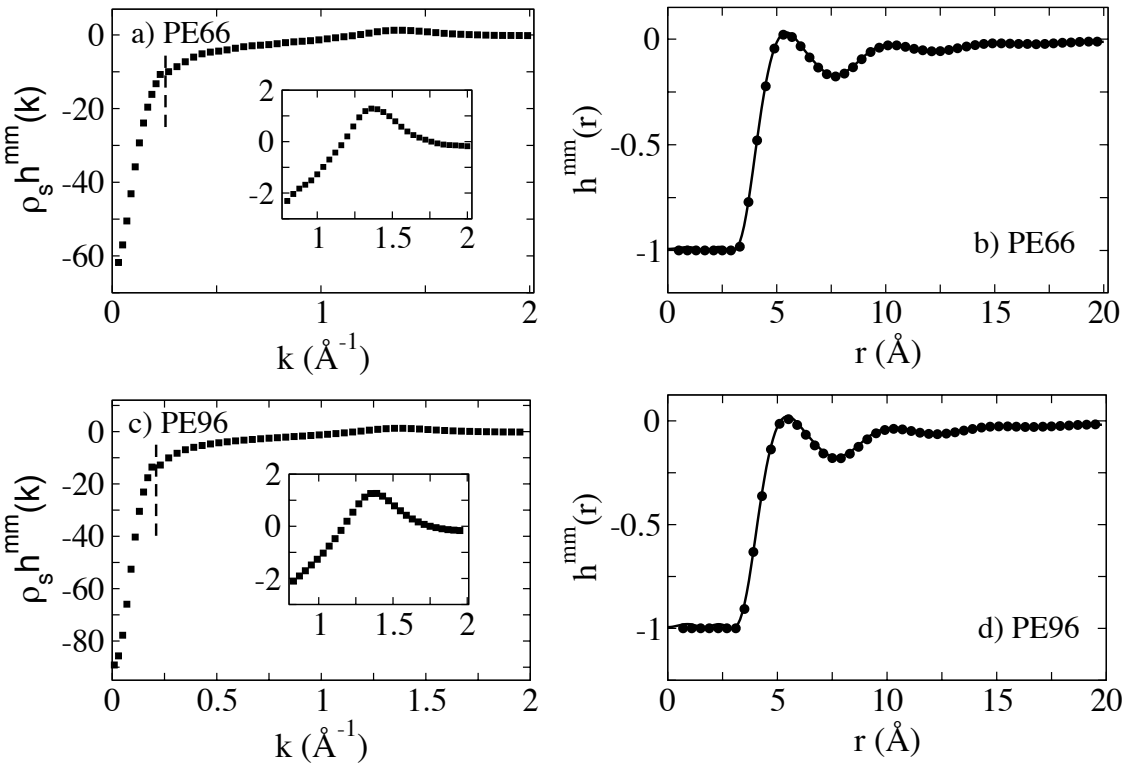


FIGURE VI.6. Left: Plot of the total correlation function, $h^{mm}(k)$, for polyethylene of varying chain length, (a) PE66 ($T = 448$K), (c) PE96 ($T = 448$K) obtained by our multiscale modeling approach of combining mesoscale and UA MD simulations. The inset depicts the local peak. Right: Plot of $h^{mm}(r)$, the total correlation function for different PE chains. The solid line depicts $h^{mm}(r)$ calculated using our multiscaling approach and the open circles represent data points from UA MD simulations.

which defines the resolution of the transformed function. Since we are combining two separate data sets, $\Delta k$ must be large enough so that the Fourier transform is not affected by the small discontinuity at the point of intersection. As long as the interval of the discontinuity is of the same order as that of the sampling step there is no effect on the Fourier transform.

The calculated values for $h^{mm}(r)$ using our multiscaling approach (solid line) are presented along with data from the full UA MD simulations (symbols). The proposed method gives results in good agreement with the full UA simulation data and correctly captures all of the relevant structural features of the liquid, including solvation shells and the correlation hole observed in polymers.

The local chain structure, at large-$k$, is represented by the peak in the insets of Figures VI.3-VI.6, which has a shape that depends on the monomeric structure as well as on the thermodynamic parameters of density and temperature, as the local chain packing is affected by those quantities. Figure. VI.7 shows superimposed the local peaks for polyethylene chains with increasing degree of polymerization at constant temperature of 448 K. Because the chains have the same monomeric structure, and the thermodynamic parameters for each sample are close in value, the local peaks superimpose. This leads to a further computational gain for the multiscale procedure, with respect to performing the full UA-MD simulation. Because the local properties are largely independent on the global scale properties for samples with long polymer chains, the multiscale procedure allows one to obtain the local scale properties for all samples just from one local UA-MD, which can be performed on a melt of short polymer chains, $N \approx 30$.

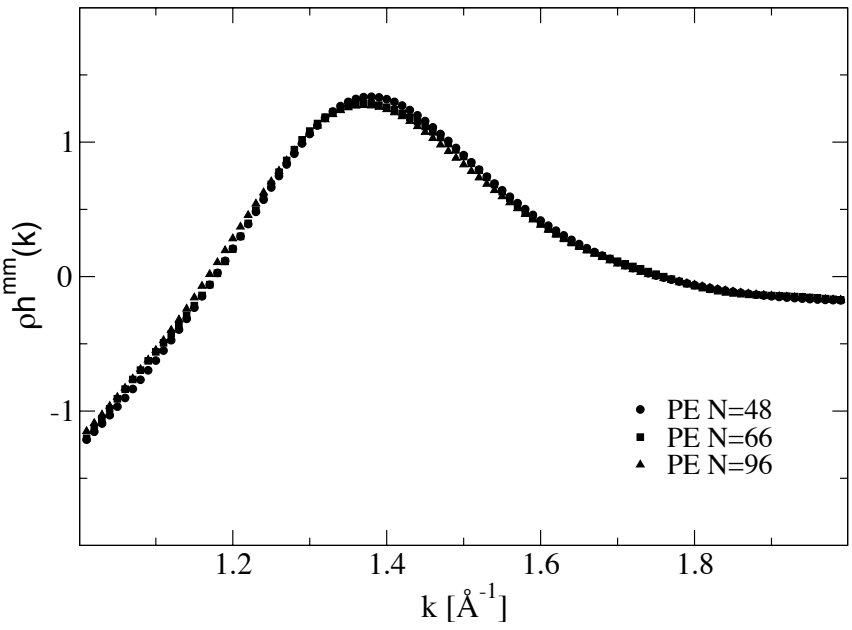


FIGURE VI.7. Plot of the local peak for the total correlation function, $h^{mm}(k)$, for polymer melts of PE at increasing degree of polymerization, ($N = 48, 66, 96$) from local UA simulations at T=448 K

## VI.3. Determining the Crossover Limit

Since the mesoscale simulation only captures global properties, it is necessary to determine the length at which local, intramolecular effects become significant and cannot any longer be discarded. This defines the crossover lengthscale for the UA simulation at which data from UA-MD and MS-MD simulations are combined.

The extent to which intramolecular effects remain important on large lengthscales depends on the length of the polymer and its flexibility. If the length of the polymer is constant, stiffer polymers span a larger volume and therefore have a higher (lower) number of inter- (intra)molecular contacts than their more flexible counterparts. Furthermore, longer chains of polymers with identical chemical structure have a higher statistical number of interpenetrating molecules and a higher (lower) number of inter- (intra)molecular contacts than shorter chains. The iPP and PIB samples presented here are characterized by efficient intramolecular packing, which is due to the particular monomeric structure: for these chains intramolecular interactions are dominant over intermolecular ones for an extended range of lengthscales.

The extent of intramolecular packing is quantified by calculating the ratio between the number of *intra* and *total* site/site contacts at a fixed radial distance, $r$,

$$f_s(r) = \frac{N_s(r)}{N_{total}(r)} \tag{VI.2}$$

where $N_s(r)$ is the number of intramolecular contact sites defined as

$$N_s(r) = 4\pi\rho \int_0^r r'^2 \omega^{mm}(r')\, dr' \ . \tag{VI.3}$$

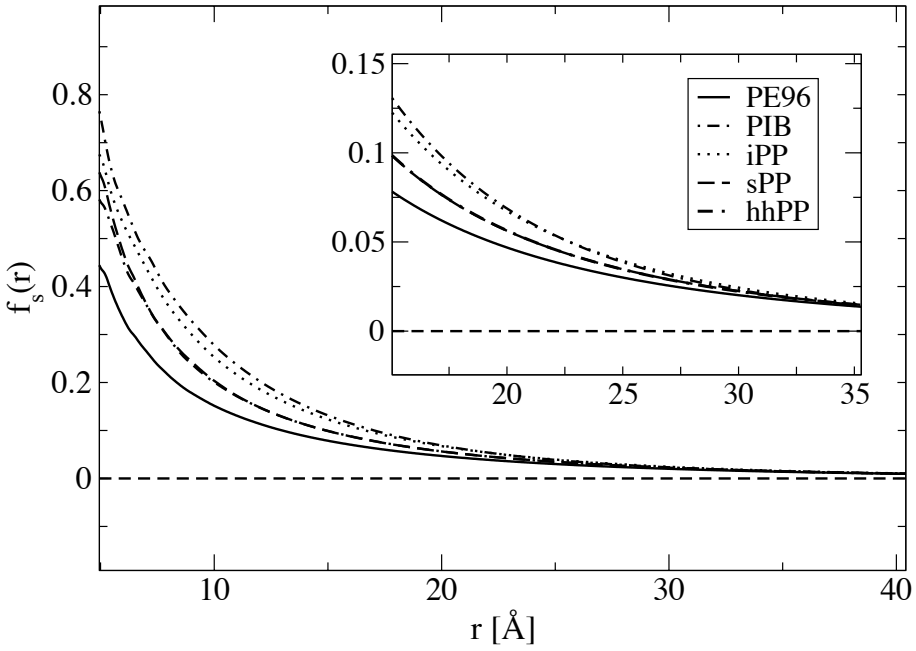


FIGURE VI.8. Fraction of intramolecular contacts, $f_s(r)$, for melts of polymers with different monomer architectures

The total number of sites in a given volume, $N_{total}(r)$, is given by

$$N_{total}(r) = \frac{4}{3}\pi\rho\, r^3\,. \tag{VI.4}$$

Figure VI.8 shows $f_s(r)$ vs. $r(\mathring{A})$ for different monomer architectures. As expected, iPP (dotted line) and PIB (dot-dashed line) show higher values of $f_s(r)$, whereas the stiffest molecule, PE (solid line), exhibits the lowest value at a given radius.

The crossover distance, at which the UA-MD ceases to provide relevant information on the local scale, is determined from the chosen value of the fraction of intramolecular contacts. In all the calculations reported in this chapter, we adopted a value of $f_s(r) = 0.025$ for determining the crossover length.

The value of $f_s(r) = 0.025$ is reached for a distance $r$ that is polymer dependent. The number of polymer chains statistically comprised in the volume spanned by $r$ defines an average number of chains, $n$, that we need to consider in a local UA-MD simulation to produce good statistical information. This number can be calculated from Equation VI.4 using the crossover radius and dividing the number of particles so obtained by the number of $CH_x$, with $x = 0, 1, 2, 3$, units contained in a single chain. The number of sites, $N_{UA}$, and the number of polymer chains, $n$, contained in the volume defined by the given radius of intramolecular interactions, calculated for value of $f_s(r) = 0.025$, as well as for $f_s(r) = 0.05$, are presented in Table VI.1.

The number of chains $n$ is also the statistical number of macromolecules that need to be considered in a local UA-MD simulation and is of the order of the number of chains interpenetrating a "tagged" polymer, $\sqrt{N}$. This number of chains is one order of magnitude smaller than the number of molecules commonly used in the full UA simulations of polymer melts.

TABLE VI.1. Total Number of Sites ($N_{sites}$) and Number of Molecules ($n$) included in a spherical volume of radius $r$, evaluated for $f_s(r) = 0.025$ and 0.05

| System | $N_{sites}(0.025)$ | $n(0.025)$ | $N_{sites}(0.05)$ | $n(0.05)$ |
|---|---|---|---|---|
| PE96 | 2785 | 29 | 995 | 10 |
| sPP | 3547 | 37 | 1412 | 15 |
| hhPP | 3518 | 37 | 1511 | 16 |
| iPP | 3931 | 41 | 1758 | 18 |
| PIB | 3729 | 39 | 1749 | 18 |

## VI.4. Multiscale Modeling of Polymer Blends

The extension of the multiscale modeling procedure to polymer blends is straightforward and requires only keeping tract of the three distinct distributions,

$h_{AA}(r)$, $h_{BB}(r)$, and $h_{AB}(r)$. Again the monomer-monomer correlation function, $h^{mm}(k)$ from the coarse-grained correlation function, $h^{cc}(k)$, is obtained by inverse mapping, using the reciprocal relation:

$$h^{mm}(k) = \left[ \frac{\omega^{mm}_{\alpha\alpha}(k)\omega^{mm}_{\beta\beta}(k)}{\omega^{cm}_{\alpha\alpha}(k)\omega^{cm}_{\beta\beta}(k)} \right] h^{cc}(k) \tag{VI.5}$$

where $h^{cc}(k)$ is obtained from the mesoscale simulation, and the intramolecular form factors, $\omega(k)$, are calculated directly from short UA MD simulations and $\alpha$ and $\beta$ distinguish between polymer chains A and B. Once again, $h^{mm}(k)$ is valid only for small k values, and begins to diverge as $\omega^{cm}(k)$ approaches zero at large k. We performed simulations of a variety of polymer blends under the conditions given in Chapter VII, Table VII.1. Mesoscale simulations provide the center-of-mass total correlation functions that describe the polymer mixtures on the large scale and are readily calculated from the simulation coordinates. As an example we show in Figure VI.9 the plot of $h^{cc}_{AA}(k)$ for a 50:50 mixture of hhPP/sPP ($\chi = 0$). Data from mesoscale simulations and theoretical predictions are compared against united atom simulations for the center-of-mass total correlation functions and show an excellent agreement. Analytical theory, mesoscale simulations, and united atom simulations are all consistent in depicting the structure of the fluid on the lengthscale of the polymer radius of gyration and larger.

As above, the local scale distributions are combined with the renormalized distributions from the coarse-grained simulations in Fourier space at a distance defined by $f_s(r) = 0.025$. The method gives a systematic way of merging simulations to optimize the tradeoff between the gain in accuracy due to inclusion of UA simulation data and the gain in efficiency due to the coarse grained mesoscopic picture. This procedure works well as it yields total correlation functions in excellent

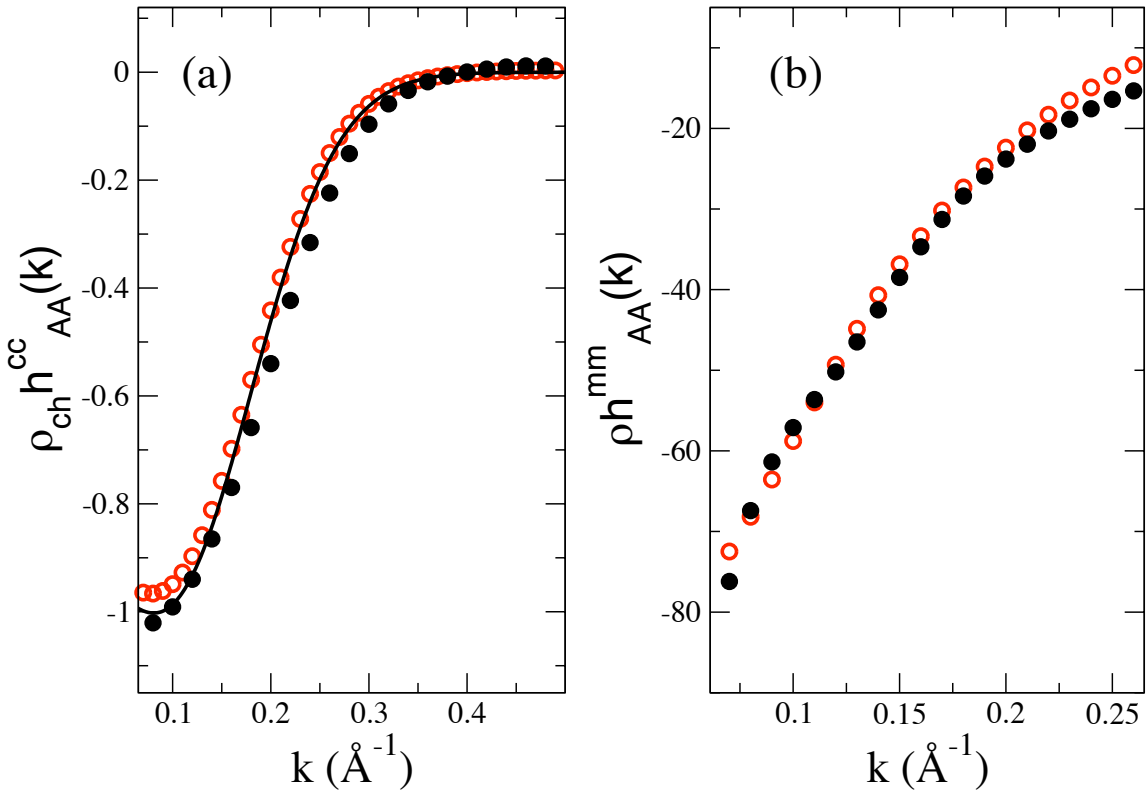


FIGURE VI.9. (a) Plot of $h^{cc}_{AA}(k)$ for hhPP/sPP obtained from mesoscale simulation (open red circles). Comparison with UA data (filled circles) and theoretical predictions (solid line) shows quantitative agreement. (b) Plot of $h^{mm}_{AA}(k)$ calculated using the inverse mapping procedure, Equation VI.5, (open red circles) compared to data from the full UA MD simulation (solid circle).

agreement with UA simulations at a reduced computational cost.

As a representative example, Figure VI.10 illustrates the spirit of our multi-scale modeling approach in which independent simulations representing the same system at different levels of coarse-graining can be combined to provide a complete description of the polymer. Analogous plots for the hhPP/PE and the PIB/PE mixture are reported in our published manuscript.[86]

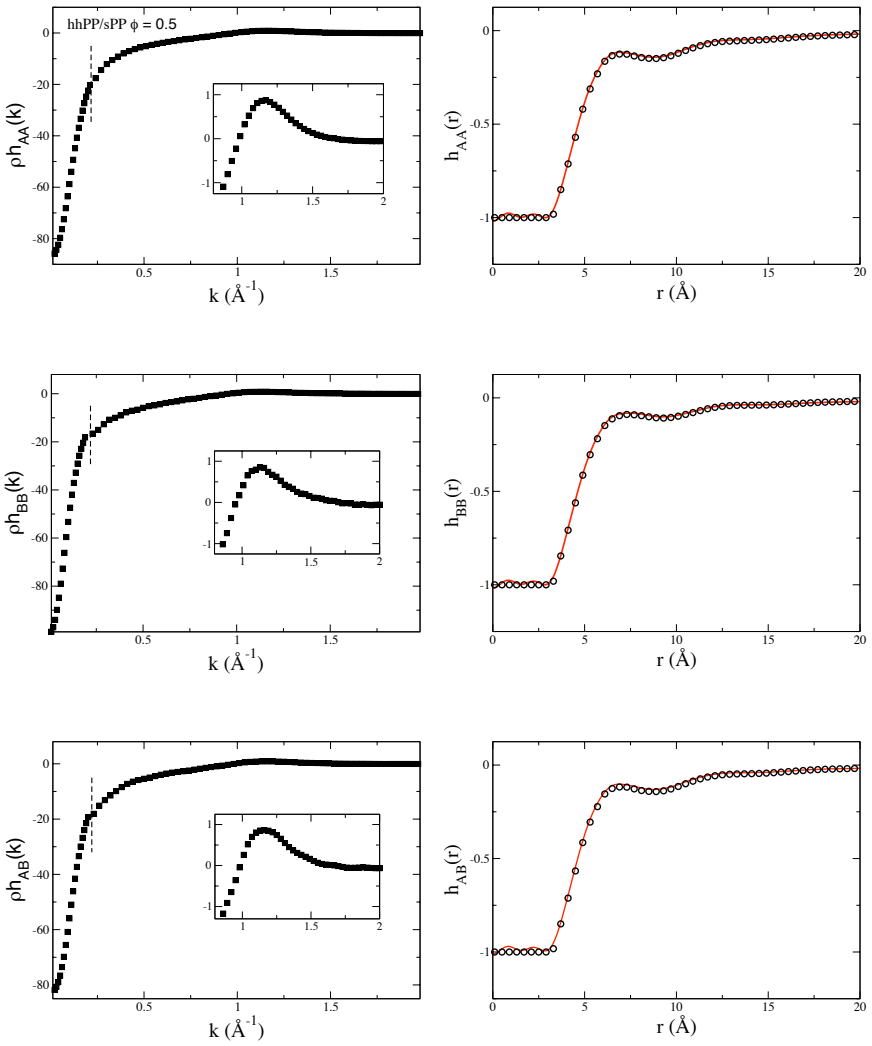


FIGURE VI.10. (Left) Multiscale modeling: The left panels show the total correlation function, $h^{mm}(k)$, for AA (top), BB (middle), and AB (bottom) interactions, for a mixture of 50:50 hhPP/sPP. The data over the range of small k values was obtained by mesoscale simulation, whereas over the large k range it was obtained by UA MD simulation. The inset depicts the local structure. The dashed line indicates the value at which the two simulations were combined. (Right) The correlation function, $h^{mm}(r)$, after Fourier transform (solid red line) is compared with results from the full UA MD simulation (open symbols).

All systems in real space show quantitative agreement with UA-MD data but are obtained at a much more efficient computational time than running the full UA MD simulation. The approach for studying blends is particularly suited for extrapolating

the small $k$ limit when $\chi \neq 0$.

### VI.5. Thermal Blends

To assess the changes in structure that result from increased fluctuation, the monomer level partial static structure factors can be calculated from the total correlation function, $h^{mm}(k)$,

$$\begin{aligned} S^{mm}_{AA}(k) &= \phi\omega^{mm}_{AA}(k) + \rho\phi^2 h^{mm}_{AA}(k) \ , \\ S^{mm}_{BB}(k) &= (1-\phi)\omega^{mm}_{BB}(k) + \rho(1-\phi)^2 h^{mm}_{BB}(k) \ , \\ S^{mm}_{AB}(k) &= \rho\phi(1-\phi) h^{mm}_{AB}(k) \ , \end{aligned} \tag{VI.6}$$

where the monomer form factors were determined from UA simulations as in Equation VI.5 above and $\phi$ is the volume fraction of polymer chain A. The structure factor measuring correlations in the relative concentration, $S^{\phi\phi}(k)$, which diverges as the mixture approaches the spinodal, is expressed as a linear combination of these partial structure factors,

$$S^{\phi\phi}(k) = (1-\phi)^2 S^{mm}_{AA}(k) + \phi^2 S^{mm}_{BB}(k) - 2\phi(1-\phi) S^{mm}_{AB}(k). \tag{VI.7}$$

In small angle neutron scattering (SANS) experiments, the $\chi$ parameter is determined from fitting the partial structure factor to the random phase approximation (RPA) equation of de Gennes[3]

$$\frac{1}{S(k)} = \frac{1}{\phi\omega^{mm}_{AA}(k)} + \frac{1}{(1-\phi)\omega^{mm}_{BB}(k)} - 2\chi, \tag{VI.8}$$

where for convenience the monomer site volumes were set equal to one.

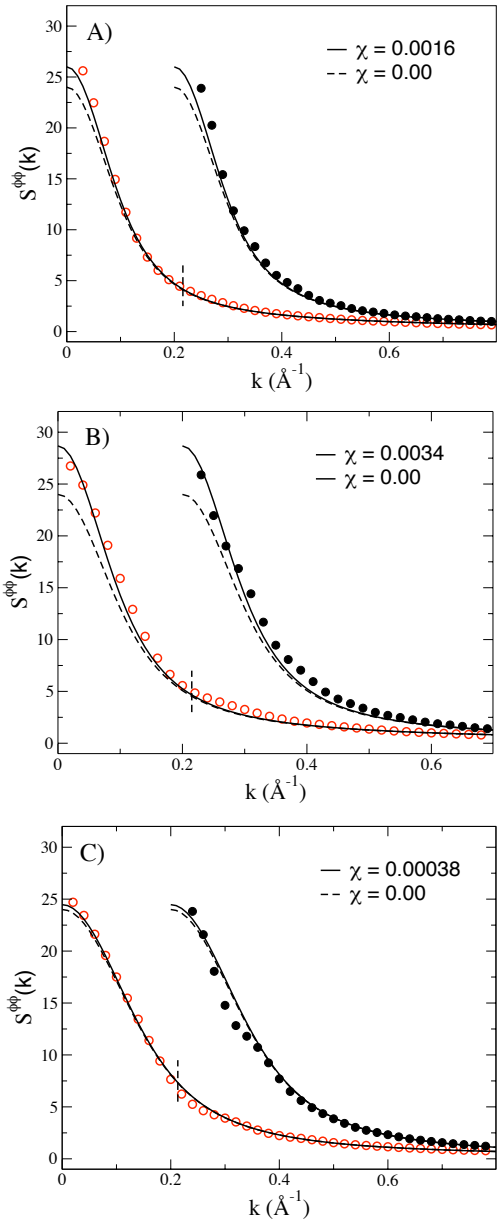


FIGURE VI.11. (A) The concentration fluctuation structure factor obtained from the multiscale modeling procedure (open circles) for hhPP/PE ($\phi = 0.5$) at $T = 453K$. For comparison the RPA equation evaluated at $\chi = 0.0016$ (solid line) and $\chi = 0.00$ (dashed line) is shown. The inset shows the structure factor from the full UA simulation. (B) The same as part (A), except for PIB/PE ($\phi = 0.5$), for which the RPA equation, evaluated at $\chi = 0.0034$ (solid line) and $\chi = 0.00$ (dashed line), is shown. (C) the same except for the hhPP/PIB blend, and the RPA equation is evaluated at $\chi = 0.00038$ (solid line) and $\chi = 0.00$ (dashed line).

Figure VI.11 presents $S^{\phi\phi}(k)$ for the three different thermal blends obtained from our multiscale modeling procedure. The static structure factor calculated in this manner exhibits good agreement when compared to the RPA equation, which was evaluated at $\chi = 0.0016$ for hhPP/PE, $\chi = 0.0034$ for PIB/PE, and $\chi = 3.8 \times 10^{-4}$ for hhPP/PIB, using the intramolecular form factors from UA MD simulations. Comparison to the RPA equation demonstrates that our approach captures the fluctuations in concentration that arise in thermal polymer mixtures even at the relatively high temperatures of these simulations. The advantage of a multiscale approach is exhibited by Figure VI.11 since the low wave vector regime is determined by mesoscale simulations so that UA simulations only need to be performed on systems at length scales up to the cut-off length (dashed line). This is important since only the initial stages of the divergent behavior need to be captured by united atom simulations, thus the need for prohibitively large simulation boxes is circumvented. For comparison, $S(k)$, calculated for the full UA MD simulation is also shown (offset for clarity) and agrees with our multiscale results, demonstrating the consistency between the two approaches.

The number of particles in the soft sphere representation are presented in Table VI.2. Since each of these particles represents an entire polymer chain, many more polymers can be simulated with reasonable efficiency as compared to an all atom simulation. This means that large scale fluctuations are much more readily calculated in a coarse-grained picture.

## VI.6. Conclusion

Chapter VI has presented an application of the coarse-grained method in a multiscale modeling procedure. The structural distributions in the coarse-grained

simulation are renormalized by the inverse of the relationship to derive them. This "inverse mapping" allows one to calculate monomer distributions from the coarse-grained simulations; however these distributions are only relevant on length scales larger than the polymer radius of gyration. Hence, one also performs united atom simulation of the same chain to obtain the local structure and then combines the two distributions in Fourier space at a crossover regime specified above. The total monomer distribution is then calculated from numerical Fourier transform of the total correlation function. This chapter has also presented an application of this procedure to polymer blends which are the sole topic of the next chapter.

TABLE VI.2. Mesoscale Simulation (MS-MD) Particle Number and Box Dimension Compared to UA Box Dimension. All UA simulations are for 1600 chains.

| Blend [A/B] | Particles | $L_{MS}$ [$\mathring{A}$] | $L_{UA}$ [$\mathring{A}$] |
|---|---|---|---|
| hhPP/sPP | 2744 | 199.07 | 166.61 |
| hhPP/PE | 5324 | 246.21 | 166.61 |
| PIB/PE | 4096 | 218.66 | 164.91 |
| PIB/sPP | 5488 | 245.19 | 164.91 |
| iPP/PE | 1728 | 168.57 | 167.27 |
| hhPP/PIB | 3456 | 230.73 | 164.91 |

# CHAPTER VII

# EFFECTIVE SOFT-CORE POTENTIALS AND MESOSCOPIC SIMULATIONS OF BINARY POLYMER MIXTURES

Chapter VII presents a discussion of the analytical coarse-graining procedure extended to blends. Here we focus only on the Gaussian thread model results as derived previously by Yatsenko and Guenza.[38,39] This chapter shows that the mesoscale simulations performed using the effective potential can describe the entire phase diagram of a polymer blend and provide a method of performing simulations of systems with increasing critical fluctuations. This work resulted in a paper co-authored with I. Lyubimov and M. G. Guenza entitled "Effective Soft-Core Potentials and Mesoscopic Simulations of Binary Polymer Mixtures".[87]

United atom molecular dynamics simulation trajectories are a courtesy of G. S. Grest, J. G. Curro, and E. Jaramillo from Sandia National Laboratories.

## VII.1. Introduction

The mixing of two or more types of polymers is of great scientific and technological interest, as it opens up the possibility of creating new materials emerging with specific physical and chemical properties.[5] However, although polymer blends have been very much a part of everyday life, these continue to be a source of extensive scientific inquiry. The rich physics in polymer mixtures stems in part from the fact that their structure and dynamics change as thermodynamic conditions that cause phase separation (i.e. spinodal decomposition) are approached. Mixture stability is not only driven by temperature and composition, but also by differences in chain length and monomer architecture that may contribute substantial entropic

effects. From physical and engineering standpoints, a goal is to understand and predict changes that a polymer will undergo when mixed with another polymer system.[88,89]

In this chapter, we focus on performing molecular dynamics simulations of polymer mixtures where the ensemble of polymers is mapped onto a system of interacting soft particles, i.e. the soft-sphere limit. The advantage of this extreme coarse-graining of the polymer is that it is possible to simulate very large ensembles of particles, i.e. adopt large simulation boxes, with a modest increase in the computational time. Such an extreme level of coarse-graining becomes particularly important for simulations of systems where the relevant range of length scales is particularly large, for example in micellar aggregates of ionic surfactants.[90]

The chapter discusses the procedure to obtain the coarse-grained potential for a mixture of polymers starting from liquid state theory and solving the Ornstein-Zernike equation.[38,39] The potential obtained in such a manner is explicitly related to the structural parameters of the polymer, making it specific to any system we desire to simulate, but also fully transferable to systems with different molecular structure and thermodynamic conditions. More specifically, non-phenomenological expressions for the com-com total pair intermolecular correlation functions, $h^{cc}_{\alpha\beta}(r)$, between self ($\alpha\alpha$) and cross ($\alpha\beta$) interactions, are obtained for binary polymer mixtures where atomistic sites are accounted for as real sites, while coarse-grained sites are treated as auxiliary sites. The equation formally bridges information from the microscopic (monomer) domain to mesoscopic (molecular) scales. The derived equations for $h^{cc}_{\alpha\beta}(r)$ reproduce well and with no fitting parameters united atom (UA) molecular dynamics (MD) simulation data in both real and reciprocal spaces.

Systems investigated are blends of polyethylene, polyisobutylene, as well as

polypropylenes in their head-to-head, istotactic, as well as syndiotactic forms. While the focus here is on static properties, the derived potential is widely applicable to non-equillibrium systems, and may be useful in other methods commonly employed, such as dissipative particle dynamics,[91] which currently rely on numerical potentials.

The temperature dependence of the effective potential is expressed in terms of the single interaction parameter, $\chi$, that enters through the analytical form of the potential and depends on the local interactions between monomers. It is demonstrated that the proposed theory may be applied to a variety of including the case where the mixture exhibits a Lower Solution Critical Temperature (LSCT).

## VII.2. Mesoscopic Pair Correlation Functions for Asymmetric Binary Polymer Blends

Our model for a binary blend consists of $A$ and $B$ homopolymers, having $N_A$ and $N_B$ monomer sites with segment lengths $\sigma_A$ and $\sigma_B$, respectively. For simplicity, these monomer sites are taken to span equivalent volumes so that the polymer volume fraction is given by $\phi = n_A N_A/(n_A N_A + n_B N_B)$, where $n_\alpha$ is the number of molecules of type $\alpha$ in the mixture with $\alpha \in \{A, B\}$. While $\rho = (n_A N_A + n_B N_B)/V$ quantifies the total number of monomer sites contained in a region of space spanned by $V$, the site and chain number densities for molecules of type A are given by $\rho_A = n_A N_A/V = \phi\rho$ and $\rho_{c,A} = n_A/V$, respectively.

The derivation of the total intermolecular correlation function in a polymer mixture was derived in the Gaussian thread limit by Yatsenko, et. al.[38,39] The key step is to include the center of mass sites as *auxiliary* sites, along with monomer sites

in a generalized Ornstein-Zernike integral equation of the form,

$$\mathbf{H}(k) = \mathbf{\Omega}(k)\mathbf{C}(k)\left[\mathbf{\Omega}(k) + \mathbf{H}(k)\right] , \tag{VII.1}$$

where $\mathbf{H}(k)$ is the matrix of total intermolecular pair correlation functions (pcfs), $\mathbf{C}(k)$ is the matrix of direct intermolecular pcfs, and $\mathbf{\Omega}(k)$ represents the matrix of intramolecular pcfs. Specializing to the case of a binary polymer mixture, each matrix in Equation VII.1 is of rank four, composed of four $2 \times 2$ blocks that account for monomer-monomer ($mm$), com-com ($cc$), and the corresponding cross ($cm$ and $mc$) interactions. For instance,

$$\mathbf{H}(k) = \begin{bmatrix} \mathbf{H}^{mm}(k) & \mathbf{H}^{mc}(k) \\ \mathbf{H}^{cm}(k) & \mathbf{H}^{cc}(k) \end{bmatrix} . \tag{VII.2}$$

The remaining matrices in Equation VII.1 follow an arrangement analogous to that of Equation VII.2. Each block in Equation VII.2 contains self ($\alpha\alpha$) interactions along its diagonal, whereas cross ($\alpha\beta$) interactions occupy off-diagonal positions.

As a next step, the individual block elements that define the matrices in Equation VII.1 are defined. The intermolecular total pcf matrix $\mathbf{H}(k)$ is composed of the chain-averaged monomer-monomer pcfs $H^{mm}_{\alpha\beta}(k) = \rho_\alpha \rho_\beta h^{mm}_{\alpha\beta}(k)$, the com-monomer pcfs $H^{cm}_{\alpha\beta}(k) = \rho_{c,\alpha}\rho_\beta h^{cm}_{\alpha\beta}(k) = H^{mc}_{\beta\alpha}(k)$, and com-com pcf $H^{cc}_{\alpha\beta}(k) = \rho_{c,\alpha}\rho_{c,\beta}h_{\alpha\beta}(k)$. Note that in general, $h^{cm}_{\alpha\beta}(k) = h^{mc}_{\beta\alpha}(k)$ while $h^{cm}_{\alpha\beta}(k) \neq h^{mc}_{\alpha\beta}(k)$ when $\alpha \neq \beta$. The intramolecular pcf matrix $\mathbf{\Omega}(k)$ is similarly composed of $\Omega^{mm}_{\alpha\beta}(k) = \rho_\alpha\rho_\beta\omega^{mm}_{\alpha\beta}(k)\delta_{\alpha\beta}z_{\alpha\beta}$, $\Omega^{cm}_{\alpha\beta}(k) = \rho_{c,\alpha}\rho_\beta\omega^{cm}_{\alpha\beta}(k)\delta_{\alpha\beta}z_{\alpha\beta} = \Omega^{mc}_{\beta\alpha}(k)$, and $\Omega^{cc}_{\alpha\beta}(k) = \rho_{c,\alpha}N_\beta\rho_{c,\beta}\delta_{\alpha\beta}z_{\alpha\beta}$, where $z_{\alpha\beta} = [\phi_\beta\rho(2-\delta_{\alpha\beta})]^{-1}$. Under the assumption that the direct correlation between fictitious sites can be neglected, the only non-

zero block in $\mathbf{C}(k)$ involves monomer-monomer pcfs, defined as $C^{mm}_{\alpha\beta}(k) = c^{mm}_{\alpha\beta}(k)$.

Using the matrix definitions described above, Equation VII.1 is solved to obtain the intermolecular mesoscopic total pcfs, which are given by the relation

$$h^{cc}_{\alpha\beta}(k) = \left[\frac{\omega^{cm}_{\alpha\alpha}(k)\omega^{cm}_{\beta\beta}(k)}{\omega^{mm}_{\alpha\alpha}(k)\omega^{mm}_{\beta\beta}(k)}\right] h^{mm}_{\alpha\beta}(k)\,. \tag{VII.3}$$

Upon inspection, it is readily seen that Equation VII.3 formally connects com distribution functions to monomer-monomer intra- and intermolecular distribution functions. In this manner, one calculates mesoscale properties from information on the local polymer scale. As mentioned before, this feature is relevant because properties on the mesoscale ultimately depend on small-scale interactions.

To obtain analytical solutions for $h^{cc}_{\alpha\beta}(k)$, a brief description is given for each of the correlation functions entering into Equation VII.3. The com-monomer intramolecular pcf can be approximated in reciprocal space with a Gaussian distribution as

$$\omega^{cm}_{\alpha\alpha}(k) = N_\alpha e^{-k^2 R^2_{g\alpha}/6}\,, \tag{VII.4}$$

with the molecular radius of gyration defined as $R_{g\alpha} = (N/6)^{1/2}\sigma_\alpha$. On the other hand, the monomer-monomer intramolecular pcf is given by the Debye formula,

$$\omega^{mm}_{\alpha\alpha}(k) = \frac{2N_\alpha\left[e^{-k^2R^2_{g\alpha}} - 1 + k^2R^2_{g\alpha}\right]}{k^4R^4_{g\alpha}}\,. \tag{VII.5}$$

For analytical convenience, however, it is costumary to approximate Equation VII.5 with its Padé approximant given by[16]

$$\omega^{mm}_{\alpha\alpha}(k) \approx \frac{N_\alpha}{1 + k^2R^2_{g\alpha}/2}\,. \tag{VII.6}$$

Although approximated, inclusion of Equation VII.6 allows for a convenient analytic expression for $h^{cc}(r)$ given below by Equation VII.9, which has been shown to give good agreement with simulations for the total pair correlation function in both real and reciprocal spaces.[38] In the current chapter, we use both Equation VII.5 and Equation VII.6 for $\omega^{mm}(k)$, and compare the resulting mesoscopic $h^{cc}(k)$ from Equation VII.3.

The respective monomer-monomer intermolecular total pcfs used are taken from the thread limit of the Polymer Reference Interaction Site Model[14,15] (PRISM). The initial analytical treatment in the context of PRISM for polymer mixtures[92] is extended to account for chain asymmetry effects in the system. In this approach, a new parameter enters the formalism, $\gamma = \sigma_B/\sigma_A$, which defines the monomer asymmetry.

While the thread model for polymer chains coarsely describes the liquid structure on local scales, it accurately captures the onset of the "correlation hole" effect at a length scale of $R_g$. Given that the spatial dimension of interest in our description is $R_g$, the thread limit of PRISM is an adequate representation for the intended purpose of the present work. The solutions are given by[38,39]

$$\begin{aligned} h^{mm}_{AA}(r) &= \frac{3}{\pi\rho r\sigma^2_{AB}}\left[\frac{1-\phi}{\phi}e^{-r/\xi_\phi} + \gamma^2 e^{-r/\xi_{\rho_{AA}}} - \frac{1}{\phi}\frac{\sigma^2_{AB}}{\sigma^2_A}e^{-r/\xi_{cA}}\right], \\ h^{mm}_{BB}(r) &= \frac{3}{\pi\rho r\sigma^2_{AB}}\left[\frac{\phi}{1-\phi}e^{-r/\xi_\phi} + \gamma^{-2} e^{-r/\xi_{\rho_{BB}}} - \frac{1}{1-\phi}\frac{\sigma^2_{AB}}{\sigma^2_B}e^{-r/\xi_{cB}}\right], \\ h^{mm}_{AB}(r) &= \frac{3}{\pi\rho r\sigma^2_{AB}}\left[-e^{-r/\xi_\phi} + e^{-r/\xi_{\rho_{AB}}}\right], \end{aligned} \tag{VII.7}$$

where

$$\xi_\phi = \frac{\sigma_{AB}}{\sqrt{24\phi(1-\phi)\chi_s(1-\chi/\chi_s)}}, \tag{VII.8}$$

is the length scale governing concentration fluctuations, which diverges at the spinodal temperature. Here, $\chi$ is a single interaction parameter that depends on the specific nearest neighbor pair energies between two AA, AB, or BB monomers, and is given by $\chi = \epsilon_{AB} - (\epsilon_{AA} + \epsilon_{BB})/2$. In a mesoscopic treatment which averages out the specific monomer interactions, $\chi$ is an input parameter corresponding to the temperature dependance of a specific polymer architecture. From our definitions it clear that the quantity $\chi/\rho$ is the analog of the Flory-Huggins interaction parameter, and at the spinodal temperature $\chi \to \chi_s$, where $\chi_s = [2N_A\phi]^{-1} + [2N_B(1-\phi)]^{-1}$. The quantity, $(1-\chi/\chi_s)$ can be seen as a reduced temperature that indicates how far the system is from its spinodal temperature. Also in Equation VII.7, $\xi_{c\alpha} = R_{g\alpha}/2^{1/2}$ is the length scale of the correlation hole while $\xi^{-1}_{\rho\alpha\beta} = \pi\rho\sigma^2_{\alpha\beta}/3 + \xi^{-1}_{c\alpha\beta}$ is the density correlation length scale with $\sigma^2_{\alpha\beta} = \phi_\beta\sigma^2_\alpha + \phi_\alpha\sigma^2_\beta$. This latter definition reintroduces finite-size effects, local semiflexibility, and branching that pertain to each component through a melt-like description. The effective segment length scales are determined from the radius of gyration of each component polymer, through the relation $\sigma_\alpha = (6/N_\alpha)^{1/2} R_g$.

Inserting the definitions from Eqs. (VII.4), (VII.6), and (VII.7) into (VII.3), the intermolecular total pcfs at the com level read

$$\begin{aligned} h^{cc}_{AA}(r) &= \frac{1-\phi}{\phi} I^{\phi}_{AA}(r) + \gamma^2 I^{\rho}_{AA}(r) \ , \\ h^{cc}_{BB}(r) &= \frac{\phi}{1-\phi} I^{\phi}_{BB}(r) + \gamma^{-2} I^{\rho}_{BB}(r) \ , \\ h^{cc}_{AB}(r) &= -I^{\phi}_{AB}(r) + I^{\rho}_{AB}(r) \ , \end{aligned} \tag{VII.9}$$

where $I^{\phi}_{\alpha\beta}(r)$ and $I^{\rho}_{\alpha\beta}(r)$ identify the concentration and density fluctuation contributions, respectively. We introduce here a compact notation with the function

$I^{\lambda}_{\alpha\beta}(r)$ defined as

$$
\begin{aligned}
I^{\lambda}_{\alpha\beta}(r) \;=\; & \\
& \frac{3}{4}\sqrt{\frac{3}{\pi}}\frac{\xi'_{\rho}}{R_{g\alpha\beta}}\vartheta_{\alpha\beta 1}\left(1-\frac{\xi^2_{c\alpha\beta}}{\xi^2_{\lambda}}\right)e^{-3r^2/(4R^2_{g\alpha\beta})}-\frac{1}{2}\frac{\xi'_{\rho}}{r}\vartheta_{\alpha\beta 2}\left(1-\frac{\xi^2_{c\alpha\beta}}{\xi^2_{\lambda}}\right)^2 e^{R^2_{g\alpha\beta}/(3\xi^2_{\lambda})} \\
& \times\left[e^{r/\xi_{\lambda}}\mathrm{erfc}\left(\frac{R_{g\alpha\beta}}{\xi_{\lambda}\sqrt{3}}+\frac{r\sqrt{3}}{2R_{g\alpha\beta}}\right)-e^{-r/\xi_{\lambda}}\mathrm{erfc}\left(\frac{R_{g\alpha\beta}}{\xi_{\lambda}\sqrt{3}}-\frac{r\sqrt{3}}{2R_{g\alpha\beta}}\right)\right] \qquad \text{(VII.10)}
\end{aligned}
$$

and

$$
\vartheta_{\alpha\beta 1} \;=\; \frac{\left(1-\frac{\xi^2_{c\alpha\alpha}\xi^2_{c\beta\beta}}{\xi^2_{c\alpha\beta}\xi^2_{\lambda}}\right)}{\left(1-\frac{\xi^2_{c\alpha\beta}}{\xi^2_{\lambda}}\right)}, \qquad \text{(VII.11)}
$$

$$
\vartheta_{\alpha\beta 2} \;=\; \frac{\left(1-\frac{\xi^2_{c\alpha\alpha}}{\xi^2_{\lambda}}\right)\left(1-\frac{\xi^2_{c\beta\beta}}{\xi^2_{\lambda}}\right)}{\left(1-\frac{\xi^2_{c\alpha\beta}}{\xi^2_{\lambda}}\right)^2}, \qquad \text{(VII.12)}
$$

where $\xi_{\lambda} \in \{\xi_{\phi}, \xi_{\rho}\}$ and $\xi'_{\rho} = 3/(\pi\rho\sigma^2_{AB})$. Radii of gyration in the blend are defined such that $2R^2_{g\alpha\beta} = R^2_{g\alpha} + R^2_{g\beta} = 4\xi^2_{c\alpha\beta}$, with $\xi_{c\alpha\alpha} \equiv \xi_{c\alpha}$.

The development presented here is the required input to the derivation of the effective pair interaction potentials, a topic that will be addressed in the following section.

### VII.3. The Effective Soft Core Potential

Since the fundamental units in our description interact through a soft-core potential, we again use the hypernetted-chain (HNC) closure,

$$
(k_B T)^{-1} v^{cc}_{\alpha\beta}(r) = h^{cc}_{\alpha\beta}(r) - \ln\left[1 + h^{cc}_{\alpha\beta}(r)\right] - c^{cc}_{\alpha\beta}(r)\,, \qquad \text{(VII.13)}
$$

where $c^{cc}_{\alpha\beta}(r)$ is the direct pcf. Taking our system to be a simple liquid comprised by soft colloidal particles, the direct pair correlation functions are defined by

$$\begin{aligned} c^{cc}_{\alpha\alpha}(k) &= \frac{1}{\rho_{c,\alpha}} - \frac{S^{cc}_{\beta\beta}(k)}{(\rho_{c,\alpha}+\rho_{c,\beta})\,|\mathbf{S}_{cc}(k)|}\ , \\ c^{cc}_{\alpha\beta}(k) &= \frac{S^{cc}_{\alpha\beta}(k)}{(\rho_{c,\alpha}+\rho_{c,\beta})\,|\mathbf{S}_{cc}(k)|}\ , \end{aligned} \tag{VII.14}$$

where $S^{cc}_{\beta\beta}$ and $S^{cc}_{\alpha\beta}$ are the static structure factors for a binary mixture, and $|\mathbf{S}_{cc}(k)| = S^{cc}_{AA}(k)S^{cc}_{BB}(k) - [S^{cc}_{AB}(k)]^2$ is the determinant of the mesoscopic static structure factor matrix. For a binary mixture these static structure factors are given by

$$\begin{aligned} S_{AA}(k) &= \phi + \phi^2\rho_{ch}h^{cc}_{AA}(k)\ , \\ S_{BB}(k) &= 1-\phi+(1-\phi)^2\rho_{ch}h^{cc}_{BB}(k)\ , \\ S_{AB}(k) &= \phi(1-\phi)\rho_{ch}h^{cc}_{AB}(k)\ , \end{aligned} \tag{VII.15}$$

where the total chain density, $\rho_{ch} = \rho/N$. By inserting Eqs. (VII.9) and (VII.14) into (VII.13), the $v^{cc}_{\alpha\beta}(r)$ are obtained.

The analytical solution presented here represents an advantage to numerically optimized potentials because this approach bypasses the need to perform atomistic simulations for each thermodynamic state point of interest, which is necessary in numerical implementations since the effective pair interaction potentials depend on the state of the system. This can be readily appreciated from the pcfs that enter into the HNC closure, which are themselves state-dependent.

We investigated the effect that the use of the Debye formalism, Equation VII.5, or of its Padé approximant, Equation VII.6, for the monomer form factor in the denominator of Equation VII.3 has on the calculation of the potential. The Padé

approximant is less precise than the Debye equation, but it allows for the analytical solution of the total correlation functions, Equation VII.9. We observe that when Equation VII.6 is used, singular points arise in the low k regime in the solution of Equation VII.14 for $c^{cc}(k)$ as the determinant of the mesoscopic static structure factor, $|\mathbf{S}_{cc}(k)| = S^{cc}_{AA}(k)S^{cc}_{BB}(k) - [S^{cc}_{AB}(k)]^2$, passes through zero. This corresponds to an unphysical region of negative compressibility. When Equation VII.5 is used instead, such singular points do not arise.

For homopolymer melts, it has previously been determined that the singularities in $c^{cc}(k)$ occur as a result of the intrinsic error introduced in Equation VII.6 by the Padé approximation.[66] In order to obtain a usable form of the effective potential from Equation VII.13, we tested two schemes: in scheme 1, we enforced the condition that $c^{cc}(k = 0) \leq c^{cc}(k) \leq 0$ for low k, which effectively eliminates any singularities from the direct correlation function; in scheme 2, we enforced the isothermal compressibility limit, such that for regions where $|\mathbf{S}_{cc}(k)| \leq |\mathbf{S}_{cc}(0)|$, we truncated $h^{cc}(k)$ so that $h^{cc}_{\alpha\beta}(k) = h^{cc}_{\alpha\beta}(k = 0)$. The two schemes are equivalent and give identical results within the precision of our calculation. This is so, because polymer liquids are almost incompressible.

The focus of this chapter is polymer blends of polyethylene (PE), polyisobutylene (PIB), and polypropylenes in their head-to-head (hhPP), isotactic (iPP), and syndiotactic (sPP) forms. The effective pair potential, $v^{cc}(r)$ for interactions of type AA, BB and AB is calculated for the different binary polymer mixtures and for hhPP:PE under different values of $\phi$ and $\chi$ using both the Debye form and Padé form of the intramolecular distribution function (Equation VII.5 and VII.6). As a model calculation of the potential, we present the results for the prototypical hhPP/PE polymer blend in Figure VII.1, which shows how the

potential depends on the reduced temperature $(1 - \chi/\chi_s)$. Input parameters to our theoretical calculations are reported in Table VII.1 as data for the UA simulations against which we test our approach.[?,27] Although there is a noticeable difference in the potential obtained using either Equation VII.5 or VII.6, they are qualitatively similar in many respects. For example, under athermal conditions, the mixture is random and the number of $AB$ contacts is in between those of the self terms, $AA$ and $BB$. Correspondingly, pair interactions accounting for $AB$ contacts must be intermediately repulsive. This effect is reflected in the plot of $v^{cc}_{\alpha\beta}(r)$. The $A$-type (flexible hhPP) particles display the highest repulsive response as a consequence of their stronger correlation hole effect. The inset of Figure VII.1 highlights the change in the repulsive component in the potential, as the ratio, $\chi/\chi_s$, is varied.

TABLE VII.1. Polyolefin blends ($T = 453$ K, $N_A = N_B = 96$)

| Blend$[A/B]$ | $\phi$ | $\rho$ [sites/Å$^3$] | $R_{gA}$ [Å] | $\gamma$ | $\chi$ |
|---|---|---|---|---|---|
| hhPP/PE | 0.50 | 0.0332 | 12.32 | 1.34 | $-0.0294 + 17.58/T$[a,b] |
| PIB/PE | 0.50 | 0.0343 | 9.76 | 1.68 | $0.00257 + 4.99/T$[b] |
| PIB/sPP | 0.50 | 0.0343 | 9.76 | 1.41 | $\cdots$ |
| sPP/PE | 0.50 | 0.0328 | 13.89 | 1.19 | $\cdots$ |
| iPP/PE | 0.25 | 0.0328 | 11.35 | 1.47 | 0.005[c] |
| iPP/PE | 0.75 | 0.0328 | 11.33 | 1.48 | 0.01 [c] |
| hhPP/PIB | 0.50 | 0.0343 | 12.4 | 1.28 | $0.027 - 11.4/T$[b,d,e] |

[a]Reference 94.

[b]Reference 95.

[c]Reference 27.

[d]Reference 28.

[e]Reference 96.

While the full Debye form (Equation VII.5) for the monomer form factor prevents an explicit analytic expression for $h^{cc}(r)$ in the form of Equation VII.9, which was the motivation for adopting the Padé approximation, a numerically obtained

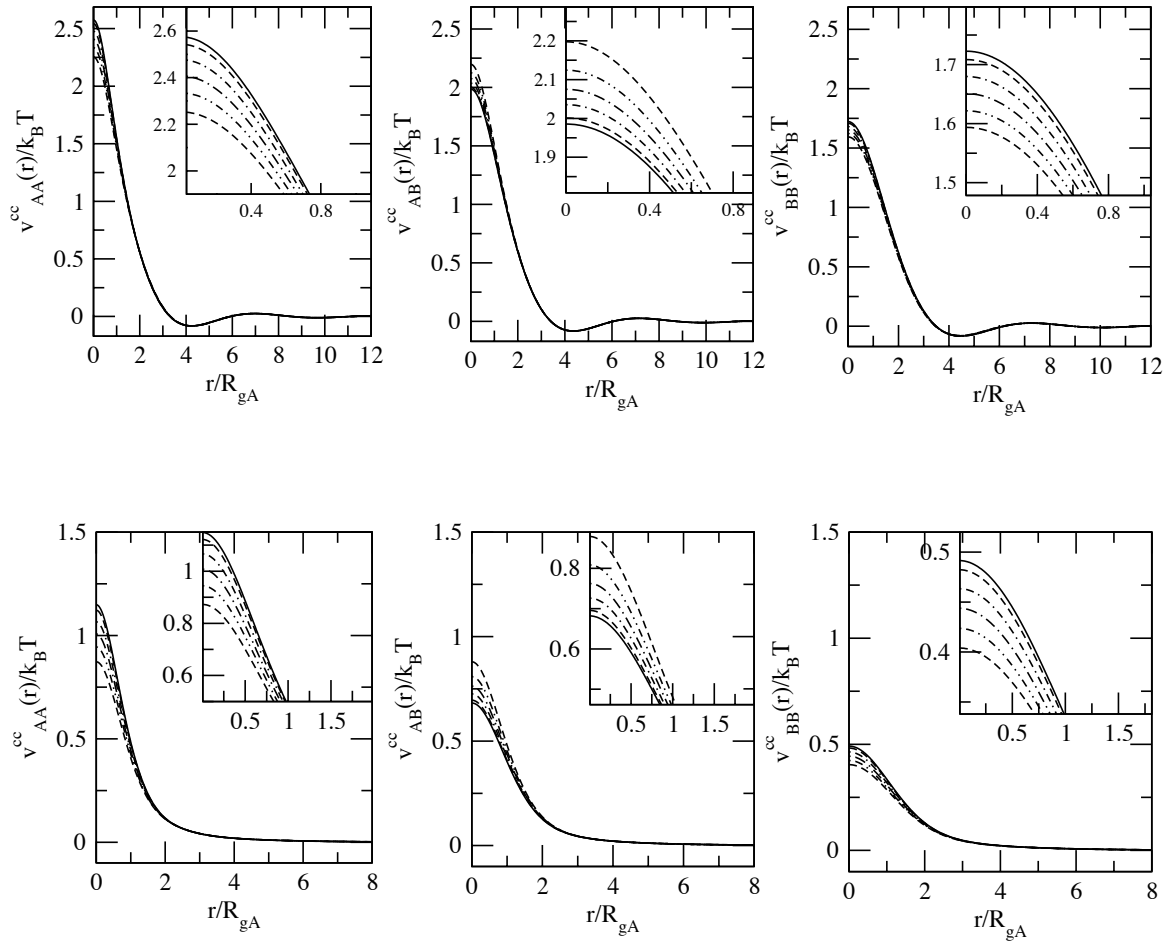


FIGURE VII.1. Comparison of the effective pair interaction potential $v_{\alpha\beta}(r)$ derived from the HNC closure for the hhPP/PE blend, $\phi = 0.5$, with $\chi/\chi_s \in \{0.0, 0.1, 0.3, 0.5, 0.7, 0.9\}$. The upper panels show $v^{cc}(r)$ obtained via the Padé approximation and the lower panels show $v^{cc}(r)$ from the Debye form. The inset highlights the change in the repulsive part of the potential as the reduced temperature is changed. The solid line represents the athermal regime ($\chi/\chi_s = 0.0$). In both the AA and BB curves, the repulsive component decreases as the system approaches the spinodal ($\chi/\chi_s = 1$), whereas the AB curve increases.

$h^{cc}(r)$ still can be readily obtained for any given system and so does not represent a limitation to our approach and avoids any singularities in the low k region for $c^{cc}(r)$. For this reason, in our following calculations the Debye approximation will be preferentially used.

The potentials $v^{cc}_{\alpha\beta}(r)$, calculated following the procedures discussed here, are required to carry out the simulations of the polymer liquid on a mesoscopic level. In the next section, we discuss the implementation of the $v^{cc}_{\alpha\beta}(r)$ to our mesoscopic simulations and in the following sections we compare mesoscale simulation results with UA MD simulations and theoretical predictions.

### VII.4. Mesoscopic Simulations of Binary Mixtures

Extensive mesoscale simulations were performed on a typical system, the hhPP/PE mixture, to investigate the consistency of our approach. Simulations were performed for compositionally symmetric mixtures, but also while approaching the spinodal, $\chi = \{0.008, 0.012, 0.016, 0.019\}$, while changing the fraction of A and B species in the melt such that $\phi = \{0.5, 0.7, 0.9\}$. Mesoscale simulation parameters for all of the hhPP/PE systems are presented in Table VII.2. For systems with $\chi$ approaching $\chi_s$, larger simulation boxes, with 10,648 particles, were used to properly account for the increase in the lengthscale of concentration fluctuations. Those systems also required longer equilibration. These simulations were run using the LONI TeraGrid system to facilitate performing numerous simulations at a time.

TABLE VII.2. Mesoscale Simulation Parameters for Blends of hhPP/PE

| Form Factor | Interaction Parameter | Particles | $\phi$ | $L/2$ $[R_g^{-1}]$ |
|---|---|---|---|---|
| Padé | $\chi/\chi_s = \{0.1, 0.3, 0.5, 0.7\}$ | 5324 | 0.5 | 8.549 |
| Debye | $\chi/\chi_s = \{0.1, 0.3, 0.5\}$ | 5324 | 0.5 | 8.549 |
| Debye | $\chi/\chi_s = 0.7$ | 10,648 | 0.5 | 10.771 |
| Debye | $\chi = \{0.008, 0.012, 0.016, 0.019\}$ | 10,648 | $\{0.5, 0.7, 0.9\}$ | 10.771 |

## VII.5. Total Pair Correlation Functions of the Polymer Mixture from Mesoscale Simulations

From the trajectories of our mesoscopic simulations, the intermolecular total pcfs are computed. Initially, we set $\chi = 0$ to determine the liquid structure far from the spinodal temperature, *i.e.* under athermal conditions, $(1 - \chi/\chi_s) = 1$. Mesoscale simulation parameters for these blends are presented in Table VII.3. For these simulations we compare the resulting pcfs to UA MD simulations. The resulting pcfs are shown in Figure VII.2 for the systems listed in Table VII.1. Mesoscopic simulations are found to yield a coarse-grained liquid structure in agreement with our theoretical predictions from the analytical expression of Equation VII.9, serving as a self-consistent check of our determination of the effective pair potential through the HNC closure. The results presented in Figure VII.2 were obtained using the Padé approximation (Equation VII.6) which works sufficiently well under athermal conditions where the low k behavior is less important since critical fluctuations are assumed to be small.

The liquid structure from mesoscopic simulations are in general consistent with data obtained from UA MD simulations, with the exception of blends containing

TABLE VII.3. Mesoscale Simulation Parameters for Athermal Blends

| System | Particles | $\phi$ | $L/2$ $[R_g^{-1}]$ |
|---|---|---|---|
| hhPP/PE | 5324 | 0.5 | 8.549 |
| PIB/PE | 4096 | 0.5 | 8.365 |
| PIB/sPP | 5488 | 0.5 | 10.416 |
| sPP/PE | 1728 | 0.5 | 5.635 |
| iPP/PE | 4913 | 0.25 | 8.482 |
| iPP/PE | 1728 | 0.75 | 6.016 |

iPP and PIB for which theoretical predictions and mesoscopic MD predict a less pronounced correlation hole than UA MD simulations. These observations are not surprising since these systems tend to possess very efficient intramolecular packing, leading to smaller isothermal compressibilities and thermal expansion coefficients when compared to other polyolefin blends.[28,95] The effective intramolecular packing arises from the attractive interactions between methyl moieties induced by their geometrical arrangement. However, the theory and mesoscopic simulations do exhibit good agreement for $r \approx R_g$.

Moving to the thermal regime, where large scale fluctuations in the local concentration develop as the system approaches a second order phase transition, we present results for the typical 50:50 mixture of hhPP/PE, although the theory and methods employed are ubiquitous and generally applicable to a wide range of systems. For these simulations the value of the $\chi$ parameter was varied such that $\chi/\chi_s = \{0.1, 0.3, 0.5, 0.7\}$, in order to see the changes in the pcfs as the system approaches the spinodal. Figure VII.3 shows the dependence of the partial correlation

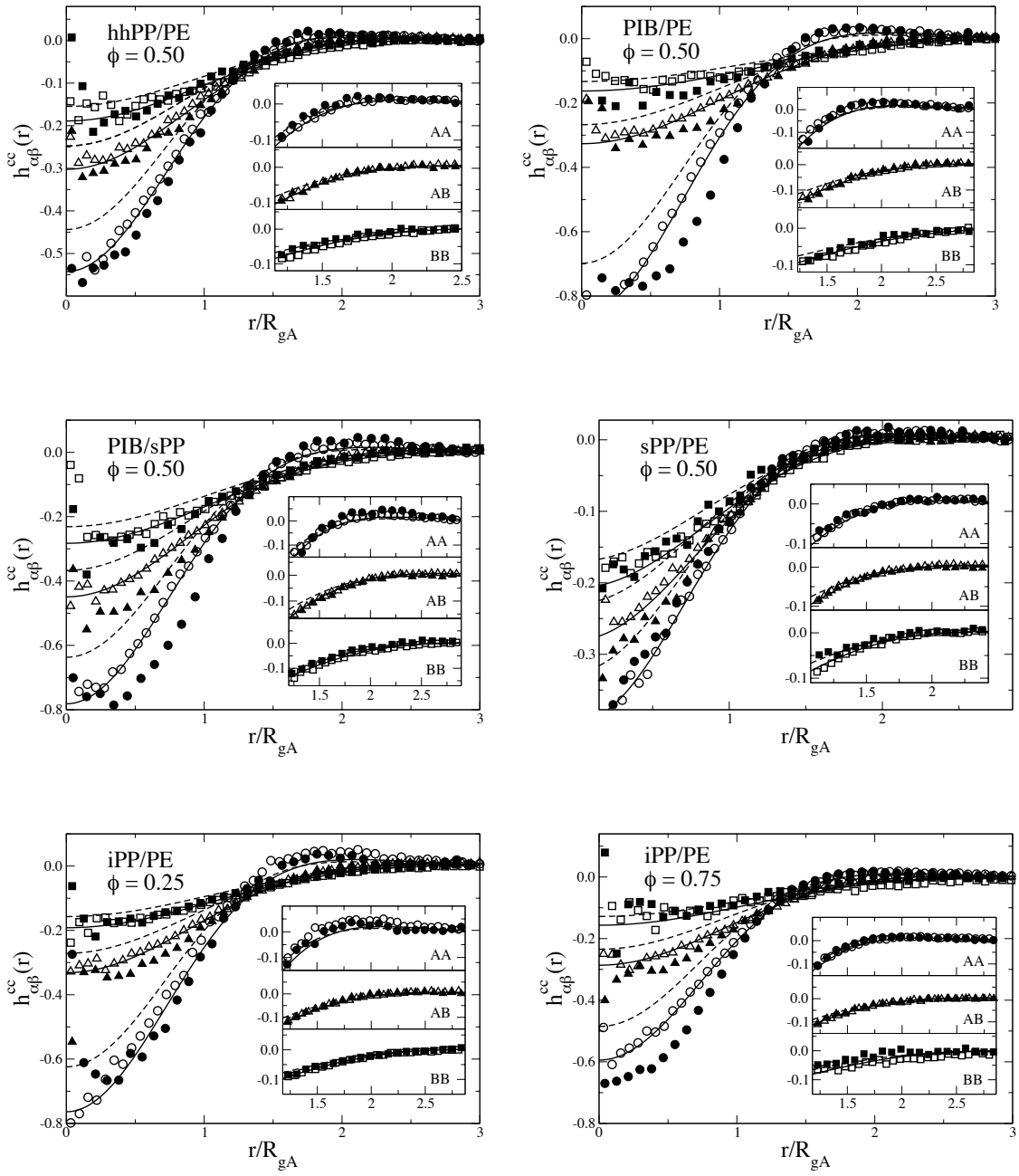


FIGURE VII.2. Comparison of mesoscopic simulations [open symbols] with UA MD simulations [filled symbols] for the $h_{\alpha\beta}(r)$ of polymer mixtures under athermal conditions. Also shown are theoretical predictions [solid curves] based on our analytic expression, Equation VII.9. Presented are data from $AA$ [circles], $AB$ [triangles], and $BB$ [squares] contributions for compositionally symmetric and asymmetric systems. For comparison, numerical predictions obtained from Equation VII.3 using the Debye form are shown [dashed curves]. For clarity the inset highlights the peak region for each separate contribution.

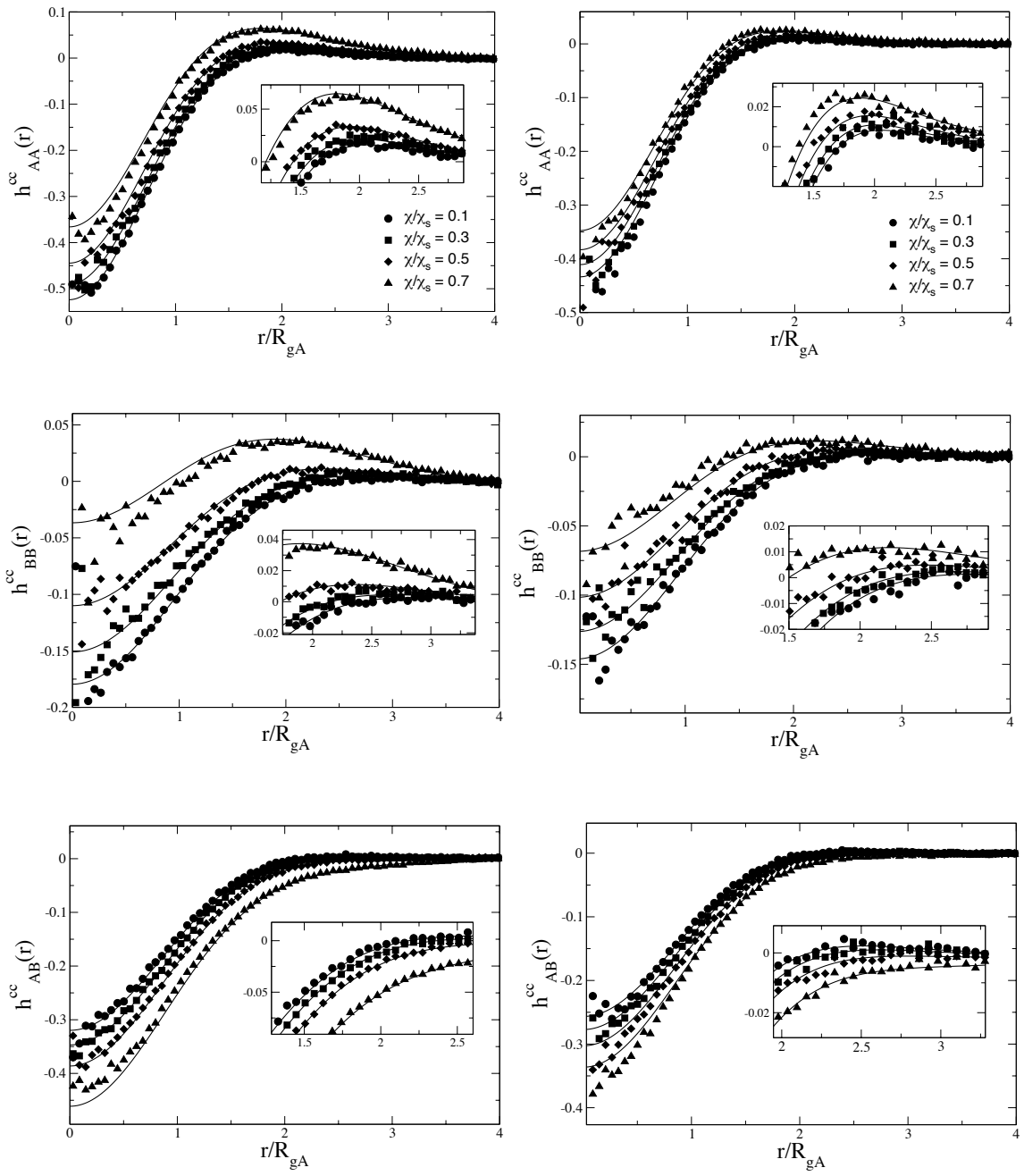


FIGURE VII.3. Comparison of mesoscopic simulations [symbols] with numerical predictions [curves] for the $h_{\alpha\beta}(r)$ of a 50:50 mixture of hhPP/PE for different values of the ratio, $\chi/\chi_s$. The left panel shows results obtained using the Padé approximation with our truncation scheme. The right panel depicts the results when the Debye form is used. Mesoscale simulations are shown to capture the structural changes that occur as the system approaches the spinodal. The inset highlights the peak region of $h(r)$

functions on the interaction parameter, $\chi$. The left side of Figure VII.3 shows the resulting correlation function from mesoscale simulations with the potential obtained via the Padé approximation, after using our truncation scheme for $c^{cc}(r)$ in the HNC (see upper panels Fig VII.1). Use of the Padé approximation has the advantage of allowing a fully analytic solution for $h^{cc}(r)$, as shown in Equation VII.9, which shows quantitative agreement with UA simulations in the athermal limit (as shown in Figure VII.2).

The right panels of Figure VII.3 shows the correlation function obtained using the potential derived from the Debye form (see lower panels of Fig VII.1). Here, comparison is again made to numerical predictions based on Equation VII.3, since an analytic solution, such as that of Equation VII.9, is not possible when the Debye form is used. In both the right and left panels of Figure VII.3 mesoscopic simulations show quantitative agreement with our theoretical predictions, indicating the self-consistency of our approach. Furthermore, despite the differences in the potential used in the simulation, Figure VII.3 shows that the resulting pcfs from either the Padé or Debye form are qualitatively similar. Lastly, it should be noted that despite the approximations made in obtaining the analytical form of Equation VII.9, the analytical expressions recover the correct k=0 limit.[38,39] In fact, all of the forms for $h^{cc}(k)$ exhibit the same $k = 0$ behavior.

The standard approach to describe the mixing behavior of polymers is the Flory-Huggins model. Under Flory-Huggins treatment, the phenomenon of demixing is understood in terms of contributions to the free energy of mixing. Generally, at low enough temperatures the translational entropy, which is associated with the center of mass motion of the molecules and always favors mixing, is outweighed by local monomer-monomer interactions. In most cases, van-der-Waals interactions are

stronger between like pairs than those between unlike pairs, resulting in a positive free energy of mixing. As a result, lower temperature favors spontaneous demixing due to changes in the local free energy of the system.[5] In an empirical manner, the Florry-Huggins parameter, $\chi$, is used to describe these changes in local free energy. At the limit of the spinodal temperature, $\chi \rightarrow \chi_s$, and since $\chi \propto \frac{1}{T}$, positive values of $\chi$ always lead to incompatibility of the mixture.[5]

In real systems, the simple Flory-Huggins model does not hold, and the $\chi$ parameter may be a complicated function of $N$, $\phi$, and $T$, leading to the variety of phase behaviors observed in polymer blends. For example, some blends phase separate upon cooling, while others show an opposite trend in demixing and phase separate upon heating. It is customary to fit the experimental temperature dependence of a mixture to the form $\chi = a + b/T$ where $a$ and $b$ may be either positive or negative depending on the system. Table **??** shows the experimentally determined $a$ and $b$ parameters for a few of the systems investigated in this paper. It should be noted that when applying an equation for the $\chi$ parameter from the literature, the $\chi$ value must be normalized by the average number of UA sites per monomer[28] to be consistent with the site-basis description adopted here.

In our present treatment, the interaction parameter, $\chi$ is treated as an adjustable parameter, which describes the interactions that drive phase separation. It is analogous to the Flory-Huggins parameter; however, since in our model it represents a system specific parameter, it may be given any value positive or negative depending on the behavior of the system of interest. The advantage of a mesoscale approach is that once the system specific parameters are defined, the trends in phase behavior can be readily calculated without requiring restrictively large MD simulations.

As a further implementation of our theory, we perform mesoscale simulations

at several fixed values of $\chi$ for which the fraction of A and B species in the melt is varied. For these simulations, we again use hhPP/PE as a typical system and vary the volume fraction such that $\phi = \{0.5, 0.7, 0.9\}$. In order to better capture the large scale structural changes, simulations were performed in a large box with 10,648 particles. Figure VII.4 shows the resulting pair correlation functions for mesoscale simulations run with $\chi = 0.008$ and $\chi = 0.012$, and Figure VII.5 shows the case where $\chi = 0.016$ and $\chi = 0.019$. In all cases, mesoscale simulations correctly capture the structural changes that depend on the concentrations of the species in the mixture when comparison is made with our theoretical predictions. For these simulations we limit our consideration to using only the Debye form in Equation VII.3 to avoid any effects due to the truncation scheme in the low $k$ region. Once more, theory and mesoscale simulations appear to be fully consistent in predicting the structural information of the mixture in the lengthscales larger or equal to the polymer radius-of-gyration.

### VII.6. Scattering Functions and Concentration Fluctuations

The mesoscale pair correlation functions effectively describe the polymer fluid as a liquid of soft colloidal particles. Once these pcfs are obtained from simulation, any property of the liquid can be calculated, including the equation of state, internal energy, compressibility, and others.[9] In this section, we examine the extent to which our classical MD simulations of soft colloidal particles reproduce the structural changes which occur as the system approaches the spinodal. Due to the increasing length scale of fluctuations as the system approaches the critical temperature for demixing, UA simulations can only reach a very limited region of the phase diagram. An advantage of using a procedure that captures the structure at the mesoscopic

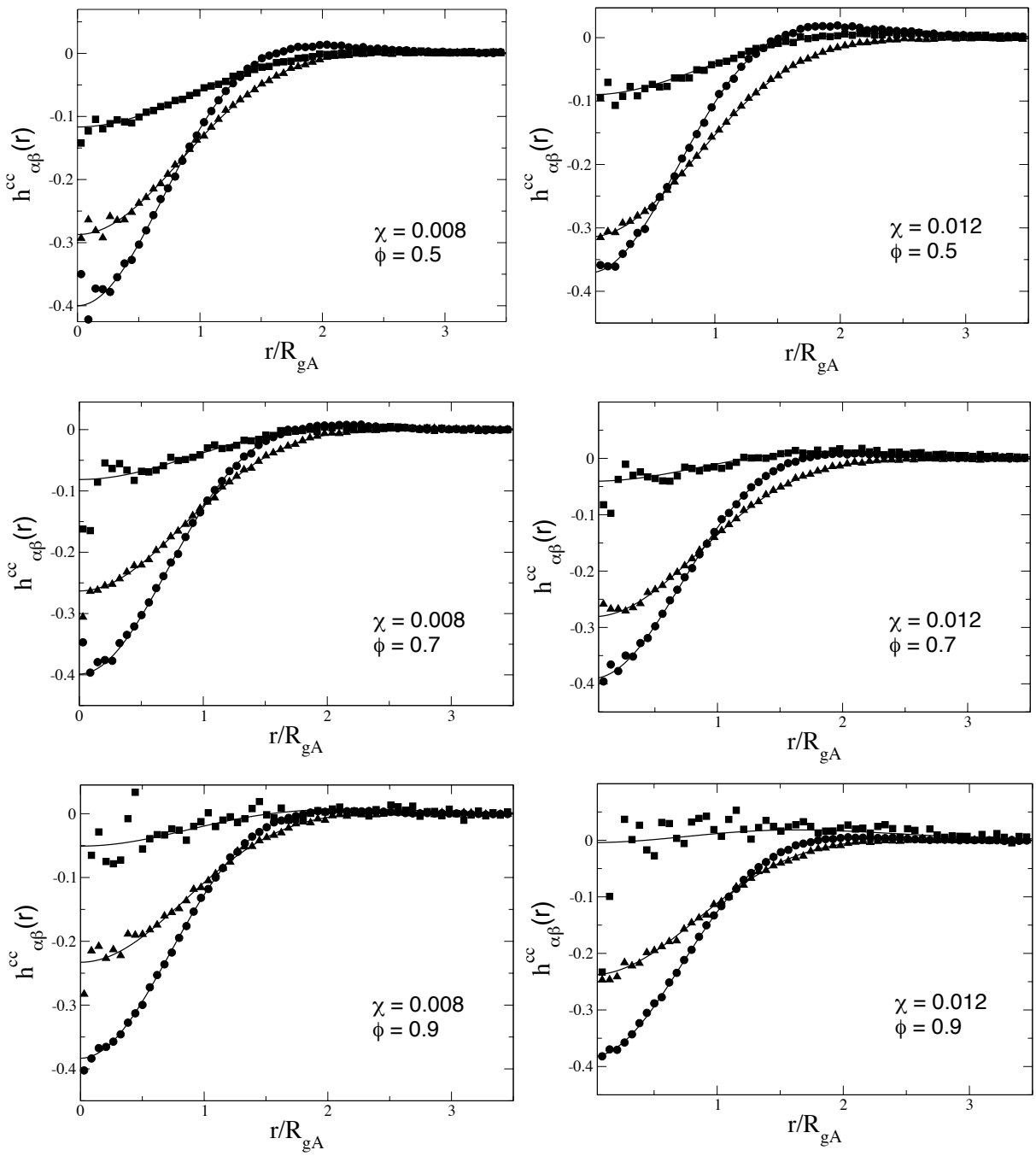


FIGURE VII.4. Comparison of mesoscopic simulations [symbols] with numerical predictions [curves] for the $h_{\alpha\beta}(r)$ of hhPP/PE for different values of $\phi$. Left panels show data when $\chi = 0.008$. Right panels show data for $\chi = 0.012$. Shown are the separate contributions for $AA$ [circles], $AB$ [triangles], and $BB$ [squares] interactions. As $\phi$ increases, the fraction of species B in the simulation box decreases, and thus, the statistics become poorer for BB interactions.

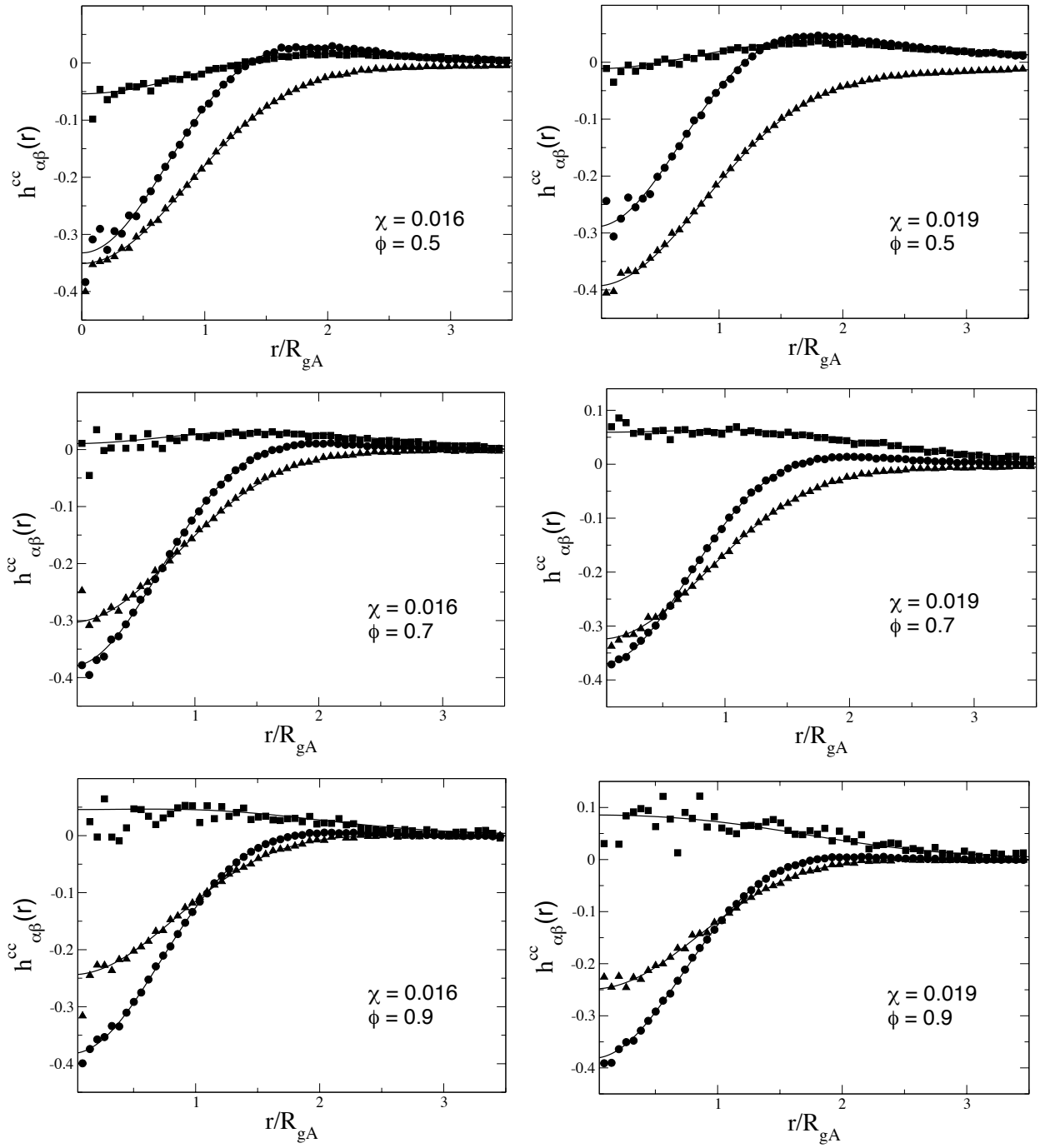


FIGURE VII.5. Same as Figure VII.4 except that left panels show data when $\chi = 0.016$, and right panels show data for $\chi = 0.019$.

scale is that the relevant length scale of the simulation can increase considerably with respect to UA MD, and simulations can describe the increasing lengthscale of the fluctuations. Thus a mesoscopic picture greatly facilitates the ability to capture this phenomenon, since we are able to simulate many thousands of chains represented as soft spheres. Models using Monte Carlo methods with phenomenological potentials have been previously performed at the level of soft colloids, demonstrating the valuable information that may be gained about phase transitions.[96,97] The advantage of the procedure presented here is that the potentials used to simulate the system are explicitly parameter dependent, being related to the system-specific molecular parameters, such as $R_g$. The potentials obtained in this manner allow for mesoscale simulations to be performed on any number of different, but specific, systems under different thermodynamic conditions, mapping them as soft colloids.

The static structure factors for each component are calculated from our simulations by Fourier transform of the total correlation function,

$$\begin{aligned} S_{AA}(k) &= \phi + 4\pi\phi^2\rho_{ch}\int_0^\infty r^2\frac{\sin kr}{kr}h_{AA}(r)dr \ , \\ S_{BB}(k) &= 1-\phi + 4\pi(1-\phi)^2\rho_{ch}\int_0^\infty r^2\frac{\sin kr}{kr}h_{BB}(r)dr \ , \\ S_{AB}(k) &= 4\pi\phi(1-\phi)\rho_{ch}\int_0^\infty r^2\frac{\sin kr}{kr}h_{AB}(r)dr \ . \end{aligned} \qquad \text{(VII.16)}$$

Density and concentration fluctuation contributions can be written as linear combinations of the static structure factors according to the formalism of Bhatia and Thornton.[98] Here, the density fluctuation, $S^{\rho\rho}(k)$ is given by

$$S^{\rho\rho}(k) = S_{AA}(k) + S_{BB}(k) + 2S_{AB}(k) \ . \qquad \text{(VII.17)}$$

The concentration fluctuation contribution, $S^{\phi\phi}(k)$ may be expressed as

$$S^{\phi\phi}(k) = (1-\phi)^2 S_{AA}(k) + \phi^2 S_{BB}(k) - 2\phi(1-\phi)S_{AB}(k) \ , \qquad \text{(VII.18)}$$

and is particularly important since it provides information about the stability of the binary mixture against demixing. The coupling term, $S^{\rho\phi}(k)$, is given by

$$S^{\rho\phi}(k) = (1-\phi)S_{AA}(k) - \phi S_{BB}(k) + (1-2\phi)S_{AB}(k). \qquad \text{(VII.19)}$$

Figure VII.6 shows the colloidal partial structure factors, $S^{\rho\rho}(k)$, $S^{\phi\phi}(k)$, $S^{\rho\phi}(k)$, calculated from pcfs obtained from mesoscopic simulations shown in the right panel of Figure VII.3 using Equations VII.17-VII.19. The data from the simulation is compared to predictions based on our numerical values for $h^{cc}(k)$, obtained from Equation VII.3 using the Debye function. Since it is particularly pertinent to capture the low $k$ behavior where concentration fluctuations will diverge as the spinodal is approached, we use the results for the Debye form since the Padé approximation introduces unphysical effects in this regime, typically for $kR_g < 2$. As seen in Figure VII.6, the curves of the density fluctuation contribution, $S^{\rho\rho}(k)$, which behaves similarly to the static structure factor for a single-component liquid,[?] are indistinguishable over the range of $\chi$ investigated. The function $S^{\rho\phi}(k)$ exhibits a slight dependence on the ratio $\chi/\chi_s$ in which the minimum at low k becomes slightly more pronounced. The minimum in $S^{\rho\phi}(k)$ represents the length scale for asymmetry in the mixture arising from the difference in particle size.[39] The partial structure factor, $S^{\phi\phi}(k)$, exhibits a characteristic diverging behavior as the spinodal is approached, indicating an increase in the length scale of concentration fluctuations.

As illustrated in the upper left of Figure VII.6, $S^{\phi\phi}(0)$ increases as the ratio

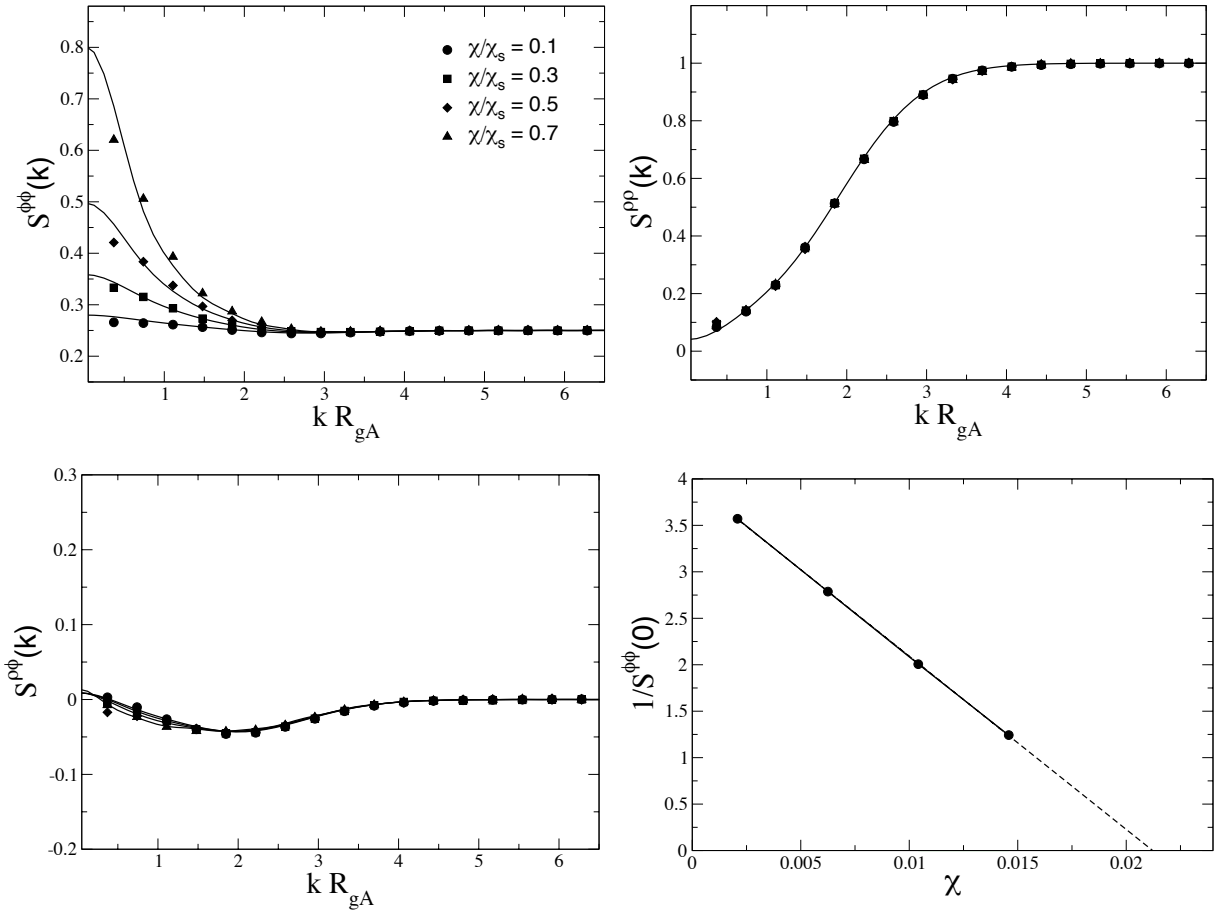


FIGURE VII.6. Top Left: Partial structure factor, $S^{\phi\phi}(k)$, obtained from mesoscopic simulations [symbols] of the coarse-grained mixture of 50:50 hhPP/PE with $\chi/\chi_s \in \{0.0, 0.1, 0.3, 0.5, 0.7\}$. The curves represent theoretical values obtained using the Debye function. Top Right: Partial structure factor, $S^{\rho\rho}(k)$ and Bottom Left: $S^{\rho\phi}(k)$ are also shown for different values of $\chi/\chi_s$. $S^{\rho\rho}(k)$ does not change noticeably with $\chi/\chi_s$ but $S^{\rho\phi}(k)$ has a slight $\chi/\chi_s$ dependence at low k. Bottom Right: Extrapolated $1/S^{\phi\phi}(0)$ values vs. $\chi$ [symbols]. The line represents a linear fit to the data and is extrapolated to the spinodal, $\chi_s$ (dashed line).

$\chi/\chi_s \rightarrow 1$. As the system nears the phase transition, the divergence of $S^{\phi\phi}(k)$ is indicative of the concentration fluctuations becoming increasingly macroscopic. Since concentration fluctuations occur on an increasingly large scale, the relevant region of the $S^{\phi\phi}(k)$ curve occurs in the low-k region; however, due to periodic boundary conditions, simulation data is only reliable at a distance less than half the length of the simulation box. This makes extrapolation of the k=0 limit from mesoscopic simulations still difficult, as seen in Figure VII.6, even though thousands of particles were represented. In this respect, our numerical predictions may serve as a guide for extending $S(k)$ to the k=0 limit. Furthermore, we have previously shown that Equation VII.9, also gives an estimate for $S^{\phi\phi}(0)$ given by[39]

$$S^{\phi\phi}(0) = \frac{\phi(1-\phi)}{1-\chi/\chi_s} + \frac{\phi^2(1-\phi)^2(\gamma^2-1)^2}{(\phi\gamma^2+1-\phi)\gamma^2}\frac{\xi_\rho^2}{\xi_{cA}^2} \ . \qquad \text{(VII.20)}$$

Even though it is based on the Padé approximation, Equation VII.20 may be used to estimate $S^{\phi\phi}(0)$ since $h^{cc}(k)$ calculated from the Padé approximation has the same $k = 0$ limit as $h^{cc}(k)$ from the Debye form. The lower right of Figure VII.6 shows a linear plot of $1/S^{\phi\phi}(0)$ vs. $\chi$ for which the $k = 0$ limit was determined by our theoretical predictions.

Following Equations VII.17-VII.19, the concentration fluctuation partial structure factor, $S^{\phi\phi}(k)$, was calculated from the mesoscale simulations presented in Figures VII.4 and VII.5, where the volume fraction, $\phi$, was changed. The resulting $S^{\phi\phi}(k)$ is presented in Figure VII.7 along with theoretically predicted values using the Debye formula. Once again, mesoscale simulations show an increase in concentration fluctuations as the thermodynamic conditions are changed, and $\chi \rightarrow \chi_s$ or $\phi \rightarrow 0.5$. In general, mesoscale simulations are consistent with our theoretical predictions based on Equation VII.3 up to the limit set by the finite box size. As seen in Figure VII.7,

when $\chi$ is low or the polymer volume fraction of one species is large, the system is well mixed and the extrapolation to low k is straightforward. However, for the case when $\phi = 0.5$ and $\chi = 0.019$, as depicted in the lower right panel of Figure VII.7, it becomes more difficult to reach the $k = 0$ limit from mesoscale simulation, even if the precision is higher than for atomistic simulations for the reasons previously discussed. Since our simulations are consistent with our theoretical predictions as shown in Figures VII.2 - VII.5, we estimate the extrapolated $S(k = 0)$ limit based on these predictions.

Once this method is employed, it is possible to discern the phase behavior of the mixture from the extrapolated $k = 0$ limit. In order to include more data points, we calculate $S^{\phi\phi}(0)$ for a range of $\chi$ and $\phi$ values, based on our solution to Equation VII.3. These are presented in Figure VII.8 which shows the structure factor as a function of the volume fraction for several fixed values of the $\chi$ parameter. The interpolation between the points is given by Equation VII.20, which demonstrates that our analytical expression is useful in determining the phase behavior.

Finally, in Figure VII.9 a plot of the inverse structure factor, $S^{\phi\phi}(0)$, vs. $\chi$ at each value of $\phi$ shows the linear behavior from which the spinodal, $\chi_s$, may be extrapolated and used to sketch the phase diagram of the system. In the bottom panel of Figure VII.9 the spinodal curve is compared to the predicted Flory-Huggins model, $\chi_s = [2N_A\phi]^{-1} + [2N_B(1-\phi)]^{-1}$, which was used in Equation VII.8. The spinodal curve from our simulation exhibits a characteristic parabolic shape consistent with mean-field theory, where $\xi_\phi \sim (1 - \chi/\chi_s)^{-\nu}$, $\nu = 1/2$. In the immediate region of the critical temperature, mean-field theory breaks down, and Ising-type critical behavior is expected. For this narrow temperature region, the linear extrapolation in Figure VII.9 would be invalid and the spinodal will exhibit

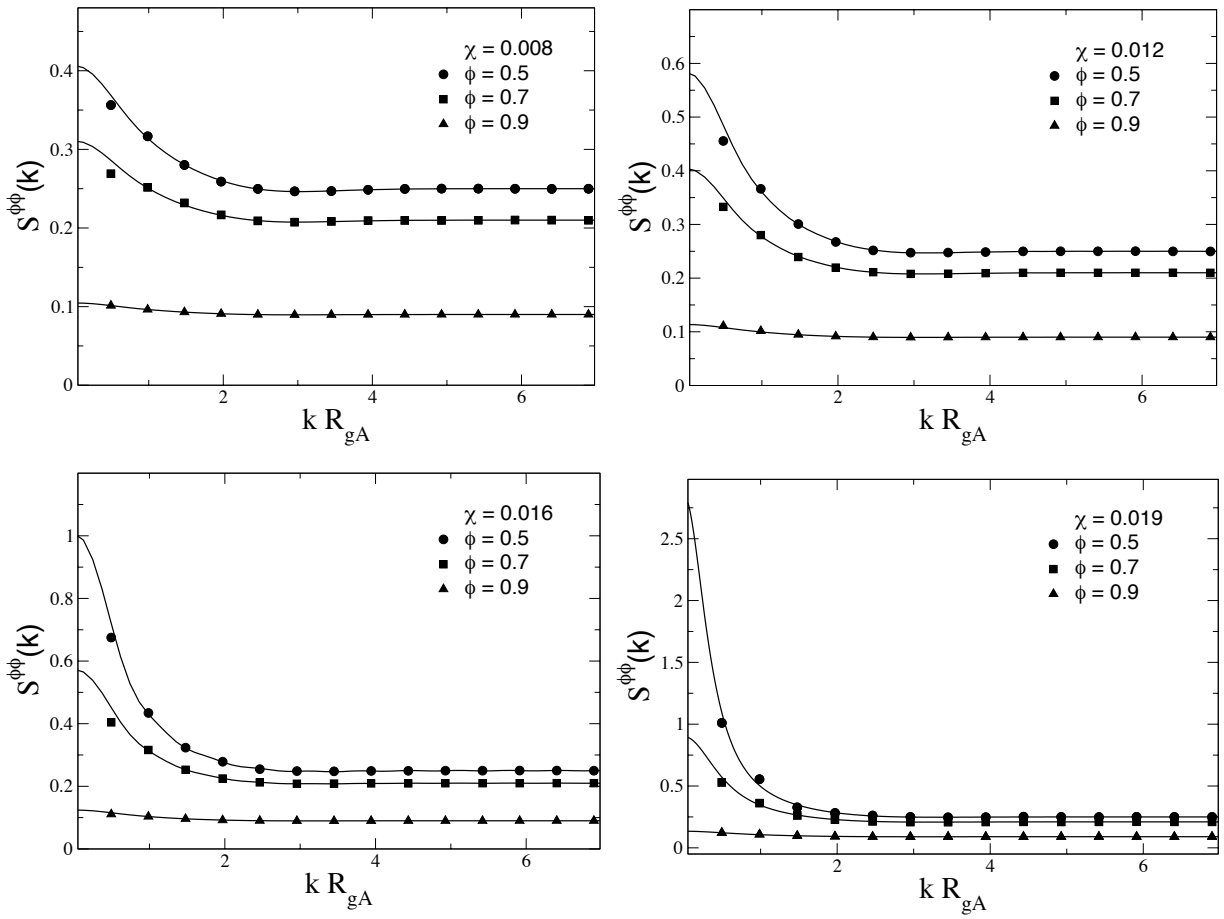


FIGURE VII.7. The concentration fluctuation partial structure factor, $S^{\phi\phi}(k)$, calculated from mesoscale simulations [filled symbols] at different values of $\phi$ for the mixture hhPP/PE. The curves represent theoretical predictions.

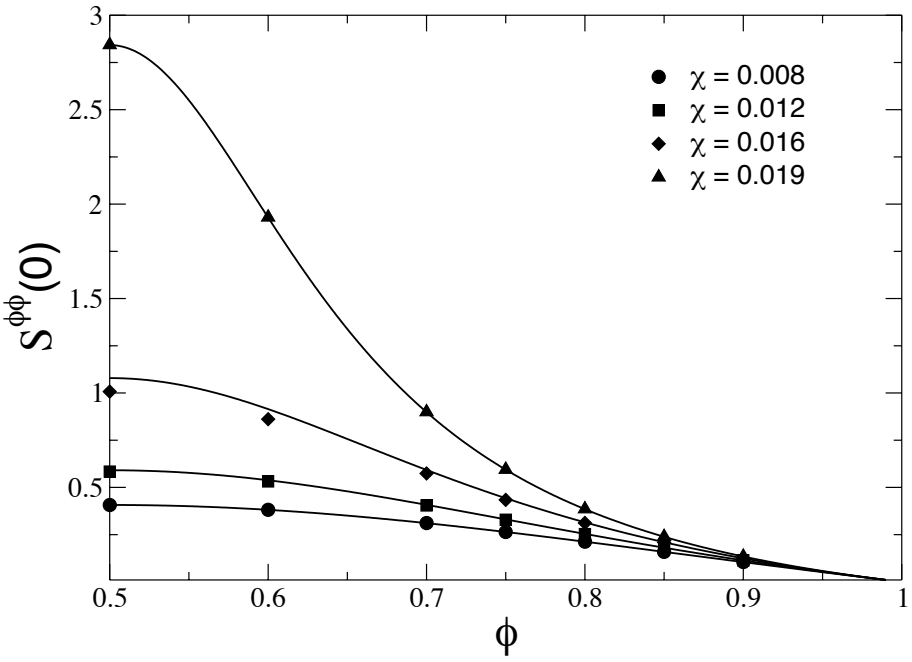


FIGURE VII.8. The extrapolated $k = 0$ limit of $S^{\phi\phi}(k)$ based on our numerical predictions [data points] and from our analytical expression, Equation VII.20, [curves] as a function of $\phi$ for different fixed values of $\chi$, for the mixture hhPP/PE.

a flatter peak.[97] For long polymer chains, the temperature region for which mean field theory becomes invalid is very small, since the Ginzburg number, which scales inversely with N, is small.[99] As seen in the upper panel of Figure VII.9 most of the simulations performed are well within the temperature region described by mean-field theory. Although the linear extrapolation becomes less quantitative near the horizontal axis, the mean-field approximation is consistent with our data.

### VII.7. Corrections to the Debye Intramolecular Form Factor

Upon examination of Figure VII.2, it appears that there is slightly better agreement between UA MD simulations when compared to our analytical results using the Padé approximation than with the full Debye form (as indicated by the dashed lines). Since the Padé form is an approximation, this improvement is likely due to a cancellation of errors. The Debye formula is exact for ideal Gaussian chains; however, Wittmer, *et. al*, have recently shown that dense polymer melts exhibit deviations from ideal Gaussian behavior because of long-range correlations arising from the repulsive interaction of chain segments.[100] These deviations become more significant for polymers confined between walls in ultrathin films.[101] In this section we investigate the implementation of higher order corrections to the Gaussian approximation on the effective pair potential by evaluating Equation VII.3 numerically with a corrected from of the intramolecular form factor.

In the infinite chain limit ($N \rightarrow \infty$) it has been proposed that corrections to the Debye formula in the intermediate wave vector range depends only on the monomer density, such that[100,102]

$$\frac{1}{\omega^{mm}(k)} = \frac{1}{\omega^{mm}_{Debye}(k)} + \frac{1}{32}\frac{k^3}{\rho} \qquad \text{(VII.21)}$$

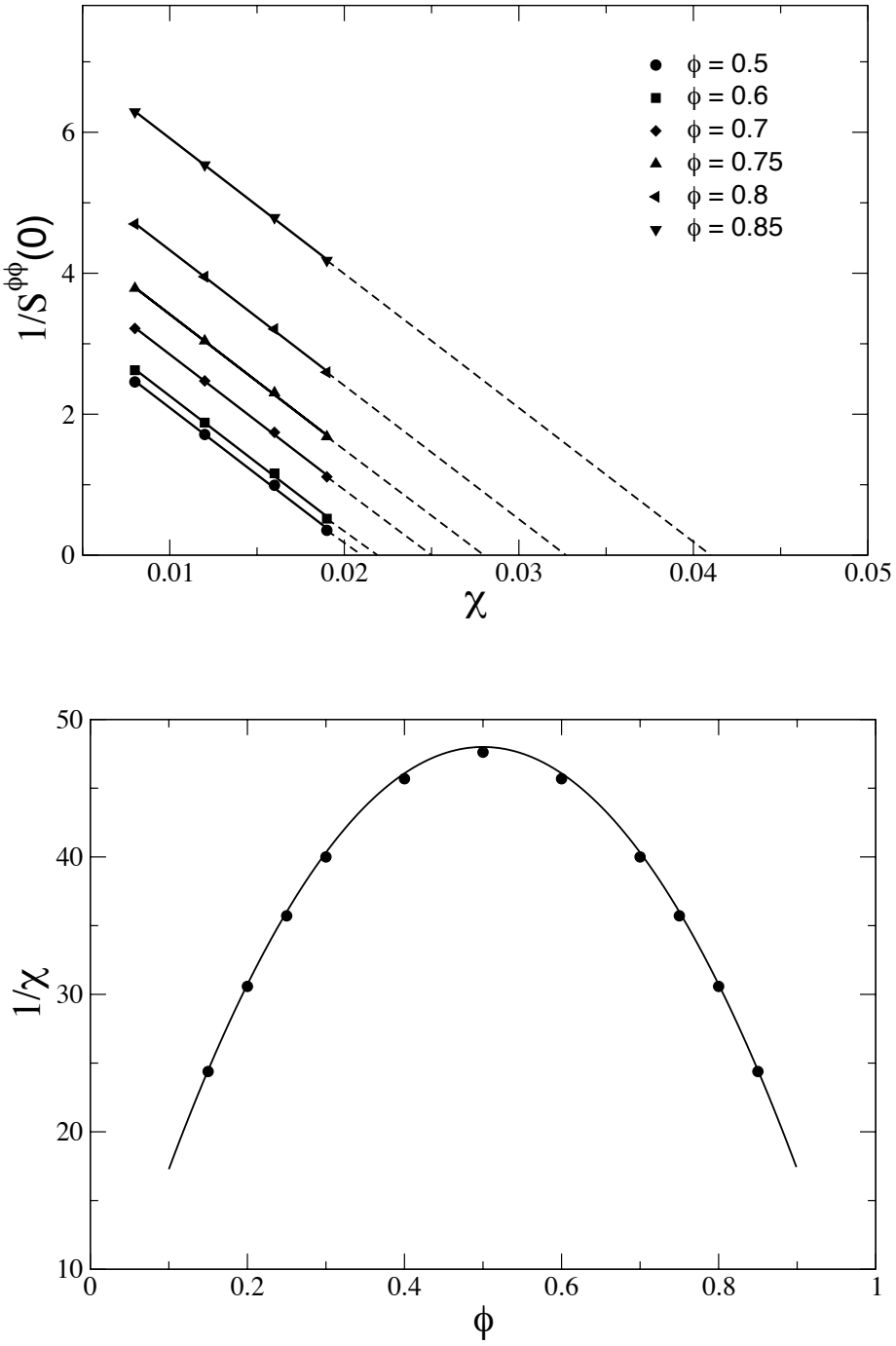


FIGURE VII.9. Top: Inverse concentration fluctuation structure factor, $S^{\phi\phi}(0)$ plotted against the interaction parameter, $\chi$ for different values of $\phi$, for the mixture hhPP/PE. The solid line depicts a linear fit to the data and the dashed line shows the extrapolation to the spinodal. Bottom: Phase diagram for the coarse-grained mixture obtained from the above extrapolation to the spinodal, $\chi_s$. The solid curve depicts the Florry-Huggins analytical expression.

Although approximate for finite chain lengths, Equation VII.21 was input into Equation VII.3 to obtain a corrected form of the pair potential which is shown in Figure VII.10 (top left) for a 50:50 mixture of hhPP/PE. The resulting correlation functions, displayed in Figure VII.10, show that the corrected Debye formula agrees very well with UA MD simulations for this sample, indicating that the disagreement between mesoscale simulations using the Debye formula and UA simulations on intermediate lengthscales is due to non-Gaussian behavior of real chains as the Flory ideality hypothesis breaks down. On the local scale, however, the corrected Debye and the UA-MD simulations tend to disagree. This is not relevant for systems with long chains, such as the hhPP:PE mixture, but it becomes important for short chains, e.g. mixtures of PIB chains, where the behavior at short distance becomes unphysical. In conclusion, while in the current publication we limit our investigation to just this correction term for the hhPP:PE mixture, further study is necessary to investigate if the observed improvement is a common feature of long-chain mixtures, independent of their monomeric structures. The pcfs obtained using the Padé approximation (Figure VII.2) are also shown in Figure VII.10 and compare well with the corrected Debye results.

## VII.8. Applications to Miscible LCST Blends

While most polymer blends are immiscible and tend to demix at experimentally relevant temperatures, some systems are known to be miscible having a lower solution critical temperature (LCST). In this section we demonstrate the extension of our approach to model LCST blends where the effective $\chi$ parameter may be negative over most of the temperature range of interest. It is worth noticing that while the hhPP/PIB blend is miscible, the iPP/PIB blend is immiscible, indicating that subtle

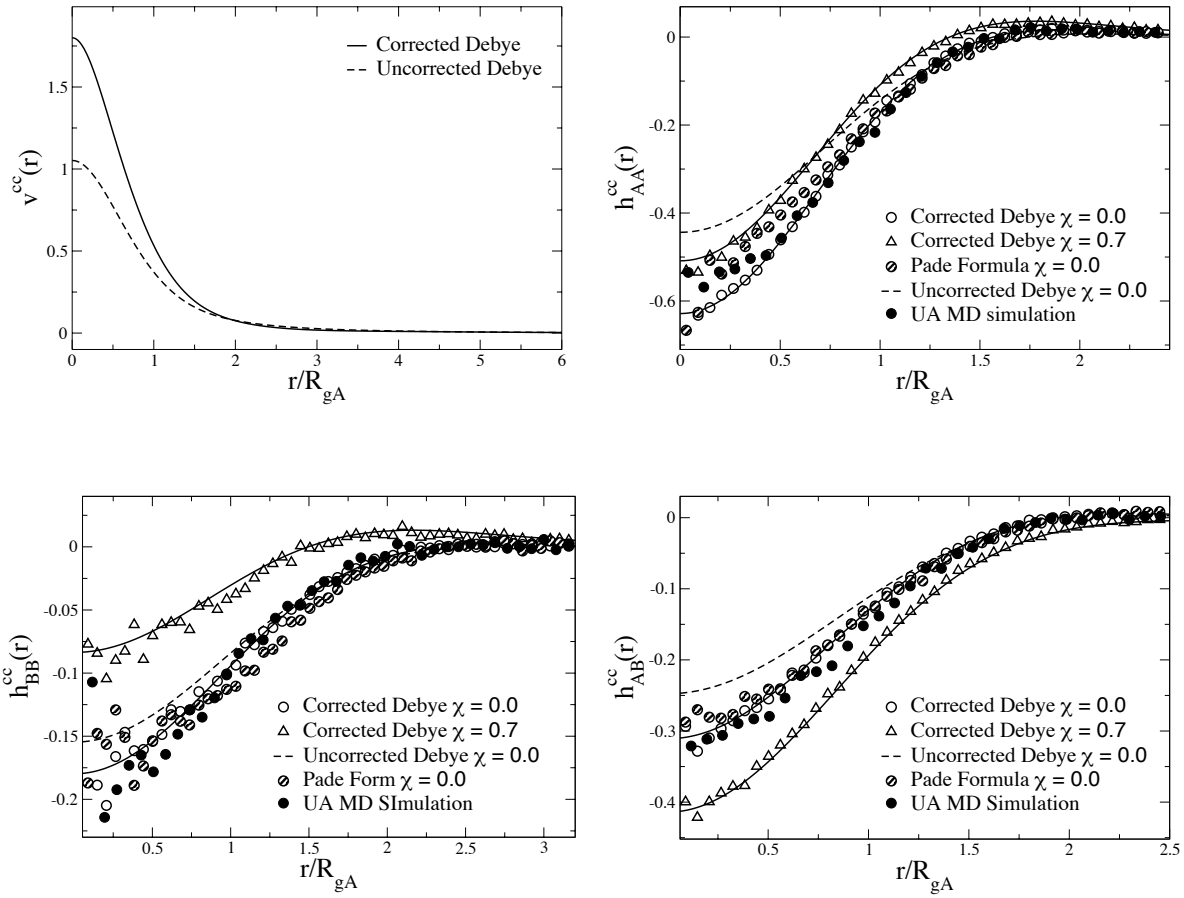


FIGURE VII.10. Top Left: The effective pair potential between A type chains for an athermal mixture of hhPP/PE with $\phi = 0.5$ when corrections to the Debye formula are included (solid line). The dashed line indicates the potential obtained using the uncorrected Debye formula. Top Right: The AA component of the correlation function calculated from mesoscale simulations using the corrected Debye formula at $\chi = 0.0$ (open circles) and $\chi = 0.7$ (open triangles). The solid line represents theoretical predictions, and the dashed line indicates predictions using the Debye formula. Filled circles represent UA MD simulations. Bottom Left: BB component and Bottom Right: AB component of the correlation function for the same mixture. The pcfs obtained using the Padé approximation are shown to nearly superimpose with the corrected Debye form. (Partially shaded circles).

changes in the specific polyolefin architecture may give rise to a completely different phase diagram. The temperature dependence of the $\chi$ parameter for the miscible hhPP/PIB blend is reported in Table **??**. The $\chi$ parameter in the literature is defined on a monomer basis and must be divided by the number of united atom sites per monomer (4.8 for hhPP/PE) to be consistent with the UA site description used here. We performed mesoscale simulations for various temperatures of a mixture of 50:50 hhPP/PIB ($\chi_s = 0.021$).

The resulting correlation functions determined for two temperatures, 2000K and 200K, from mesoscale simulations are shown in Figure VII.11. When compared with Figure VII.3 it is evident that the pcfs for the hhPP/PIB blend exhibit an opposite trend with temperature. These differences are clearly evident in the concentration fluctuation structure factor, which was calculated from these pcfs at various temperatures and is shown in the bottom right of Figure VII.11. As depicted in the low wave vector behavior of $S^{\phi\phi}(k)$, fluctuations in the concentration become smaller as the temperature is decreased, and the system becomes more stable. These results indicate that our procedure of mapping polymer blends as soft-colloids and performing mesoscopic simulations using an effective pair potential can be applied to miscible LCST blends given that the temperature dependence of the $\chi$ parameter is known.

## VII.9. Conclusion

In this chapter, the analytical coarse-grained description of the previous chapters was extended to describe polymer blends. In the athermal regime, results can be compared with both theoretical predictions and data obtained from united atom molecular dynamics simulations. In the thermal regime, mesoscopic simulations

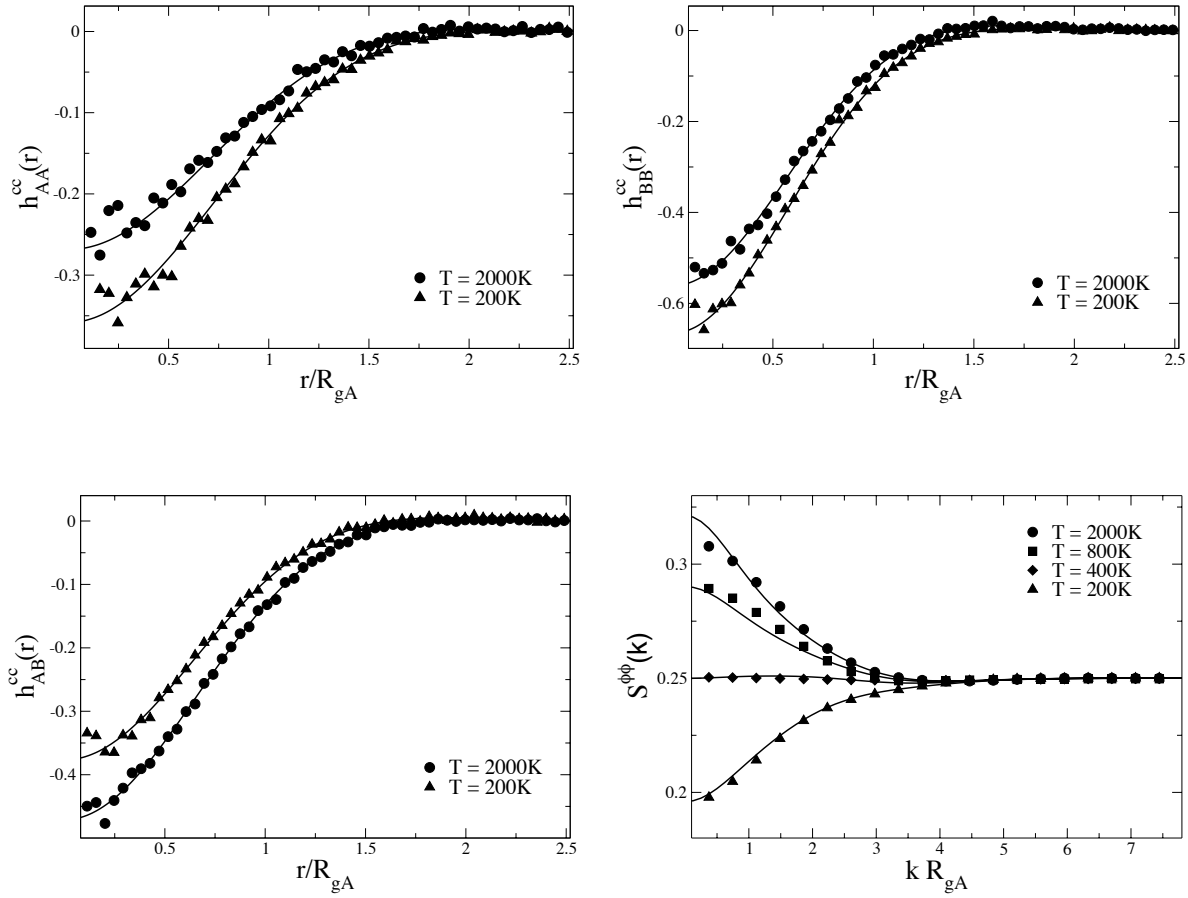


FIGURE VII.11. Top Left: AA component of the correlation function for the miscible blend, hhPP/PIB ($\phi = 0.5$) at $T = 2000K$ (circles) and $T = 200K$ (triagles). Theoretical predictions are indicated as solid lines. Top Right: BB component and Bottom Left: AB component of the same mixture. Bottom Right: The concentration fluctuation structure factor for hhPP/PIB obtained from mesoscale simulation (symbols) and from theory (solid line) at various temperatures.

capture the relevant trends for demixing of polymers in the miscible regime approaching the spinodal where united atom simulations are too computationally costly. These results are used to calculate static structure factors which are related to the increasing concentration fluctuations of the mixture. By extrapolation to the low wave vector limit, we are able to determine the phase diagram of the coarse-

grained mixture which is consistent with mean-field theory predictions.

# CHAPTER VIII

# CONCLUSION

## VIII.1. Perspectives on the Completed Work

This dissertation has presented a study of the thermodynamic and structural properties of a novel coarse-grained model for macromolecular liquids. The method is based in liquid state theory and formally connects the coarse-grained distribution functions to the underlying monomer distributions through an Ornstein-Zernike-type expression. The main objective in developing a coarse-grained model is to obtain the effective pair potential between sites. Chapter II presented a detailed derivation of the effective potential for an arbitrary number of blocks. An analytical expression for this pair potential was derived for systems for which the intramolecular monomer distribution follows Gaussian statistics, which is the case for dense polymer melts. One of the longstanding goals in coarse graining is deriving transferable potentials that can be used over a variety of conditions. This is problematic for coarse-grained methods which rely on an all-atom simulation to parameterize the model because the optimized potential is not transferable to another set of state conditions. The method proposed here has the advantage over numerical methods in that the potential is obtained analytically and does not require a numerical optimization against a more detailed model. In other words, the transferability problem is circumvented because the potential can be immediately obtained for any system at any thermodynamic state point of interest.

In developing a coarse-grained model, it is important that the coarse-grained description reproduces the correct physical properties of the "real" system. In

other words, the coarse-grained model must capture the relevant physics as one is interested in simulating a well defined thermodynamic state. Thus, Chapters III, IV, and V devote much time to establishing the thermodynamic consistency of the coarse-grained model. Numerically obtained potentials optimized to reproduce a specific property generally do not reproduce any other property of the system, a problem referred to as the representability problem. The proposed coarse-graining scheme in this dissertation is thermodynamically consistent in that the pressure, compressibility, structural distributions, and free energy are all consistent across multiple levels of description. This is another major advantage of this procedure over numerical methods because the coarse-grained description reproduces the correct underlying physical properties of the system represented. Having an analytical form of the potential is also advantageous as it allows for the direct calculation of thermodynamic quantities of interest. In Chapter III we used the analytical PRISM thread model to derive the equation of state for a homopolymer melt. Because this model can be solved analytically and compared to mesoscale simulations directly, it is possible to identify key features in the formalism that are important for thermodynamic consistency. For example, cutting the force in the numerical simulations even at lengths larger than the characteristic length of the system (several $R_g$) introduces errors in the pressure and energy as these quantities are sensitive to the long range tail of the potential. Furthermore, a formal solution of the potential of mean force (pmf) shows that the properties derived from using the pmf as the pair potential are fundamentally different than those calculated with the correct potential.

In Chapters IV and V a more realistic scheme to obtain the coarse-grained potential was developed for systems not described by the idealized thread model.

The main achievement of this work was obtaining a generalized equation of state for a homopolymer liquid which has a similar form to that of a hard sphere fluid. The pressure for polyethylene chains at different temperatures, densities, and chain lengths, was shown to collapse onto a universal curve when plotted versus an effective packing fraction. Thus, the single parameter, the effective hard sphere diameter, determines the thermodynamic state of the model. Here we were able to show quantitative comparison to united atom simulations of polyethylene melts for several different levels of coarse-graining. It was also demonstrated that a simple equipartition correction to the energy nearly completely accounts for the difference in the internal energy and entropy between different levels of block descriptions.

While the first part of the dissertation dealt with the derivation and thermodynamics of the coarse-grained model, the second part was concerned with applications of the proposed method. Chapter VI presented a novel multi-scale modeling procedure for both homopolymer melts and blends. The procedure utilizes the inverse of the Ornstein-Zernike relation to reverse-map the center of mass distributions from coarse-grained simulations to obtain the monomer-level distributions functions. Because the coarse-grained system only captures information on the lengthscales larger than the coarse-grained unit, the distributions are combined in Fourier space with the distributions from a local all-atom simulation. Subsequent Fourier transform provides the complete monomer-level distribution functions obtained at much greater computational efficiency than would be required to run the complete atomistic simulation.

Chapter VII presents the application of the procedure to binary mixtures of homopolymer blends. This is important from an engineering standpoint because most composite materials are processed in their molten liquid state, and one would

like to custom design new materials guided by insight from computer modeling. The proposed coarse-graining procedure allows one to efficiently simulate binary polymer mixtures in the miscible region of the phase diagram up to the spinodal. Because the thermodynamic conditions of the model are well established, the procedure promises to be useful in quantitative predictions of polymer mixtures.

## VIII.2. Future Directions

Having established the coarse-grained procedure and its usefulness in multi-scale modeling of complex fluids, it would be useful at this point to briefly describe some of the future directions for this research. I have done some preliminary work along these lines, but not enough to include as a complete chapter in this dissertation.

First, the procedure is currently being implemented in an algorithm to rapidly equilibrate melts of long polymer chains. In studying the dynamics of long polymer chains, it is import to have a structure with the correct statistical distribution of chain entanglements. However, generating random starting configurations does not generally produce a properly entangled system, and letting the system relax to an appropriate equilibrium configuration is computationally restrictive. Hence, molecular dynamic simulations are available for polymers that are only slightly entangled, with only a few entanglements per chain. There is active interest in developing methods to rapidly equilibrate a dense liquid of polymers which can then be used in molecular dynamics simulations to study the dynamics of chain relaxation, and also to understand the viscoelastic response to strain in non-equilibrium MD. One algorithm which has been developed is the end-bridging (EB) Monte Carlo algorithm developed by Mavrantzas and co-workers, which has been shown to efficiently equilibrate long chains.[103] This method works well for linear chains, but

is more complicated for branched system where one has to preserve the number of branched units.

Another method is to use a coarse-grained model to equilibrate the global structure and then reinsert the monomers as random walks, preserving the center of mass distribution. The motivation is that the coarse-grained simulation will rapidly equilibrate and reproduce the global structure, and then the random walk chains only have to be locally relaxed for a shorter amount of time. We are developing an alternative rapid equilibration scheme in which random walk chains are generated, and coarse-grained sites are generated along these chains at the center of mass of a select group of monomers. The coarse-grained sites interact via the effective potential described in this dissertation, and the monomer pair interactions are turned off during this stage but allowed to move collectively with the coarse-grained coordinates. Because the effective potential is soft, the chains rapidly reach an equilibrium distribution, after which the coarse-grained potential is turned off, and the monomers are allowed to subsequently relax locally. The advantage of the procedure is that the coarse-grained potential can be turned on and off allowing for switching between coarse-grained and all-atom simulations on the fly. For example, the coarse-grained simulation may be run for a short trajectory, turned off with the chains being allowed to locally relax, and then coarse-grained sites can be re-introduced after a short MD run. The entire procedure can be repeated indefinitely. Another advantage is that the thermodynamics are unchanged when switching between different levels of description, allowing one to seamlessly equilibrate chains while simultaneously relaxing them locally. This method should be a useful way to generate properly equilibrated starting configurations for molecular dynamics simulations.

Another direction of interest is to use the coarse grained procedure to

study polymers of more complex architecture than those discussed in the current dissertation. The coarse-grained procedure described above is general and applicable to any system for which the Ornstein-Zernike equation is an accurate description. For systems for which the intramolecular distributions no longer obey Gaussian statistics, one can compute these numerically from short united atom simulations and the procedure would be numerically implemented. The procedure to obtain the direct correlation parameter would be the same as presented in Chapter V, where one needs the semi-flexible chain parameters for the more complicated architecture which may be obtained by comparison to united atom simulations or from the literature. For example, the semi-flexible chain model has been successfully used to describe polystyrene using PRISM theory.[104] This can be used to parameterize our coarse-grained potential for polystyrene.

In moving to more complicated systems, the theory will have to be developed for polyelectrolytes. Again, the coarse-grained relations described above are still valid, but the monomer level PRISM theory for polyelectrolytes needs to be used. For example, Yethiraj has developed the integral equation theory for rigid polyelectrolytes in solution.[105] This could be implemented to parameterize a coarse-grained model for DNA. Additionally, for ionic species, the hypernetted chain closure may not be the correct closure to use for obtaining the potential, but the potential can be derived in a similar method using a closure for charged species. For example, the LWC closure was suggested by Chandler and co-workers in the context of solvated electrons in a liquid.[106] The long-term goal would be to use this procedure along with the multi-block model to simulate coarse-grained amphipathic systems. This would be useful to investigate block co-polymers of increased complexity where a variety of microphases occur. Furthermore, this would provide a stepping stone to develop

a coarse-grained procedure for DNA which might help to bridge the gap between low level coarse-grained models of DNA such as those of de Pablo[55] and very generic chain models such as the wormlike chain model.

# APPENDIX

# SAMPLE PYTHON FUNCTION TO GENERATE THE COARSE-GRAINED POTENTIAL

## A.1. Soft Sphere

This subroutine calculates the effective potential for use in LAMMPS simulations. The inputs are the number of monomers, temperature, monomer density, radius of gyration, and the direct correlation parameter $c_0$.

```
# function to calculate potential
def func_potl(N,T,rhom,Rgyr,c0):
    from numpy import exp
    from scipy.fftpack import fft
    import fofrfunc
    from numpy import log
    import derivtif
    from newsavetxt import savetxthd

    Navo= 6.022*10**(23.0)
    kB = 3.297627*10**(-27.0)   # in Kcal/K
    kBT = kB*T*Navo       # in Kcal/mol
    #
    rhoc = rhom/N    # chain number density
    rhor = rhoc*Rgyr**(3.0)  # reduce density
    #   for specific c0 value
    ckk0 = c0/Rgyr**(3.0) # in reduced units
    #   Algorithm parameters
    knum = 4001 # number of k-values
    klim = 40.0 # largest k-value
    delk = float(klim/(knum-1)) # increment step
    # initialize abscissae in k-space
    kval = arange(knum-1)
    kval = kval*delk
    # in real space
    rval = arange(4001)
    rval = rval*0.01
    part = arange(4001)
```

```
for i in range(0,4001):
    part[i]=i+1

# Calculate Debye from factor
wmmdk = 2.0*N/kval**(4.0)*(exp(-kval**(2.0))-1.0+kval**(2.0))
wmmdk[0]=N # to avoid division by zero
dataout = column_stack((kval,wmmdk))
savetxt('wmmk.txt',dataout)
# monomers distribution about c.o.m.
wcmgk = sqrt(pi)/kval*N*special.erf(kval/2.0)*
exp(-kval**(2.0)/12.0)
wcmgk[0] = N
dataout = column_stack((kval,wcmgk))
savetxt('wcmk.txt',dataout)
################################################
# Calculate hcck and ccck from (paper here)
hmmdk = wmmdk**(2.0)*ckk0/(1.0-wmmdk*N*rhor*ckk0)
hccdk = (wcmgk/wmmdk)**(2.0)*hmmdk
dataout = column_stack((kval,hccdk))
savetxt('hcck.txt',dataout)
cccdk = hccdk/(1.0+rhor*hccdk)
################################################
# Numerical Fourier Transform
hccdr = fofrfunc.fofrfunc(kval, hccdk, rval)
dataout = column_stack((rval*Rgyr,hccdr))
savetxt('hccr.txt',dataout)
cccdr = fofrfunc.fofrfunc(kval, cccdk, rval)
dataout = column_stack((rval*Rgyr,cccdr))
savetxt('cccr.txt',dataout)
# correlation funtions written in real-units (not Rg units)
# HNC potential
vccdr = hccdr - log(hccdr+1) - cccdr
dccdr = derivtif.derivtif(rval, vccdr)
vccdr = vccdr*kBT # energy in Kcal/mol
dccdr = -1.0*dccdr*float(kBT/Rgyr) # force in Kcal/(mol*A)
rval[0] = 1.0*10**(-23.0) # to avoid r=0 LAMMPS error
rvalr = rval*Rgyr # distance in A
# write out potential to check
dataout = column_stack((rvalr,vccdr))
savetxt('vccr.txt',dataout)
# write potential file in LAMMPS format
l=len(rvalr)
```

```
    val=str(l)
    txt=' N       ' + val
    hdrtxt ='soft_potl\n'
    hdrtxt += txt
    hdrtxt += '\n'
    hdrtxt += '\n'
    dataout = column_stack((part,rvalr,vccdr,dccdr))
    savetxthd(name,dataout, header=hdrtxt,
    fmt=('%12.0i  %24.16e %24.16E %24.16E'))
    dataout = column_stack((rvalr,dccdr))
    savetxt('dccr.txt',dataout)
    return (rvalr,dccdr)
```

### A.2. Tri-Block Model

This is the tri-block version of the code. This additional input is the number of soft blobs. For the tri-block model this is 3.

```
# function to calculate triblock potential
def func_potl(N,blobs,T,rhom,Rgyr,c0):
    from numpy import exp
    from scipy.fftpack import fft
    import fofrfunc
    from numpy import log
    import derivtif
    from newsavetxt import savetxthd
    from numpy import cos
    from numpy import arccos
    from numpy import sin
    from numpy import sqrt

    Navo= 6.022*10**(23.0)
    kB = 3.297627*10**(-27.0)   # in Kcal/K
    kBT = kB*T*Navo       # in Kcal/mol
    numb=N/blobs
    Rgyrb=Rgyr/sqrt(blobs)
    #
    rhoc = rhom/N    # chain number density
    rhob = rhom/numb  # blob density
    rhor = rhoc*Rgyrb**(3.0)  # reduce chain density
    rhomr = rhom*Rgyrb**(3.0) # reduced monomer density
    rhobc = rhob*Rgyrb**(3.0) # reduced blob density
```

```
#   for specific c0 value
ckk0 = c0/Rgyrb**(3.0) # in reduced units
gamma=-numb*ckk0*rhomr
#   Algorithm parameters
knum = 4001 # number of k-values
klim = 40.0 # largest k-value
delk = float(klim/(knum-1)) # increment step
# initialize abscissae in k-space
kval = arange(knum-1)
kval = kval*delk
# in real space
rval = arange(4001)
rval = rval*0.01
part = arange(4001)
for i in range(0,4001):
    part[i]=i+1

Wmmdk = 2.0*(exp(-blobs*kval**(2.0))-
1.0+blobs*kval**(2.0))/(blobs**(2.0)*kval**(4.0))
Wmmdk[0]=1.0 # to avoid division by zero
# Write monomer omega distribution to check!  (units of Rgb)
dataout = column_stack((kval,Wmmdk))
savetxt('Wmmk.txt',dataout)
# Calculate monomers distribution about c.o.m.
# (Equation 13 in Clark, J. Phys. Chem.)
Wcm0 = sqrt(pi)/kval*special.erf(kval/2.0)*exp(-kval**(2.0)/12.0)
Wcm0[0] = 1
Wcm1=exp(-kval**(2.0)/3.0)*(1-exp(-kval**(2.0)))/(kval**(2.0))
Wcm1[0] = 1
Wcm2=exp(-4.0*kval**(2.0)/3.0)*(1-exp(-kval**(2.0)))
/(kval**(2.0))
Wcm2[0] = 1
# Writing cm omega distributions to check! (in units of Rgb)
dataout = column_stack((kval,Wcm0))
savetxt('Wcm0k.txt',dataout)
dataout = column_stack((kval,Wcm1))
savetxt('Wcm1k.txt',dataout)
dataout = column_stack((kval,Wcm2))
savetxt('Wcm2k.txt',dataout)
########################################
denY=Wmmdk*blobs
denZ=denY**(2.0)
```

```
nmr11=(Wcm0+Wcm1+Wcm2)**2.0        # Eqn 19
nmr12=(Wcm0+Wcm1+Wcm2)*(Wcm0+2.0*Wcm1)   # Eqn 20
nmr22=(Wcm0+2.0*Wcm1)**2.0               # Eqn 21
##########################################
X011=nmr11/(denY)
X012=nmr12/(denY)
X022=nmr22/(denY)
##########################################
X111=nmr11/(denZ)
X112=nmr12/(denZ)
X122=nmr22/(denZ)
##########################################
X211=nmr11/(denY**3.0)
X212=nmr12/(denY**3.0)
X222=nmr22/(denY**3.0)
##########################################
hbbk11=-numb*(X011-(1.0/gamma)*X111+(1.0/gamma**2.0)*X211)/(rhom)
hbbk12=-numb*(X012-(1.0/gamma)*X112+(1.0/gamma**2.0)*X212)/(rhom)
hbbk22=-numb*(X022-(1.0/gamma)*X122+(1.0/gamma**2.0)*X222)/(rhom)
##########################################
# Now calculate Blob-Blob omegas
Wbb1=exp(-2.0*kval**(2.0)/3.0) # Eqn. 16
Wbb2=exp(-5.0*kval**(2.0)/3.0)
Wbbtot=Wbb1+Wbb1+Wbb2
dataout = column_stack((kval,Wbb1,Wbb2,Wbbtot))
# Write out Wbb(k) in units of Rgb
savetxt('Wbbk.txt',dataout)
##########################################
# Now calculated the direct correlation c(r)
D31=1.0-2.0*(Wbb1**(2.0))+Wbb2-4.0*rhoc*hbbk12*Wbb1+
rhoc*Wbb2*hbbk22
D32=2.0*hbbk11+hbbk22-2.0*rhoc*(hbbk12)**(2.0)+
2.0*rhoc*hbbk11*hbbk22
Dtot=(2.0*(Wbb1)**(2.0)-Wbb2-1.0)*(D31+rhoc*D32)
surt=D31
blurt=D32
nrut=2.0*(Wbb1)**(2.0)-Wbb2-1.0
cbbk11=-(hbbk11-2.0*hbbk12*Wbb1+(Wbb1)**(2.0)*hbbk22-
rhoc*(hbbk12)**(2.0)

+rhoc*hbbk11*hbbk22)/Dtot
######################################################
```

```
 cbbk12=-(hbbk12*(1.0+2.0*(Wbb1**(2.0))+Wbb2)+
 2.0*rhoc*Wbb1*(hbbk12)**(2.0)-
 Wbb1*(2.0*hbbk11+hbbk22+hbbk22*Wbb2+
 2.0*rhoc*hbbk11*hbbk22))/Dtot

 cbbk22=-(4.0*hbbk11*(Wbb1**2.0)-
 4.0*hbbk12*Wbb1*(1.0+Wbb2)-2.0*rhoc*
(1.0+Wbb2)*(hbbk12**2.0)+hbbk22*(1.0+Wbb2)*
(1.0+Wbb2+2.0*rhoc*hbbk11))/Dtot
 ########################################################
 ###### fix k=0 ##########################################
 cbbk11[0]=hbbk11[0]/(1+rhoc*hbbk11[0])/blobs**2
 cbbk12[0]=hbbk12[0]/(1+rhoc*hbbk12[0])/blobs**2
 cbbk22[0]=hbbk12[0]/(1+rhoc*hbbk22[0])/blobs**2
 ########################################################
 # Write distributions in units of Rgb
 dataout = column_stack((kval,hbbk11))
 savetxt('hbbk11.txt',dataout)
 dataout = column_stack((kval,hbbk12))
 savetxt('hbbk12.txt',dataout)
 dataout = column_stack((kval,hbbk22))
 savetxt('hbbk22.txt',dataout)
 dataout = column_stack((kval,cbbk11))
 savetxt('cbbk11.txt',dataout)
 dataout = column_stack((kval,cbbk12))
 savetxt('cbbk12.txt',dataout)
 dataout = column_stack((kval,cbbk22))
 savetxt('cbbk22.txt',dataout)

 ################################################
 # Now Fourier Transform to real space
 hbbr11 = fofrfunc.fofrfunc(kval, hbbk11, rval)
 hbbr11 = hbbr11/(Rgyrb**3)
 hbbr12 = fofrfunc.fofrfunc(kval, hbbk12, rval)
 hbbr12 = hbbr12/(Rgyrb**3)
 hbbr22 = fofrfunc.fofrfunc(kval, hbbk22, rval)
 hbbr22 = hbbr22/(Rgyrb**3)
 dataout = column_stack((rval*Rgyrb,hbbr11))
 savetxt('hbbr11.txt',dataout)
 dataout = column_stack((rval*Rgyrb,hbbr12))
 savetxt('hbbr12.txt',dataout)
 dataout = column_stack((rval*Rgyrb,hbbr22))
```

```
savetxt('hbbr22.txt',dataout)
cbbr11 = fofrfunc.fofrfunc(kval, cbbk11, rval)
cbbr12 = fofrfunc.fofrfunc(kval, cbbk12, rval)
cbbr22 = fofrfunc.fofrfunc(kval, cbbk22, rval)
cbbr11 = cbbr11/(Rgyrb**3)
cbbr12 = cbbr12/(Rgyrb**3)
cbbr22 = cbbr22/(Rgyrb**3)
dataout = column_stack((rval,cbbr11))    # Write c(r)
savetxt('cbbr11.txt',dataout)
dataout = column_stack((rval,cbbr12))
savetxt('cbbr12.txt',dataout)
dataout = column_stack((rval,cbbr22))
savetxt('cbbr22.txt',dataout)
# Calculate HNC potential
vccdr11 = hbbr11 - log(hbbr11+1) - cbbr11
dccdr11 = derivtif.derivtif(rval, vccdr11)
vpmf11 = -log(hbbr11+1)   # Potential of mean force
dvpmf11 = derivtif.derivtif(rval, vpmf11)
vccdr11 = vccdr11*kBT # energy in Kcal/mol
vpmf11 = vpmf11*kBT
dccdr11 = -1.0*dccdr11*float(kBT/Rgyrb) # force in Kcal/(mol*A)
dvpmf11 = -1.0*dvpmf11*float(kBT/Rgyrb)
vccdr12 = hbbr12 - log(hbbr12+1) - cbbr12
dccdr12 = derivtif.derivtif(rval, vccdr12)
vccdr12 = vccdr12*kBT # energy in Kcal/mol
vpmf12 = -log(hbbr12+1)   # Potential of mean force
dvpmf12 = derivtif.derivtif(rval, vpmf12)
vpmf12 = vpmf12*kBT
dvpmf12 = -1.0*dvpmf12*float(kBT/Rgyrb)
dccdr12 = -1.0*dccdr12*float(kBT/Rgyrb) # force in Kcal/(mol*A)
vccdr22 = hbbr22 - log(hbbr22+1) - cbbr22
vpmf22 = -log(hbbr22+1)  # Potential of mean force
dccdr22 = derivtif.derivtif(rval, vccdr22)
dvpmf22 = derivtif.derivtif(rval, vpmf22)
vccdr22 = vccdr22*kBT # energy in Kcal/mol
vpmf22 = vpmf22*kBT
dccdr22 = -1.0*dccdr22*float(kBT/Rgyrb) # force in Kcal/(mol*A)
dvpmf22 = -1.0*dvpmf22*float(kBT/Rgyrb)
rval[0] = 1.0*10**(-23.0) # to avoid r=0 LAMMPS error
rvalr = rval*Rgyrb # distance in A
# Write potential to check! (Not in proper LAMMPS format yet)
dataout = column_stack((rvalr,vccdr11))
```

```
savetxt('vccr11.txt',dataout)
dataout = column_stack((rvalr,vccdr12))
savetxt('vccr12.txt',dataout)
dataout = column_stack((rvalr,vccdr22))
savetxt('vccr22.txt',dataout)
# Calculate the difference betweem pmf and hnc force
Vmfexv12 = vccdr12-vpmf12
Fmfexv12 = dccdr12-dvpmf12
Vmfbnd12 = Vmfexv12+kBT*3.0*rvalr*rvalr/(8.0)/(Rgyrb*Rgyrb)
Fmfbnd12 = Fmfexv12-2.0*kBT*3.0*rvalr/(8.0)/(Rgyrb*Rgyrb)
# write potential file in LAMMPS format
l=len(rvalr)
val=str(l)
txt=' N       ' + val
hdrtxt ='Vb11_tri\n'
hdrtxt += txt
hdrtxt += '\n'
hdrtxt += '\n'
dataout = column_stack((part,rvalr,vccdr11,dccdr11))
savetxthd(name,dataout, header=hdrtxt,
 fmt=('%12.0i %24.16e %24.16E %24.16E'))
dataout = column_stack((rvalr,dccdr11))
savetxt('dccr11.txt',dataout)
f_out = file(name,'a')
hdrtxt ='Vb12_tri\n'
hdrtxt += txt
hdrtxt += '\n'
hdrtxt += '\n'
dataout = column_stack((part,rvalr,vccdr12,dccdr12))
savetxthd(f_out,dataout, header=hdrtxt,
fmt=('%12.0i %24.16e %24.16E %24.16E'))
f_out.close()
dataout = column_stack((rvalr,dccdr12))
savetxt('dccr12.txt',dataout)
f_out = file(name,'a')
hdrtxt ='Vb22_tri\n'
hdrtxt += txt
hdrtxt += '\n'
hdrtxt += '\n'
dataout = column_stack((part,rvalr,vccdr22,dccdr22))
savetxthd(f_out,dataout, header=hdrtxt,
fmt=('%12.0i %24.16e %24.16E %24.16E'))
```

```
f_out.close()
dataout = column_stack((rvalr,dccdr22))
savetxt('dccr22.txt',dataout)
f_bond = file(nmbond,'w')
hdrtxt ='Vbond_tri\n'
hdrtxt += txt
hdrtxt += '\n'
hdrtxt += '\n'
dataout = column_stack((part,rvalr,Vmfbnd12,Fmfbnd12))
savetxthd(f_bond,dataout, header=hdrtxt,
 fmt=('%12.0i %24.16e %24.16E %24.16E'))
f_bond.close()
f_pmf = file(pmfname,'w')
hdrtxt = 'pmf\n'
hdrtxt += txt
hdrtxt += '\n'
hdrtxt += '\n'
dataout = column_stack((part,rvalr,Vmfexv12,Fmfexv12))
savetxthd(f_pmf,dataout, header=hdrtxt,
 fmt=('%12.0i %24.16e %24.16E %24.16E'))
f_pmf.close()
print 'computing angle potential between blobs'
# Here is the angle potential of mean force from Laso et al.
a=-0.25
pnts=4000  # How many discrete points
delo=pi/float(pnts)  # point spacing
smomega=arange(pnts)
smomega=smomega+1
smomega=smomega*delo
acval=arccos(-a*cos(smomega))
pn1=((1-a**2)**(3.0/2.0)*sin(smomega))
/(pi*(1-a**2*cos(smomega)*cos(smomega))**2.0)
pn2=(1+2*a*a*cos(smomega)*cos(smomega))*acval
/(sqrt(1-a*a*cos(smomega)*cos(smomega)))
pn3=3*a*cos(smomega)
pn=pn1*(pn2+pn3)/sin(smomega)
norm=pn1*(pn2+pn3)
Vang=-kBT*log(pn)
degrees=smomega*180.0/pi
degrees.sort()
Vang.sort()
degrees[0]=0.0  # Must have first angle be zero
```

```
    nang = arange(pnts)
    for i in range(0,pnts):
        nang[i]=i+1

    dang = derivtif.derivtif(degrees, Vang)
    f_ang = file(nmang,'w')
    hdrtxt = 'Vang_tri\n'
    txt=' N       ' + str(pnts)
    hdrtxt += txt
    hdrtxt += '\n'
    hdrtxt += '\n'
    dataout = column_stack((nang,degrees,Vang,dang))
    savetxthd(f_ang,dataout, header=hdrtxt,
     fmt=('%12.0i %24.16e %24.16E %24.16E'))
    dataout = column_stack((degrees,norm,pn))
    savetxthd('ang_dist.dat',dataout)
    f_ang.close()
    return (rvalr,dccdr11,dccdr12,dccdr22)
```

### A.3. Block Average Description

Here is presented a block-averaged implementation of the algorithm.

```
 # function to calculate potential
def func_potl(N,blobs,T,rhom,Rgyr,c0):
    from numpy import exp
    from scipy.fftpack import fft
    import fofrfunc
    from numpy import log
    import derivtif
    from newsavetxt import savetxthd
    from numpy import cos
    from numpy import arccos
    from numpy import sin
    from numpy import sqrt

    Navo= 6.022*10**(23.0)
    kB = 3.297627*10**(-27.0)   # in Kcal/K
    kBT = kB*T*Navo       # in Kcal/mol
    numb=N/blobs
    Rgyrb=Rgyr/sqrt(blobs)
    #
    rhoc = rhom/N    # chain number density
```

```
rhob = rhom/numb  # blob density
rhor = rhoc*Rgyrb**(3.0)  # reduce chain density
rhomr = rhom*Rgyrb**(3.0) # reduced monomer density
rhobc = rhob*Rgyrb**(3.0) # reduced blob density
#   for specific c0 value
ckk0 = c0/Rgyrb**(3.0) # in reduced units
gamma=-numb*ckk0*rhomr
print 'gamma',gamma
#   Algorithm parameters
knum = 4001 # number of k-values
klim = 40.0 # largest k-value
delk = float(klim/(knum-1)) # increment step
# initialize abscissae in k-space
kval = arange(knum-1)
kval = kval*delk
# in real space
rval = arange(4001)
rval = rval*0.01
part = arange(4001)
for i in range(0,4001):
    part[i]=i+1

Wmmdk = 2.0*(exp(-blobs*kval**(2.0))-1.0+blobs*kval**(2.0))
/(blobs**(2.0)*kval**(4.0))
Wmmdk[0]=1.0 # to avoid division by zero
dataout = column_stack((kval,Wmmdk))
savetxt('Wmmk.txt',dataout)
Wcm0 = sqrt(pi)/kval*special.erf(kval/2.0)*
exp(-kval**(2.0)/12.0)
Wcm0[0] = blobs
Wcm1=2.0*(exp(-blobs*kval**(2.0))+blobs-
1.0-blobs*exp(-kval**2.0))
*exp(-kval*kval/3.0)/(blobs*blobs*kval*kval*
(1.0-exp(-kval**2.0)))
Wcm1[0] = 0
Wbmav=Wcm0/(float(blobs))+Wcm1
dataout = column_stack((kval,Wcm0))
savetxt('Wcm0k.txt',dataout)
dataout = column_stack((kval,Wcm1))
savetxt('Wcm1k.txt',dataout)
dataout = column_stack((kval,Wbmav))
savetxt('Wbmavk.txt',dataout)
```

```
########################################
denY=Wmmdk*blobs
denZ=denY**(2.0)
nmr=(blobs*Wbmav)**2
########################################
X0=nmr/(denY)
########################################
X1=nmr/(denZ)
########################################
X2=nmr/(denY**3.0)
################################################
#hbbk=-numb*(X0-(1.0/gamma)*X1+(1.0/gamma**2.0)*X2)/(rhom)
hbbk=-numb*gamma*nmr/(1.0+blobs*gamma*Wmmdk)/rhom
################################################
# Now calculate Blob-Blob omegas
Wbbk=1.0+2.0*(exp(-blobs*kval**(2.0))+
blobs-1.0-blobs*exp(-kval**(2.0)))*

exp(-2.0*kval*kval/3.0)/(blobs*(1-exp(-kval*kval))**2.0)
Wbbk[0]=blobs
dataout = column_stack((kval,Wbbk))
savetxt('Wbbk.txt',dataout)
################################################
# Now calculated the direct correlation c(r)
D2=Wbbk*(Wbbk+rhob*hbbk)
cbbk=hbbk/(Wbbk*(Wbbk+rhob*hbbk))

########################################################
###### fix k=0 ##########################################
cbbk[0]=hbbk[0]/(1+rhoc*hbbk[0])/blobs**2
########################################################
dataout = column_stack((kval,hbbk))
savetxt('hbbk.txt',dataout)
dataout = column_stack((kval/Rgyrb,cbbk))
savetxt('cbbk.txt',dataout)
Zbbk=blobs*(Wmmdk-(Wbmav*Wbmav/(Wbbk/blobs)))
Denom=1+gamma*Zbbk
dataout = column_stack((kval,Denom))
savetxt('denom_Rgb.txt',dataout)
dataout = column_stack((kval/Rgyrb,Denom))
savetxt('denom.txt',dataout)
################################################
```

```
    # Numerical Fourier Transform
    hbbr = fofrfunc.fofrfunc(kval, hbbk, rval)
    hbbr = hbbr/(Rgyrb**3)
    dataout = column_stack((rval*Rgyrb,hbbr))
    savetxt('hbbr.txt',dataout)
    cbbr = fofrfunc.fofrfunc(kval, cbbk, rval)
    cbbr = cbbr/(Rgyrb**3)
    dataout = column_stack((rval*Rgyrb,cbbr))
    savetxt('cbbr.txt',dataout)
    # Calculate HNC potential
    vccdr = hbbr - log(hbbr+1) - cbbr
    dccdr = derivtif.derivtif(rval, vccdr)
    vpmf = -log(hbbr+1)   # Potential of mean force
    dvpmf = derivtif.derivtif(rval, vpmf)
    vccdr = vccdr*kBT # energy in Kcal/mol
    vpmf = vpmf*kBT
    dccdr = -1.0*dccdr*float(kBT/Rgyrb) # force in Kcal/(mol*A)
    dvpmf = -1.0*dvpmf*float(kBT/Rgyrb)
    rval[0] = 1.0*10**(-23.0) # to avoid r=0 LAMMPS error
    rvalr = rval*Rgyrb # distance in A
    dataout = column_stack((rvalr,vccdr))
    savetxt('vccr.txt',dataout)
    # Calculate the difference betweem pmf and hnc force
    Vmfexv = vccdr-vpmf
    Fmfexv = dccdr-dvpmf
    # Now compute the bond potential and force between blocks
    Vmfbnd = Vmfexv+kBT*3.0*rvalr*rvalr/(8.0)/(Rgyrb*Rgyrb)
    Fmfbnd = Fmfexv-2.0*kBT*3.0*rvalr/(8.0)/(Rgyrb*Rgyrb)
#    Vmfbnd = kBT*3.0*rvalr*rvalr/(8.0)/(Rgyrb*Rgyrb)
#    Fmfbnd = -2.0*kBT*3.0*rvalr/(8.0)/(Rgyrb*Rgyrb)
    # write potential file in LAMMPS format
    l=len(rvalr)
    val=str(l)
    txt=' N       ' + val
    hdrtxt ='Vbave\n'
    hdrtxt += txt
    hdrtxt += '\n'
    hdrtxt += '\n'
    dataout = column_stack((part,rvalr,vccdr,dccdr))
    savetxthd(name,dataout, header=hdrtxt,
     fmt=('%12.0i %24.16e %24.16E %24.16E'))
    dataout = column_stack((rvalr,dccdr))
```

```
savetxt('dccr.txt',dataout)
f_bond = file(nmbond,'w')
hdrtxt ='Vbond\n'
hdrtxt += txt
hdrtxt += '\n'
hdrtxt += '\n'
dataout = column_stack((part,rvalr,Vmfbnd,Fmfbnd))
savetxthd(f_bond,dataout, header=hdrtxt,
 fmt=('%12.0i %24.16e %24.16E %24.16E'))
f_bond.close()
f_pmf = file(pmfname,'w')
hdrtxt = 'pmf\n'
hdrtxt += txt
hdrtxt += '\n'
hdrtxt += '\n'
dataout = column_stack((part,rvalr,Vmfexv,Fmfexv))
savetxthd(f_pmf,dataout, header=hdrtxt,
fmt=('%12.0i %24.16e %24.16E %24.16E'))
f_pmf.close()
print 'computing angle potential between blobs'
# Here is the angle potential of mean force from Laso et al.
# This should reproduce the correct angular distributions
a=-0.25
pnts=4000  # How many discrete points
delo=pi/float(pnts)  # point spacing
smomega=arange(pnts)
smomega=smomega+1
smomega=smomega*delo
acval=arccos(-a*cos(smomega))
pn1=((1-a**2)**(3.0/2.0)*sin(smomega))
/(pi*(1-a**2*cos(smomega)*cos(smomega))**2.0)
pn2=(1+2*a*a*cos(smomega)*cos(smomega))*acval
/(sqrt(1-a*a*cos(smomega)*cos(smomega)))
pn3=3*a*cos(smomega)
pn=pn1*(pn2+pn3)/sin(smomega)
norm=pn1*(pn2+pn3)
Vang=-kBT*log(pn)
degrees=smomega*180.0/pi
degrees.sort()
Vang.sort()
degrees[0]=0.0  # Must have first angle be zero
nang = arange(pnts)
```

```
for i in range(0,pnts):
    nang[i]=i+1

dang = derivtif.derivtif(degrees, Vang)
f_ang = file(nmang,'w')
hdrtxt = 'Vang_tri\n'
txt=' N       ' + str(pnts)
hdrtxt += txt
hdrtxt += '\n'
hdrtxt += '\n'
dataout = column_stack((nang,degrees,Vang,dang))
savetxthd(f_ang,dataout, header=hdrtxt,
 fmt=('%12.0i %24.16e %24.16E %24.16E'))
dataout = column_stack((degrees,norm,pn))
savetxthd('ang_dist.dat',dataout)
f_ang.close()
return (rvalr,dccdr)
```

REFERENCES CITED


[1] E. A. Campo, *Industrial Polymers* Hanser Gardner Publications, Cincinnati, O.H., 2007.

[2] T. P. Lodge and M. Muthukumar, J. Phys. Chem. **100**, 13275 (1996).

[3] P.-G. de Gennes, *Scaling Concepts in Polymer Physics* Cornell University Press, Ithaca, NY, 1979.

[4] M. Rubinstein and R. H. Colby, *Polymer Physics*, Oxford University Press Inc., New York, N.Y., 2003.

[5] G. Strobl, *The Physics of Polymers*, Springer, Heidelberg, 1996.

[6] M. D. Gehlsen, J. H. Rosedale, F. S. Bates, G. D. Wignall, L. Hansen, and K. Almdal, Phys. Rev. Lett. **68** 2452 (1992).

[7] K. Binder, Ed *Monte Carlo and Molecular Dynamics Simulations in Polymer Science*, Oxford University Press: New York, 1995.

[8] J. -P. Hansen and I. R. McDonald,*Theory of Simple Liquids*, Academic Press, New York, N.Y. 2nd Ed., 1990.

[9] D. A. McQuarrie *Statistical Mechanics*, University Science Books, Sausalito, C.A. 2000.

[10] D. Chandler and H.C. Anderson, J. Chem. Phys. **57**, 1930 (1972).

[11] B. M. Ladanyi and D. Chandler, J. Chem. Phys. **62**, 4308 (1975).

[12] D. Chandler and L. R. Pratt, J. Chem. Phys. **65**, 2925 (1976).

[13] L. R. Pratt and D. Chandler, J. Chem. Phys. **66**, 147 (1977).

[14] K. S. Schweizer and J. G. Curro, Chemical Physics **149**, 105 (1990).

[15] K. S. Schweizer and J. G. Curro, Adv. Chem. Phys., **98**, 1 (1997).

[16] M. Doi and S. F. Edwards, *The Theory of Polymer Dynamics*, Oxford University Press, Oxford, 1986.

[17] K. S. Schweizer and J. G. Curro, J. Chem. Phys., **89** 5059 (1989).

[18] K. S. Schweizer and A. Yethiraj J. Chem. Phys., **98** 9053 (1993).

[19] A. Yethiraj and K. S. Schweizer, J. Chem. Phys. **98**, 9080 (1993).

[20] B. J. Reynwar, G. Illya, V. A. Harmandaris, M. M. Muller, K. Kremer and M. Deserno, Nature **447** 461 (2007).

[21] G. Srinivas, D. E. Discher and M. L. Klein, Nat. Mater, **3** 638 (2004).

[22] R. Everaers, S. K. Sukumaran, G. S. Grest, C. Svaneborg, A. Sivasubramanian, and K. Kremer, Science, **303** 823 (2004).

[23] W. G. Noid, J. Chem. Phys, **139**, 090901 (2013).

[24] Y. Li, B. C. Abberton, M. Kroger, and W. K. Liu, Polymers, **5**, 751 (2013).

[25] M. Putz, J. G. Curro, and G. S. Grest, J. Chem. Phys. **114** 2847 (2001).

[26] M. G. Martin and J. I. Siepmann, J. Phys. Chem. B **102** 2569 (1998).

[27] D. Heine, D. T. Wu, J. G. Curro, and G. S. Grest, J. Chem. Phys **118** 914 (2003).

[28] E. Jaramillo, D. T. Wu, G. S. Grest, and J. G. Curro, J. Chem. Phys **120** 8883 (2004).

[29] K. Kremer and G. S. Grest, J. Chem. Phys. **92**, 5057 (1990).

[30] Ji-Xuan Hou1, Carsten Svaneborg, Ralf Everaers, and Gary S. Grest, Phys. Rev. Lett. **105** 068301 (2010)

[31] D. Reith, M. Putz, F. Muller-Plathe, J. Comput. Chem. **24** 1624 (2003).

[32] P. Carbone, H. A. Karimi Varzaneh, X.Y. Chen and F. Müller-Plathe, J. Chem. Phys. **128**, 0649041 (2008).

[33] R. L. Henderson, Phys. Lett. **49A**, 197 (1974).

[34] S. Izvekov, M. Parrinello, C. J. Burnham, and G. A. Voth, J. Chem. Phys. **120**, 10896 (2004)

[35] S. Izvekov and G. A. Voth J. Phys. Chem. B, **109**, 2469 (2005).

[36] T. D. Hone, S. Izvekov, and G. A. Voth, J. Chem. Phys. **122**, 054105 (2005).

[37] V. Krakoviack, J. -P. Hansen and A. A. Louis, Europhys. Lett. **58(1)** 53 (2002).

[38] G. Yatsenko, E. J. Sambriski, M. A. Nemirovskaya, and M. Guenza, Phys. Rev. Lett **93** 257803 (2004).

[39] G. Yatsenko, E. J. Sambriski, and M. G. Guenza, J. Chem. Phys. **122** 054907 (2005).

[40] E. J. Sambriski and M. G. Guenza, Phys. Rev. E **76** 051801 (2007).

[41] A. J. Clark, J. McCarty,, and M. G. Guenza, J. Chem. Phys. **139** 124906 (2013).

[42] A. J. Clark, and M. G. Guenza J. Chem. Phys. **132**, 044902 (2010).

[43] H. Yamakawa, *Modern Theory of Polymer Solutions*, Harper and Row, New York, N. Y., 1971.

[44] Y. Rosenfeld, N. W. Ashcrof, Physical Review A, **20**, 2162 (1979).

[45] J. McCarty, A. J. Clark, I. Y. Lyubimov, and M.G. Guenza, Macromol. **45** 8482 (2012).

[46] M. Neri, C. Anselmi, M. Cascella, A. Maritan, P. Carloni, Phys. Rev. Lett., **95**, 218102 (2005).

[47] M. G. Guenza, J. Phys.: Condens. Matter, **20** 033101 (2008).

[48] I.-j. Chen, H.-J. Quian, Z.-Y. Lu; Z.-S. Li, C. C. Sun, J. Phys. Chem. B, **110**, 24093 (2006).

[49] V. A. Harmandaris, D. Reith, N. F. A. van der Vegt, K. Kremer, Macromol. Chem. Phys. **208**, 2109 (2007).

[50] M. Praprotnik, L. D. Site, K. Kremer, Annu. Rev. Phys. Chem, **59** 545 (2008).

[51] Q. Sun, J. Ghosh, R. Faller, *State point dependence and transferability of potentials in systematic structural coarse graining.* In: G. Voth, Ed.; *Coarse-Graining of Condensed Phase and Biomolecular Systems*. CRC Press. 2008.

[52] A. P. Lyubartsev, A. Laaksonen, Phys Rev. E., **52**, 3730 (1995).

[53] M. Praprotnik, C. Junghans, L. D. Site, K. Kremer, Comput. Phys. Commun., **179**, 51 (2008).

[54] S. O. Nielsen, C. F. Lopez, G. Srinivas, M. L. Klein, J. Chem. Phys., **119**, 7043 (2003).

[55] T. A. Knotts IV, N. Rathore, D. C. Schwartz, J. J. de Pablo, J. Chem. Phys., **126**, 084901(2007).

[56] J. J. de Pablo, Annu. Rev. Phys. Chem., **62**, 555 (2011).

[57] A. A. Louis J. Phys.: Condens. Matter **14**, 9187 (2002)

[58] Fukunaga, H.; Takimoto, J.; Doi, M. *J. Chem. Phys.* **2002**, 116, 8183.

[59] Carbone, P.; Varzaneh, H. A. K.; Chen, X.; Müller-Plathe, F. *J. Chem. Phys.* **2008**, 128, 064904.

[60] M. E. Johnson, T. Head-Gordon, A. A. Louis, J. Chem. Phys., **126**, 144509 (2007).

[61] F. Müller-Plathe, Chem. Phys. Chem., **3**, 754 (2002).

[62] A. J. Clark, J. McCarty, I. Y. Lyubimov, and M. G. Guenza, Phys. Rev. Lett. **109**, 168301 (2012).

[63] H. S. Ashbaugh, H. A. Patel, S. K. Kumar, S. Garde, J. Chem. Phys., **122**, 104908 (2005).

[64] I. Y. Lyubimov, J. McCarthy, A. Clark, and M. G. Guenza, J. Chem. Phys. **132**, 2249031 (2010).

[65] K. S. Schweizer, J. G. Curro, Macromol., **1998**, **21**, 3070, 3082 (1998).; J. Chem. Phys., **149**, 105 (1990).

[66] E. J. Sambriski, G. Yatsenko, M. A. Nemirovskaya, M. G. Guenza, J. Chem. Phys., **125**, 234902 (2006).

[67] P. Ascarelli, R. J. Harrison, Phys. Rev. Lett., **22**, 385 (1969)..

[68] F. H. Stillinger, H. Sakai, S. Torquato, J. Chem. Phys., **117**, 288 (2002).

[69] A.A. Louis, P. G. Bolhuis, J. P. Hansen, and E. J. Meijer, Phys. Rev. Lett. **85**, 2522 (2000)

[70] K. G. Honnell, C. K. Hall, and R. Dickman, J. Chem. Phys. 87, 664 (1987)

[71] K. S. Schweizer, J. G. Curro, J. Chem. Phys., **89**, 3342 (1988).; K. S. Schweizer, J. G. Curro, *ibid*, **89**, 3350 (1988).

[72] F. T. Oyerokun, K. S. Schweizer, J. Phys. Chem. B, **109**, 6595 (2004).

[73] A. P. Chatterjee, K. S. Schweizer, J. Chem. Phys., **108**, 3813 (1998).

[74] J. McCarty, I. Y. Lyubimov, and M. G. Guenza, J. Phys. Chem. B **113** 11876 (2009).

[75] S. Plimpton J. Comput. Phys. **117**, 1 (1995).

[76] E. K. Watkins and W. L. Jorgensen, J. Phys. Chem. A **105** 4118 (2001).

[77] A. Uhlerr, M. Doxastakis, V.G. Mavrantzas, D. N. Theodorou, S. J. Leak, N. E Adam, and P. E. Nyberg *Europhys. Lett.* **57**, 506 (2002).

[78] N. Ch. Karayiannis, V. G. Mavrantzas, and D. N. Theodorou, Phys. Rev. Lett. **88**, 1055031 (2002).

[79] C. N. Likos, A. Lang, M. Watzlawek and H. Lowen, Phys Rev. E **63**, 031206 (2001).

[80] R. Evans, Adv. Phys. **24**, 143, (1979).

[81] M. S. Shell, J. Chem. Phys. **129**, 144108 (2008).

[82] J. F. Rudzinski and W. G. Noid, J. Chem. Phys. 135 214101 (2011).

[83] Honnell, K. G.; Curro, J. G.; Schweizer, K. S. *Macromol.* **23**, 3496.

[84] A. C. Hindmarsh, P. N. Brown, K. E. Grant, S. L. Lee, R. Serban, D. E. Shumaker, and C. S. Woodward, ACM Trans. Math. Softw. **31**, 363 (2005)

[85] M. Laso, H. C. Ottinger and U. W. Suter J. Chem. Phys. **95** 2178 (1991).

[86] J. McCarty and M. G. Guenza, J. Chem. Phys. **133**, 094904 (2010).

[87] J. McCarty, I. Y. Lyubimov, and M. G. Guenza, Macromol. **43**, 3964 (2010).

[88] N. Balsara in *Physical Properties of Polymers Handbook*, Ed. James E. Mark, Woodbury, N.Y. AIP Press (1996).

[89] O. Olabisi, L. M. Robeson, and M. T. Shaw, *Polymer-Polymer Miscibility* (Academic Press, New York, 1979).

[90] S. A. Baeurle and J. Kroener, J. Math. Chem. **36**, 409 (2004).

[91] R. D. Groot, Lect. Notes Phys. **640**, 5 (2004).

[92] H. Tang and K. S. Schweizer, J. Chem. Phys. **105**, 779 (1996).

[93] H. S. Jeon, J. H. Lee, and N. P. Balsara, Macromol. **31**, 3328 (1998).

[94] J. H. Lee, N. P. Balsa, A. K. Chakraborty, R. Krishnamoorti, and B. Hammouda, Macromol. **35**, 7748 (2002).

[95] R. Krishnamoorti, W. W. Graessley, L. J. Fetters, R. T. Garner, and D. J. Lohse, Macromol. **28**, 1252 (1995).

[96] M. Murat and K. Kremer, J. Chem. Phys. **108**, 4340 (1998).

[97] A. Sariban and K. Binder, J. Chem. Phys. **86**, 5859 (1987); A. Sariban and K. Binder, Macromolecules **21**, 711 (1988); A. Sariban and K. Binder, Colloid Polym. Sci. **267**, 469 (1989).

[98] A. B. Bhatia, and D. E. Thornton, Phys. Rev. B **2**, 3004 (1970).

[99] K. Binder, Computer Physics Communications **147**, 22 (2002).

[100] J.P. Wittmer, P. Beckrich, J. Johner, A.N. Semenov, S.P. Obukhov, H. Meyer, and J. Baschnagel, Europhys. Lett. **77** 56003 (2007).

[101] J. P. Wittmer, P. Beckrich, H. Meyer, A. Cavallo, A. Johner, J. Baschnagel, Phys. Rev. E **76** 011803 (2007)

[102] P. Beckrich, A. Johner, A.N. Semenov, S.P. Obukhov, H. Benot, and J.P. Wittmer, Macromol. **40** 3805-3814 (2007).

[103] V. G. Mavrantzas, T. D. Boone, E, Zevropoulou, and D. N. Theodorou, Macromol. **32**, 5072 (1999).

[104] L. Zhao, Y. G. Li, J. Mi, and C. Zhong, J. Chem. Phys., **123**, 124905 (2005).

[105] C.-Y. Shew and A. Yethiraj, J. Chem. Phys., **106**, 5706 (1997).

[106] D. Laria, D. Wu, and D. Chandler, J. Chem. Phys., **95**, 4444 (1991).